論文 / 著書情報
Article / Book Information

題目(和文)	原始惑星系円盤から太陽系への化学進化
Title(English)	Chemistry from Protoplanetary Disks to the Solar System
著者(和文)	WEI CHEN-EN
Author(English)	WEI CHEN-EN
出典(和文)	学位:博士(理学), 学位授与機関:東京工業大学, 報告番号:甲第11385号, 授与年月日:2020年3月26日, 学位の種別:課程博士, 審査員:奥住 聡,野村 英子,井田 茂,中本 泰史,佐藤 文衛,玄田 英典
Citation(English)	Degree:Doctor (Science), Conferring organization: Tokyo Institute of Technology, Report number:甲第11385号, Conferred date:2020/3/26, Degree Type:Course doctor, Examiner:,,,,,
学位種別(和文)	博士論文
Type(English)	Doctoral Thesis

Chemistry from Protoplanetary Disks to the Solar System

Wei, Chen-En

Department of Earth and Planetary Sciences

Tokyo Institute of Technology

A thesis submitted for the degree of

Doctor of Science

January 31, 2020

Abstract

Currently, there is no astrochemical model can follow the chemistry fully during the whole evolution from molecular clouds to protoplanetary disks (PPDs) and further to planets and small bodies, thus we usually collect the clues within stages to stages and compare the present observations with models trying to put the pieces together to understand the whole picture of chemical evolution. In this thesis, we focus on the stage of PPDs, where are the reservoirs of gas, dust, and ice which are required to be the building blocks of planets and small bodies. The components in the disk midplane are regarded as the initial composition of the planets and small bodies. Therefore, we focus on the stage of PPDs and aim to understand the following two topics (1) The carbon depletion problem in the inner solar system and (2) The effect of mantle reactions on the formation of complex organic molecules (COMs) by comparing with Comet 67P/Churyumov-Gerasimenko (Comet 67P/C-G).

In the first topic, we investigated the carbon depletion problem in the inner Solar system by examining the effect of carbon grain destruction. First of all, we constructed a 2-phase chemical model considering gas-phase reaction and gas-grain interaction under the physical conditions of typical PPDs. With the physical model coupling with the chemical network, we presented the 2-dimensional molecular distribution and further used it to calculate the midplane solid carbon to silicon ratio along the disk radii. The results with carbon grain destruction did reproduce the carbon depletion gradient in the inner region of the disk but with some quantitative discrepancy. On the other hand, if there were no carbon grain destruction, most of the carbon remained in the refectory and thus carbon to silicon ratio almost keeps constant between different radii. Besides, in the carbon-rich case, the abundance of carbon-bearing species, such as HCN and carbon-chain molecules increased significantly near the midplane, while oxygen-bearing species are depleted. Among all

species, we suggested HCN might be one of the good tracers to probe the effect of carbon grain destruction since it showed about 8 orders of magnitude differences between the two cases. Following this indication, we used the obtained molecular abundance distributions, coupled with line radiative transfer calculations to search the potential tracers to examine carbon grain destruction in nearby PPDs. Our results show that line emission from T Tauri disks is too weak to probe carbon grain destruction but this effect can be probed through the line ratio of HCN/$H^{13}CN$ and c-C_3H_2 in Herbig Ae disks due to the higher luminosity and larger hot region. The $H^{13}CN$ emission traces a relatively deeper layer compared to the HCN line and their ratio shows that differences due to carbon grain destruction may be detectable with ALMA.

Though we produced the gradient of carbon depletion in the Solar system in the first part of the thesis, the quantitative discrepancy might be due to the lack of grain-surface reactions which play an important role to produce COMs and possibly stores the carbon in the icy form making influences on the solid carbon to silicon ratios. Therefore, in our second topic, we improved our chemical model by applying a 3-phase model, considering not only gas-phase reaction and gas-grain interaction but also grain-surface reaction and mantle reactions into our network. The reaction rates caused by the swapping inside the mantle are often set as the same as those of the surface reactions. In this thesis, we constructed a formula of mantle reaction rate based on the recent experiments which show ice chemistry proceeding through the thermal process inside the ice bulk. Moreover, experiments suggested that mantle reaction can enhance the molecular complexity and be the possible pathway to produce the candidate compounds, Ammonium carbamate, accounting for the broad absorption features in the reflected spectra of comet 67P/C-G. With this improved reaction network, we examined the effect of mantle reactions on the formation of COMs especially focusing on reproducing the materials detected on comet 67P/C-G. Our results showed that these mantle reactions can occur efficiently when temperature $\geq$ 120K. Now, the FU Ori objects can raise the temperature of the disks and affect the chemical reactions. We found that if the Solar system had experienced the outburst in the early stage of the evolution, once the mass accretion rate exceeds 10^{-5} $M_\odot yr^{-1}$, the abundance of Ammonium carbamate can reach 10^{-6}

relative to total hydrogen nuclei under some assumptions with efficient mantle reactions. The effect of mantle reactions depends on the structure of ices, namely the thermal history of small bodies and has room for further improvement in future work.

Acknowledgements

I would like to express my deep appreciation to my advisor, Professor Hideko Nomura, who guides me not only during my Ph.D. She was my advisor during my stay at Tokyo Tech. as an exchanged student. She led me to this research field and broaden my knowledge about planetary science, giving me lots of chances to discuss with researchers all over the world. She is always kind and penitent to provide me many suggestions and help me solve the problems either they are related to research or not. I could not accomplish my research and live in Japan without worries without her support. Also, I gratefully thank to all the referees. All the comments and suggestions make the thesis more completed.

Furthermore, I would like to extend my appreciation to my other collaborators for assisting my researches. Prof. Tom Millar and Prof. Catherine Walsh, who kindly give me lots of advice, helping me improve the research. I sincerely thank Prof. Patrice Theulé, who is my host during my short-term stay at Aix-Marseille University. He helps me to make up the knowledge relating to the chemical experiments and encourages me to ask more questions. He showed me around France and introduced me to other researchers, making my life there more fulfilled. Moreover, I appreciate Prof. Wing-Huen Ip, Prof. Jeong-Eun Lee, Prof. Ted Bergin, Prof. Yuri Aikawa, Dr. Kenji Furuya, Dr. Taiki Suzuki and Dr. Yu Komatsu for all the discussions helping me achieve better research.

I am grateful for everyone I met during the doctoral program and all my friends. Through my ups and downs, they are always there and make my every day enjoyable. Last but not least, I gratefully thank my family. With their unconditional support and love, I could realize my goals without any worries.

Contents

Chapter 1

General Introduction

1.1 The Evolution of Young Stellar Objects

1.1.1 Formation of Low-Mass Stars

Stars are thought to be formed inside a dense molecular clouds with density $\sim 10^4$ - 10^5 cm^{-3}. Since clouds are opaque, the interior temperature is around 10-20K. Once the prestellar core formed, the evolution stage of low mass stars (M$\leq$ 2 $M_\odot$) can be classified into 4 classes (Figure 1.1; Lada 1987; Andre et al. 1993; Andre & Montmerle 1994) based on the characteristics of their spectral energy distribution (SED).

Due to the gravitational collapse, the surrounding materials fall into the prestellar core resulting a protostar surrounding by a infalling envelope. At the initial stage of star formation (Class 0), the mass of the surrounding envelope is larger than the central protostellar mass. The SED peaks in the far-IR or mm wavelength with no flux detected in the near-IR. As materials keep falling into the central protostar, the mass of the protostar exceeds the surrounding envelope and move on to the first stage (Class I). The timescale is about 10^5 years. The SED is composed of near-IR and mid-IR wavelength and it is approximately flat. At the same time, during class 0 and I there are disks surrounding the protostars which make the conservation of the angular momentum and this two stages are referred as embedded stage.

After 10^{5-6} years, due to the continuous accretion of the surrounding envelope and the outflow from the protostars, the envelope dissipate. The disk is visible in the optical band and move on to the second stage, The Class II object also called as classical T-Tauri stars and the disk encircling it is protoplanetary disk. Comparing to Class I object, the SED of Class II object falls between near-IR and mid-IR wavelength, composed of the blackbody radiation from the protostars and the near-IR from the protoplanetary disk. The planetary system are thought to be formed during this stage. Dusts collide with each others, grow and settle to the disk midplane, becoming the building blocks of the planets and the small bodies (e.g., asteroids and comets) in the system. The detail of the protoplanetary disks will be introduced in the next section.

After that (around 10^{6-7} years), the accretion settle down. In the third stage, the pre-main sequence stars is orbiting by a gas-poor disk consisting the product of dust collision. The SED of Class III object is mainly the stellar blackbody radiation. Finally, the stars reach the main-sequence, the remnant disk are blew away by the stellar winds and the planetary system is born.

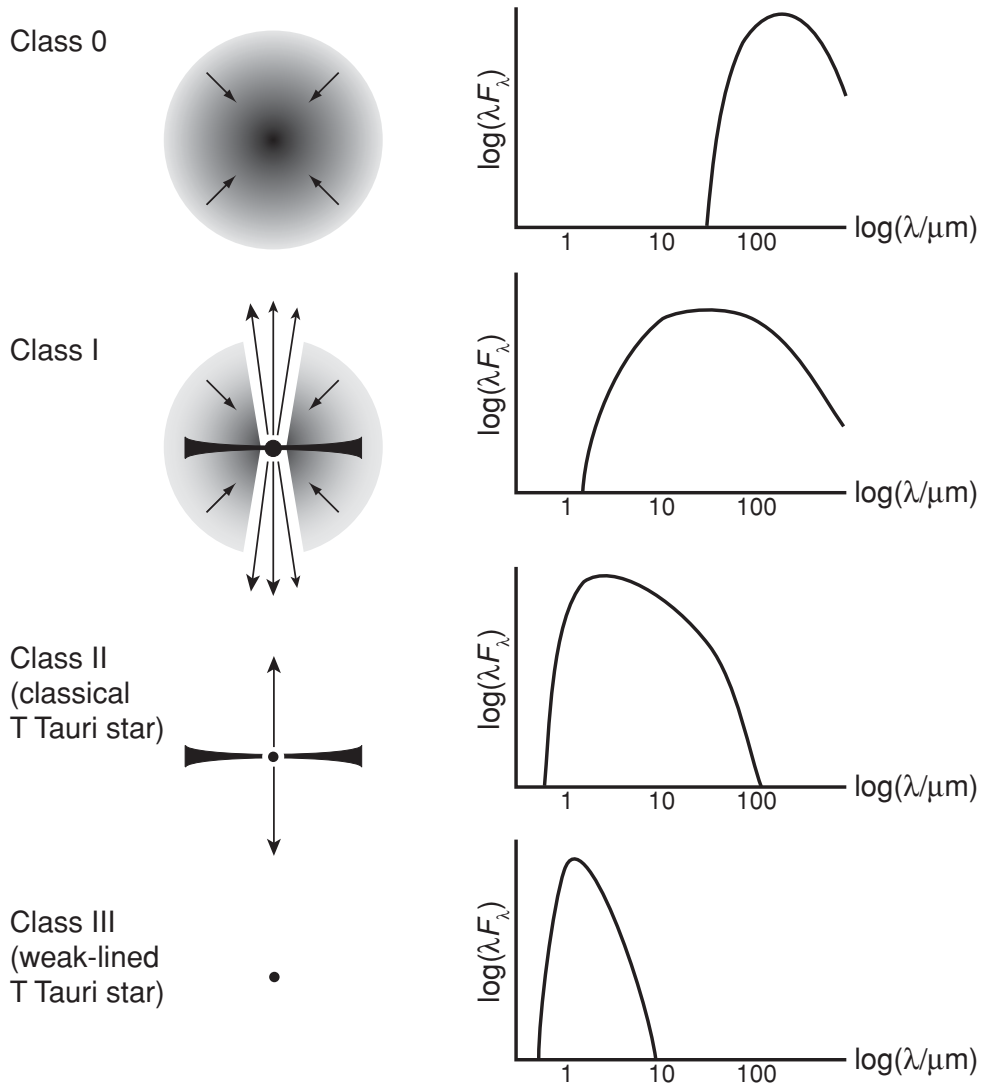

Figure 1.1: The schematic overview of different stages in the left panel with the observational classification of low-mass star formation in the right panel (Armitage 2010)

1.1.2 FU Orionis Phenomenon

FU Orionis (FU Ori) phenomenon demonstrate that accretion disks is highly episodic during early stellar evolution. The mass accretion rate varies from 10^{-7} to a few 10^{-4} $M_{\odot}yr^{-1}$, in the quiescent state and outburst state, respectively (Hartmann & Kenyon 1996; Audard et al. 2014). Figure 1.2 shows the estimated mass accretion verses time evolution of low-mass stars. It is thought FU Ori outbursts span from Class I objects with embedding envelopes to ones with tenuous envelope close to Class II stage (Quanz et al. 2007).

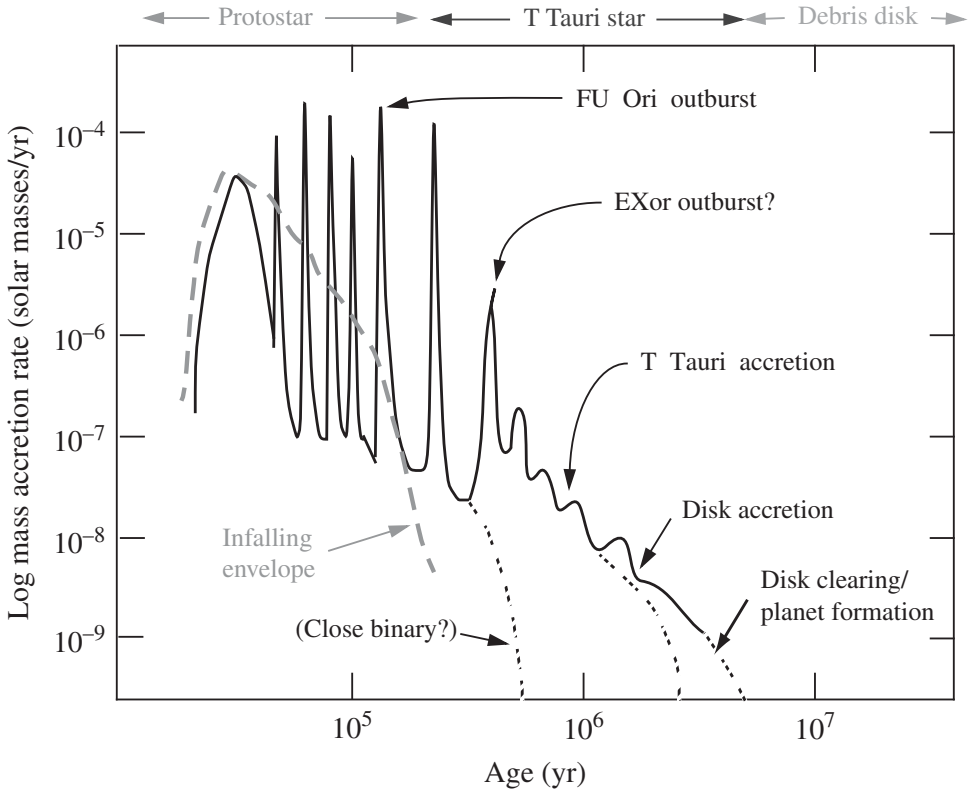

Figure 1.2: The estimated mass accretion rates during the formation of a solar-type (low-mass) star (Hartmann 2008).

FU Ori Phenomenon are originally identified by three long-studeid objects, FU Ori, V1057 Cyg and V1514 Cyg as a class with strong outburst in optical light (Herbig 1966; Herbig 1977). They exhibit large increase of brightness $\sim$ 4 orders of magnitude or higher with timescale 50-100 years (Hartmann & Kenyon 1996). Though the outburst timescale is relatively short, by comparing the the number of observed FU ori objects and the star formation rate in the solar neighborhood, it is estimated that the each young star will undergo $\sim$ 10 outburst over its lifetime (Hartmann &

Kenyon 1985) with quiescent duration from $\sim 10^3$ - 10^4 years (Scholz et al. 2013). Figure 1.3 is the schematic view of FU Ori phenomenon. A central protostars surrounded by a infalling envelope and accretion disk. The mass accretion rate of disk is 10^{-7} $M_\odot yr^{-1}$ in the quiescent state and reaches 10^{-4} $M_\odot yr^{-1}$ when outburst occurs. During the century-long outburst, $\sim 10^{-2}$ $M_\odot$ is added to the central protostar. Meanwhile, high velocity wind are generated with mass loss rate $\sim 10^{-1}$ of the disk accretion rate and the infalling envelope keeps feeding the disk between repetitive outburst events.

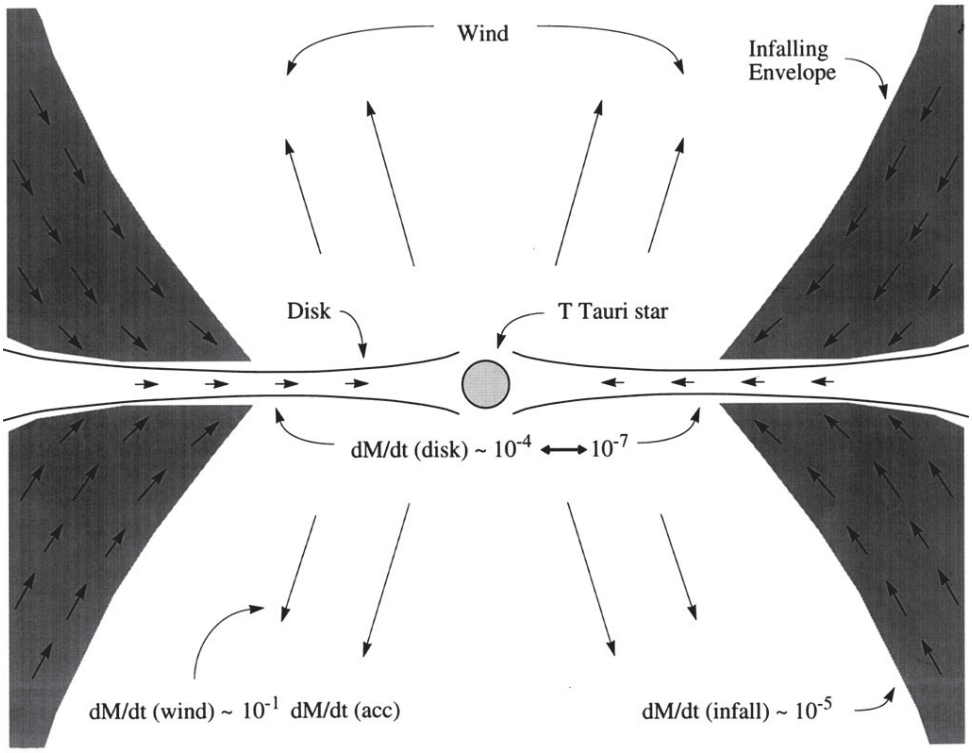

Figure 1.3: The schematic overview of FU Ori objects (Hartmann & Kenyon 1996).

Additionally, the so-called luminosity problem indicating the inconsistency between the observed luminosity of young stellar objects and the theoretical predicted luminosity. The observed luminosity is about an order of magnitude less then the expected value. The episodic accretion which might be associated with FU Ori outburst is the most common explanation for this problem that protostars accrete most of their mass during during short outbursts and spend most of time during the low-luminosity quiescent state (Kenyon et al. 1990).

From the other aspect, the sudden increment of mass accretion rate increase the temperature of the disks and further alter the chemical composition in the disks. Several chemical tracers towards FU Ori outburst have been proposed, such as HCO^+, N_2H^+ and H_2CO (Visser & Bergin 2012; Visser et al. 2015; Molyarova et al. 2018). Moreover, some complex organic molecules (COMs; molecules containing six or more atoms; Herbst & van Dishoeck 2009) formed in the ice mantles become possible to be observed when outburst occurs (Molyarova et al. 2018). Usually around the solar-type stars, the snowlines of COMs and also water are in the inner few au of the disks, making it difficult to be observed. However, when outburst happened, the rapid increment of accretion rate can push the snowline outwards and give us a chance to probe a fresh sublimation of COMs, e.g., the recent the observation towards V883 ori (Cieza et al. 2016; Lee et al. 2019).

1.2 The Chemistry of Disks and the Solar System Objects

1.2.1 The Chemistry in Protoplanetary Disks

The protoplanetary disk is the disk surrounding the Class II protostars, composing of gas and dust with mass ratio equals to 100. The environment of the protoplanetary disk is diverse. The density varies by about 10 orders of magnitude and the temperature ranges from a few K to thousands of K. From the surface to the midplane, the main structure can be classified into three layers (Figure 1.4); a surface PDR (Photon Dominated Region)-like layer, a warm molecular layer and a cold midplane. The PDR-like layer mainly consists of atoms and ions due to the severe stellar UV radiation and interstellar radiation field the latter of which can influence the disk structure at larger radial distances from the star. In this layer, chemistry induced by photodissociation and photoionization dominates. Moving downward to the warm molecular layer, molecules here can survive due to partial shielding from the radiation field. In this layer, gas phase two-body reactions (neutral-neutral reactions and ion-neutral reactions) are active and set the molecular composition. Towards the midplane, excepting the very inner part, the temperature decreases due to the efficient shielding of radiation. Therefore, in the midplane, molecules can freeze on the surfaces of dust grains. Chemical modeling of PPDs has been widely described in, for example, Bergin et al. (2007), Henning & Semenov (2013) and Dutrey et al. (2014).

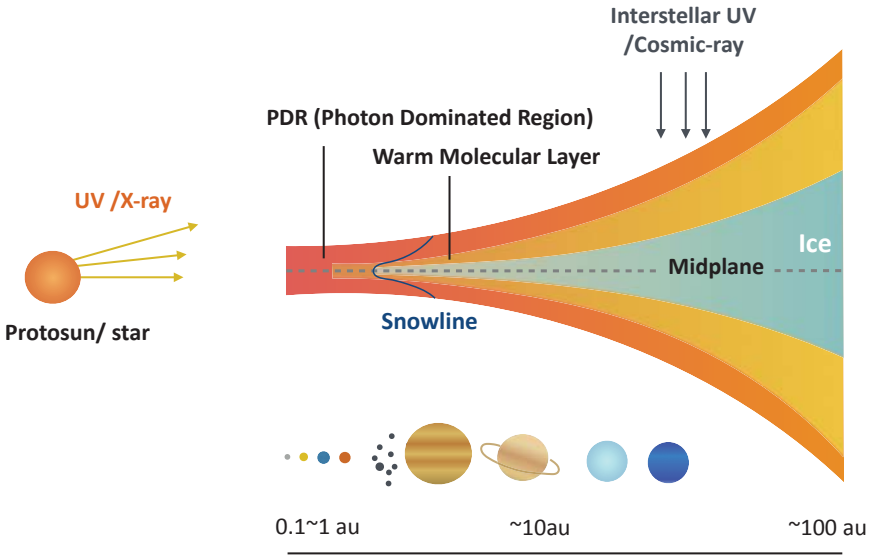

Figure 1.4: A schematic picture of protoplanetary structure.

The distribution of molecules is important for planetary formation, especially near the midplane. The final composition of planets is related to the location of snowlines in comparison with the planet's formation location. The balance between desorption and adsorption of gas-phase species onto grains determines the composition of the materials forming planetesimals and planets. From the observational point of view, several molecules, such as CO, CO_2, CN, HCN, H_2CO, C_2H_2, OH (e.g., Dutrey et al. 1997; Thi et al. 2004; Pontoppidan et al. 2010) and some deuterated molecules, DCO^+, and DCN (e.g., van Dishoeck et al. 2003; Qi et al. 2008) have been detected in the disks so far. Recently, some relatively complex molecules in PPDs have been detected, such as CH_3CN, CH_3OH and HCOOH (Öberg et al. 2015; Walsh et al. 2016; Favre et al. 2018; Loomis et al. 2018; Bergner et al. 2018). So far, the total molecular inventory in PPDs is > 20. Thanks to the high spatial resolution and sensitivity of ALMA, we have opportunities to reveal further detail, even in the inner region of disks (< 10's of au).

1.2.2 The Bulk Abundances of Common Elements in the Solar System

Forming from the protoplanetary disks, the chemical compositions in the solar system are regulated by the previous stage. Here we focus on the common elements showing in the Earth, e.g., carbon, oxygen and nitrogen. Figure 1.5 shows the relative abundance ratio of C,N,O to silicon of sun, ISM and solar system objects including

Earth, meteorites and comets as a function of abundance ratio of hydrogen to silicon (Jura 2006; Pontoppidan et al. 2014). Though it could not tell us which chemical compositions are the main carriers of the elements, it indicates the volatility of the chemical compounds with the elements. For instance, the ISM and sun represents the totally amount of elements which were available during the formation stage. Beyond the Sun, most of the solar system objects are hydrogen-poor. This implies hydrogen is too volatile to be incorporated into the solid-form chemical compounds, and thus most of them are depleted in hydrogen. In the case of comets, which carries largest amount of hydrogen, is because comets are thought to be form in the outer region of the disks and most of the hydrogen can be stored in the water ice form. On the other hand, when it is inside the water snowline, rocky planetesimals are lack of hydrogen.

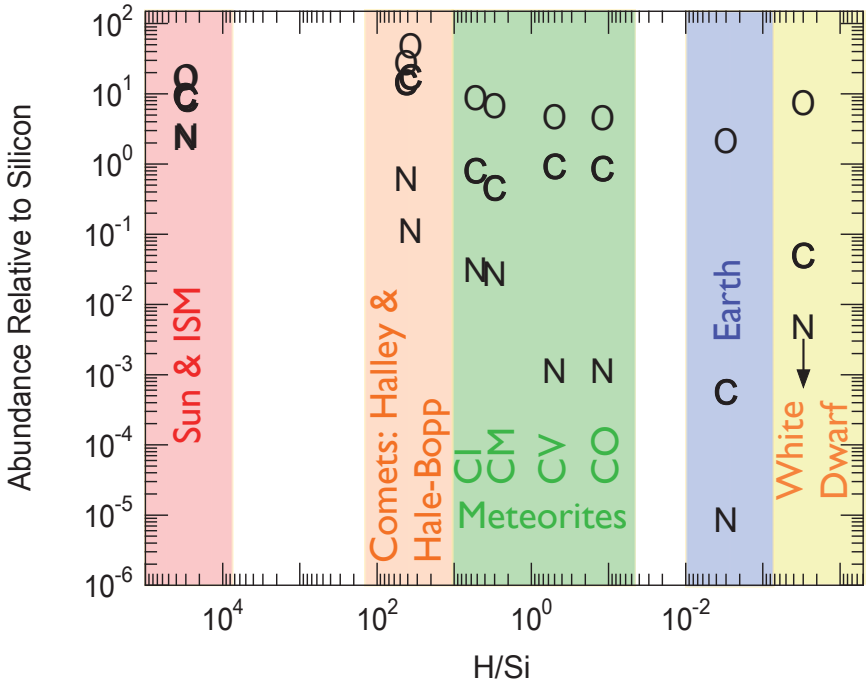

Figure 1.5: The relative elemental abundance in the solar system. CNO relative to silicon abundance ratio in the vertical axis and H relative to silicon in the horizontal axis. The figure is taken from Pontoppidan et al. (2014) and noted here the white dwarf value are from GD 40 (Jura et al. 2012 with arbitrary H/si ratio in the horizontal axis.

Moving to the case of oxygen, the least depleted element within CNO, comparing to the sun and ISM, indicates the carriers of most of the oxygen is relatively less volatile, namely, relatively refractory. The possible carrier is silicate, mostly $SiO_4{}^{4-}$ or $SiO_3{}^{2-}$ (Pontoppidan et al. 2014). The measurements of comets show comparable or even larger ratios comparing to the solar value and the recent measurement towards

comet 67P/C-G shows the O/Si value around 9-16 with uncertainty +9 and -4 (Rubin et al. 2019). All comets show consistent value and support the possible carrier, silicate, which have larger O/Si within the refractory compounds. On the other hand, rocky planetesimals shows about an order of magnitude depleted of oxygen, indicating the possible carriers of it should be the chemical compound with less fraction of oxygen in the composition and should be the compounds freeze in the outer region but present in the gaseous form in the inner disk. Therefore, the likely candidates are H_2O, CO_2 and CO.

In the case of carbon, it displays clearly gradient along the heliocentric distance. In the outer region, comets show the comparable carbon to silicon abundance ratio. Moving inward to the region of asteroid belt where meteorites come from, the ratio decrease to 1 to 2 orders magnitude less than the solar value and even depleted to 4 orders of magnitude less than the solar value in the case of the Earth. The spectral observation towards the atmosphere of white dwarf (Jura et al. 2012) also show a depleted carbon to silicon ratio. The strong gravity of white dwarfs are expected to pull the heavier elements from its atmosphere, and thus the detection of heavy elements are considered to be the impacts from some rocky bodies. A carbon poor with C/O ratios in the spectra of white dwarf are similar to those showing in chondritic meteorites in the solar system (Jura et al. 2012; Wilson et al. 2016). It indicates that the mechanisms to make the carbon depleted in the solar system might be universal and not only occur in the solar system. In the ISM, most of the carbon are stored in the solid forms, such as graphite and PAHs (Savage & Sembach 1996;Draine 2003), while the gradient of elemental abundance of carbon showing in the solar system hints the carbon should be in the gaseous form instead of solid before the formation of the planetesimals to account for the carbon depletion in the Earth and meteorites. This so-called carbon depletion problem will be further examine in Chapter 2.

Final is the nitrogen which shows the most depleted ratios within CNO, comparing to the solar value. All the objects in the solar system are depleted in nitrogen and it shows a gradient as well. As we approach the sun, the abundance of nitrogen decreases as temperature goes higher. This suggests that the majorities of the compounds carries nitrogen are in the volatile forms and the most likely candidates are NH_3, N_2 and N.

1.2.3 The Chemistry in Comets

In this subseciton, we focus on comets, the small objects in the solar system, which are thought to be made in the cold outer region of the protoplanetary disks. They are

considered to be relatively pristine leftovers from the early days of the solar system. The composition of which can be the link to the formation of the solar system if we assume comets do not undergo a major processing during the formation.

Figure 1.6 is the schematic illustration of process in the cometary coma. As comets approach the Sun, part of solar irradiation will be reflected away, part of it will be thermal radiated from the surface and the rest of it heat up nucleus, resulting the sublimation of ice on/under the surface and form the cometary coma. Once molecules sublimate from the surface, various gas-phase chemistry take place in the coma, within which photochemistry dominates the reactions as comets become closer to the sun.

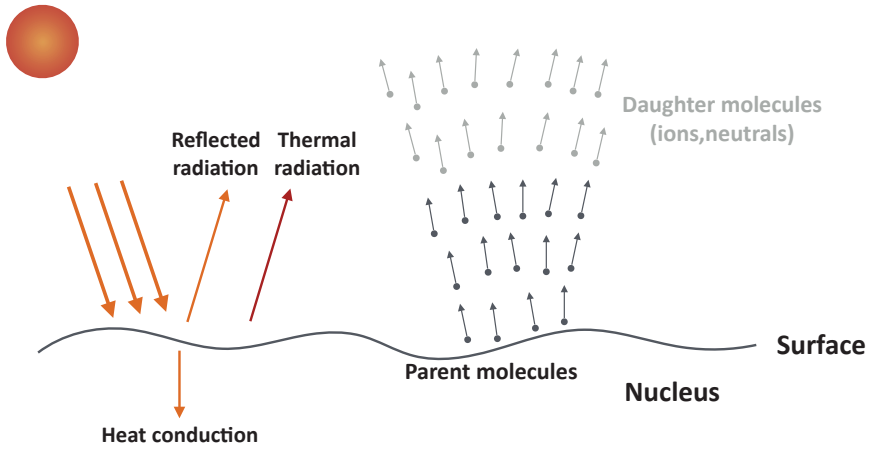

Figure 1.6: The schematic illustration of process in the cometary coma and surface energy balance.

Figure 1.7 shows the composition of the cometary coma (Mumma & Charnley 2011). The green bar represents the range of values found among the detection and the number of comets has been detected were shown in the end. As the figure shows, water ice is the primary composition of the coma. The following abundant species are CO and CO_2. The abundance ratios of the each molecule may change with heliocentric distance, depending on the sublimation temperature of different species as well as the nature of the nucleus. To date more than 20 parent molecules have been detected in cometary coma, including some complex species, e.g, H_2CO, CH_3OH, HCOOH, CH_3CN and so on. The composition of the cometary coma provide us a chance to understand the composition of the nucleus. However, retrieving the molecules in the cometary coma to the nucleus is challenging since once the parent molecular come out, they will get photodissoicated into small species so-called daughter molecules, making things more complicated. Therefore, tracing the origin

of the daughter molecules and translate their abundances to the parent molecules is even tricky (Le Roy et al. 2015). Thanks to Rosetta mission, we now have a chance to detect the surface of comet directly and opens the new era of cometary science.

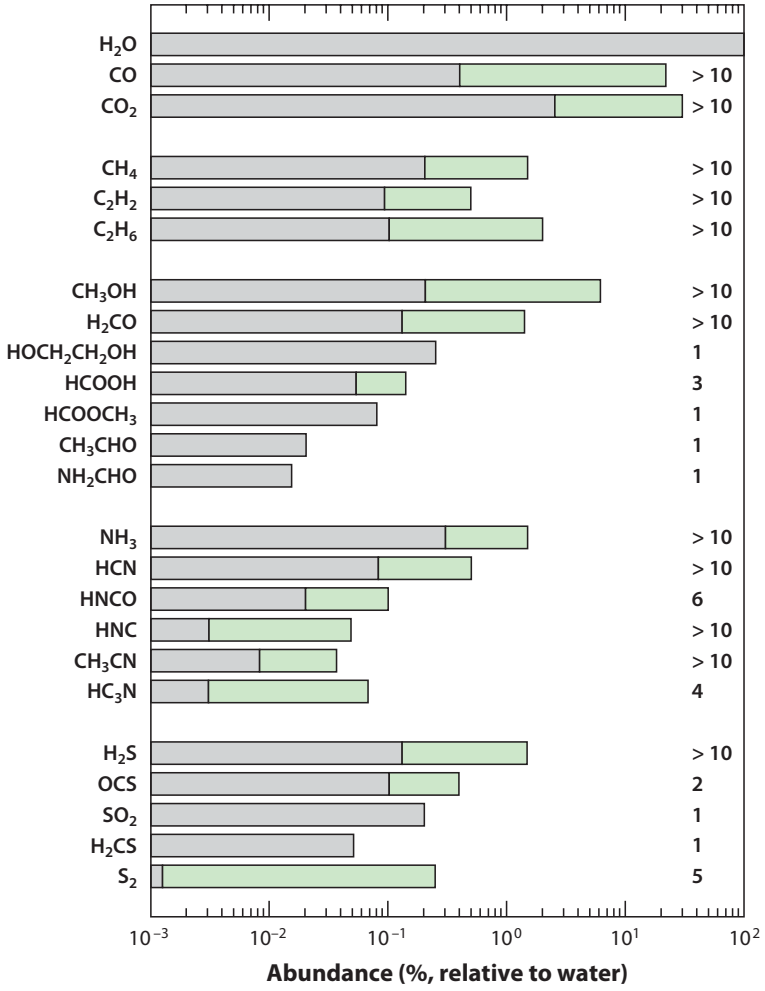

Figure 1.7: The table lists the chemical compositions detected in the cometary coma by the abundance ratio relative to water (Mumma & Charnley 2011).

1.2.3.1 Rosetta Mission and Comet 67P/C-G

Comet 67P/ Churyumov-Gerasimenko (67P/C-G), the destination of Rosetta mission, is a short-period Jupiter-family comet, which is thought to be originally formed in the Kuiper belt, extending from the orbit of Neptune $\sim$ 30 au to approximately 50 au. It was first detected in 1969 (Churyumov & Gerasimenko 1972). The orbital period and perihelion distance changed form 9.0 years and $\sim$ 2.7 au to the current period of $\sim$ 6.5 years and $\sim$ 1.3 au due to its close encounter with Jupiter (Krolikowska 2003).

Comet 67P/C-G includes two lobes connected by the narrow neck (See left panel of Figure 1.8).

Rosetta is an European Space Agency (ESA) mission, launched on 2 March 2004. After ten years journey traveling through the solar system. On 6 August 2014, the spacecraft reached it target, comet 67P/C-G, the heliocentric distance was around 3.5 au and it started a series of measurements towards the comet. In addition to the remote sensing, the lander Philae landed on the comet on 12 November 2014. Rosetta followed the comet through the perihelion $\sim$ 1.3 au, on August 2015 and continued orbiting it until the end of September 2016 (The corresponding orbital distance can be found in the right panel of Figure 1.8). It is the first time to land on the comet, having a long-term study of it. Rosetta chases the comet when it was far from the Sun until it become active caused by the solar irradiation and see how cometary activity changes with time (Groussin et al. 2015; Fornasier et al. 2019).

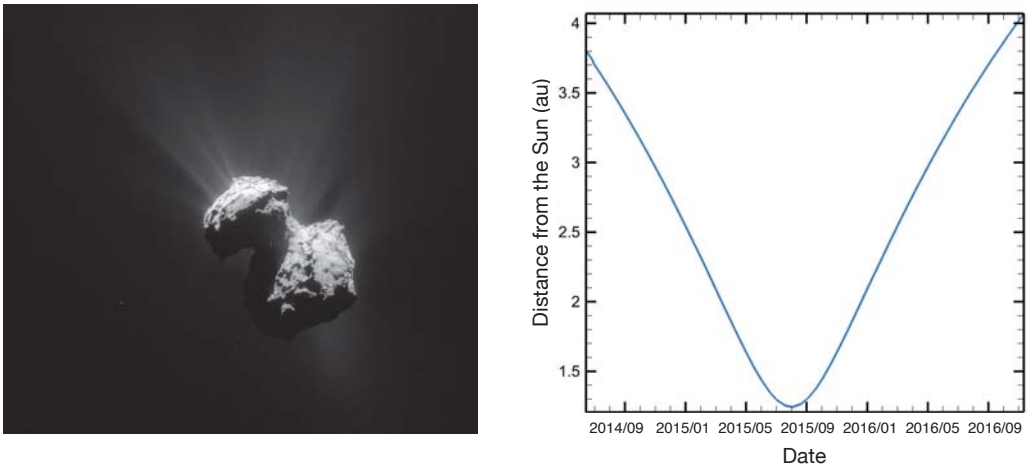

Figure 1.8: Left: Comet 67P/C-G taken on 7 July 2015 from a distance of 154 km from the comet centre (Credited by ESA - European Space Agency). Right: The orbital distance from the Sun of Comet 67P/C-G as a function of date.

There are several interesting things discovered by Rosetta mission. For example, the unexpected detection of O_2 in the cometary coma (Bieler et al. 2015). The abundance of O_2 ranges from 1 % to 10 % relative to H_2O, the third or fourth abundant species in the coma. The detection is surprising since O_2 ice is thought to be converted to water ice efficiently and hardly be preserved in the ice form stored in comets. The formation of O_2 have been discussed by many papers, such as Taquet et al. (2016), Mousis et al. (2016) and Dulieu et al. (2017). Also the instrument aboard the lander measured many organic compounds on the cometary surface, including

four first-time-detected species: methyl isocyanate, CH_3NCO, acetone, CH_3COCH_3, propionaldehyde, C_2H_5CHO, and acetamide, CH_3CONH_2 (Goesmann et al. 2015). Furthermore, the broad absorption feature centered at 3.2 μm in the cometary reflectance spectra were detected for the first time as well (Capaccioni et al. 2015). Besides, Rosetta measured the simplest amino acid, glycine in the cometary coma of 67P/C-G (Altwegg et al. 2016). It confirms the detection of glycine from Comet Wild-2 in sample returned by Stardust mission (Elsila et al. 2009).

1.3 Astrochemical model

To date, over hundreds of molecules have been detected in various environment from interstellar clouds, star forming regions to protoplanetary disks (Herbst & van Dishoeck 2009). The species detected in different places are related to the life cycle of the stars. They are constantly processed by different chemical reactions along different stages of stellar and planetary formation. Thus, chemical model plays an important role for us to understand and connect the observation between different stages.By coupling the simulation of chemical model with the radiative transfer, we can further make predictions for molecules that have not or cannot be directly observed.

From a numerical point of view, chemical models solve a system of differential equations as:

$$\frac{d[n_i]}{dt} = \Sigma(production) - \Sigma(destruction) \tag{1.1}$$

where n_i represents the number density (cm^{-3}) of species i. The production and destruction are the reactions related to species. The number equations depends on how many species being taking into account in the network. By setting the initial abundances of molecules and solving the series of differential equations, finally we can obtain the abundance evolution of each species. The elements are eventually stored in three forms: (1) the gas phase (2) refractory cores of interstellar grains and (3) the ice mantle covers on the refractory core. In astrochemistry, the reactions can be roughly divided into two types: gas-phase reactions occurring in the gas phase and grain-surface reactions taking place on the top of the ice mantle (Wakelam et al. 2013; Yamamoto 2017). At the low temperature (T≤100), gas-phase reactions are mostly dominated by exothermic reactions and the reactions without activation barriers such as the ion-molecule reactions which are reactions between a neutral molecule and positive charged molecule (or atom) and dissociate recombination, the reactions between positive charge ion and electron. However, gas-phase reactions itself can not

produce COMs observed in the space efficiently such as CH_3OH (Horn et al. 2004), raising up the importance of the grain-surface reactions. In the space, dust grains are important because they provide a surface to increase the possibility that species meet and react. Furthermore, dust grain can absorbed the excess energy created by the reactions. In contrast, the excess energy created by the gas-phase reactions have to be absorbed by the product and it can lead to immediate dissociation. Reactions on the surface are mainly between light atoms such as H, C and O when temperature < 20K. When temperature increase around 30-50K, not only light species, but heavier molecules can diffuse on the surface and form complex molecules. Thus, grain-surface reactions are crucial to enhance the molecular complexity. Last but not least, in the chemical model, we usually assumed that reactions hardly occur inside the ice mantle due to long diffusion timescale. However, recent researches (Theulé et al. 2013; Mispelaer et al. 2013; Ghesquière et al. 2015) question the conventional picture of the interstellar ice, suggesting reactions might occur inside the ice mantle with the efficiency higher than we expected.

Here we briefly mention how chemical models deal with gas-phase and solid phase. The models can be separated into two-phases model, three-phases model and multi-layers model (see Figure 1.9). The most different part is the way to define the reactive ice bulk. For example, since the surface reaction only occurs on the top most layer, three-phase model separates gas-phase (the striped circle), surface-phase (the white circle) and mantle phase (the black circle), and thus only the species in the surface-phase can do the grain-surface reactions. The first three-phase model was by Hasegawa & Herbst (1993) and after there are several modified version such as Garrod et al. (2008) and Fayolle et al. (2011). In the case of two-phase model, there is no distinguish between surface and mantle and thus all the species in the icy-phase can do the grain-surface reactions under the constrained of fraction between the amount of active layer and the total ice mantle (Aikawa et al. 1996). Finally, the multiple layer model such as Taquet et al. (2012), can trace the species between different layers and grain-surface reactions can occurs in different layers, providing us a more accurate results when comparing to the observation. However, it is time-consuming comparing to two- or three-phase models. Taking into account the computation time, the suitable treatments depends on the issues we want to solve. For example, if the species are less affected by grain surface reactions, two phase model is sufficient enough to take the calculation. On the other hand, if species are effected by grain-surface reactions a lot, three-phase model or even multiple layers model should be considered.

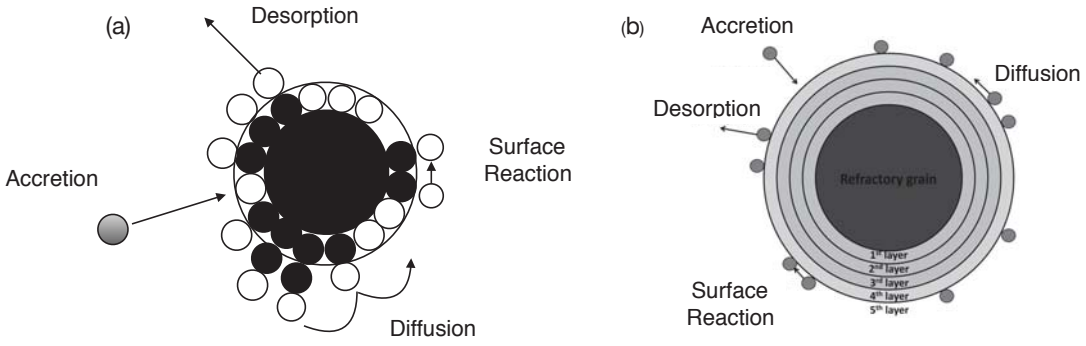

Figure 1.9: The schematic view of (a) three-phase model (modified from Hasegawa & Herbst 1993) and (b) multi-layer model (modified from Taquet et al. 2012).

1.4 About this thesis

Since Protoplanetary disks are analogue of the proto-Solar Nebula, the birthplace of planets and small bodies. This thesis treats two topics which chemically connect protoplanetary disks with the Solar system objects by means of calculations of chemical reaction network. In Chapter 2, we focus on the inner region of the solar system, aiming to understand carbon deficit on Earth and the asteroid belt. We examined the effect of carbon grain destruction on disk chemistry and further made a prediction of molecules which can possibly be detected by ALMA. In Chapter 3, we studied the formation of COMs through mantle reactions, taking into account the effect of FU Ori outbursts, focusing on the comet forming region, namely the outer region of the disk. We aimed to reproduce the materials newly detected in the Comet 67P/C-G by Rosetta mission. In addition, we discussed about the influence of the carbon grain destruction on the formation of COMs. In the Chapter 4, we summarized the results based on previous chapters and we issued the future prospects to further improve our works.

Chapter 2

The Effect of Carbon Grain Destruction in the Protoplanetary Disks

Modified from Wei et al. (2019)

2.1 Introduction

The protoplanetary disks (PPD) around low-mass stars are analogs of the solar nebula. Disks are composed of dust and gas surrounding a central pre-main-sequence star. As dust grains settle down to the midplane, they collide, grow and form planetesimals. These are the ingredients which form rocky planets, the cores of gas-giant planets and small bodies in our solar system. Therefore, the composition of rocky bodies contain information on the refractory materials available during the formation of solar system and provide clues on both the local and large-scale chemical and physical processes in disks.

Figure 2.1 shows that the abundance of carbon relative to silicon has clear variances across the solar system bodies (e.g., Geiss 1987; Lee et al. 2010; Pontoppidan et al. 2014; Bergin et al. 2015; Anderson et al. 2017; Bardyn et al. 2017). The similar amount of carbon relative to silicon in the Sun and ISM suggests that this value is representative of the ratio at the beginning of the formation of the planets. Although the surface of our Earth is covered with organic compounds, including even live organisms, if one excludes the uncertain amount of carbon in the core, the Earth BSE value (Bulk Silicate Earth: includes only ocean, atmosphere and silicate mantle) is 4 orders of magnitude lower than the solar ratio. Even when taking into account that some light elements, including carbon, are possibly incorporated inside the core of Earth, the abundance ratio remains significantly lower than solar (Allègre et al. 2001). In the asteroid belt, the amount of carbon in meteorites relative to silicon is 1 to 2 orders of magnitude less than the solar value. Moving farther out, to the comet region, the carbon fractions become again comparable to that in the Sun. The C/Si ratio shows a clear correlation with heliocentric distance. Highly depleted elements in the solar system imply that they were in a phase too volatile to condense, and as such, they were not incorporated into planetesimals. Thus any gaseous carbon species which did not freeze onto the surface of grains nor become incorporated into refractory organic material will be either accreted onto the central star or dispersed out of the disk. In contrast, refractory carbon or carbon contained in ice mantles would have been incorporated into solid bodies producing, for example, the solar-like carbon abundance relative to silicon seen in comets.

The described trend of carbon depletion in the solar system is a long-standing problem in the community (Geiss 1987; Lee et al. 2010; Pontoppidan et al. 2014; Bergin et al. 2015; Anderson et al. 2017). This is the so-called carbon deficit problem. This issue exists not only in the solar system but also in white dwarf systems (Jura

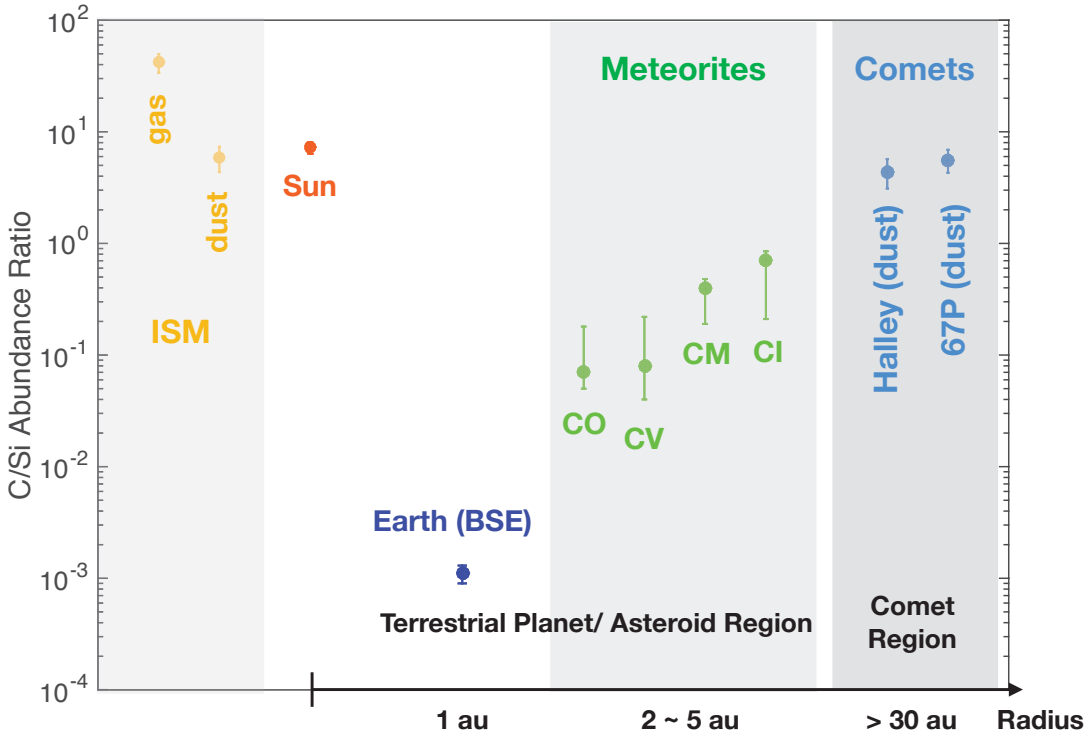

Figure 2.1: The carbon to silicon abundance ratio with error bars in the protosun (Lodders 2010), Earth, four classes of carbonaceous chondritic meteorites (CI, CO, CM and CV; Bergin et al. 2015), cometary dust of Halley (Jessberger et al. 1988) and 67P/C-G (Bardyn et al. 2017), and ISM (Bergin et al. 2015).

2006). Therefore, the cause might be universal throughout the Galaxy. In the ISM about 60% of carbon is in the form of either graphite, amorphous carbon grains, or polycyclic aromatic hydrocarbons (PAHs) (Savage & Sembach 1996;Draine 2003). If the solar system inherited ISM-like material, then refractory carbon must have been destroyed prior to planetary formation to account for the observed carbon depletion. Some possible ways to destroy carbon grains have been discussed: (1) carbon can be released from the solid to the gas phase by hot oxygen atoms, if the gas temperature is higher than 500 K and the grain size is within 0.1-1 μm (Lee et al. 2010). (2) carbon aggregates such as graphite can react with oxygen-bearing species, e.g., OH (Finocchi et al. 1997; Gail 2001; Gail 2002). (3) PAH destruction by X-ray and extreme ultraviolet (EUV) photons (Siebenmorgen & Krügel 2010).

In this study, we calculate the chemistry in protoplanetary disks taking into account carbon grain destruction in the inner region to study how it affects the molecular abundance distribution in the disk. We compare the results between cases with and without carbon grain destruction, finding the candidate species which have the largest variations in abundance between two cases. To investigate whether or not the

effect of carbon grain destruction is observable with ALMA, we perform the radiative transfer calculations of molecular line emission from identified species in T Tauri and Herbig Ae disks.

We describe our disk model and the radiative transfer calculations in Section 2.2. The results and discussion are presented in Section 2.3. Section 2.3.1 presents the effect of carbon grain destruction on the molecular abundances and distributions (HCN, CH_4, C_2H_2, c-C_3H_2 carbon-chain molecules, H_2O, OH, O_2 and CO_2). Section 2.3.2 discusses the radial distribution of the solid carbon fraction in the disk in our model in comparison with the solar system, and Section 2.3.3 presents the prediction for ALMA observation based on our calculations. We summarize and state the conclusions of this work in Section 2.4.

2.2 Methodology

2.2.1 Physical Model

We use physical models of protoplanetary disks generated using the methodology described in Nomura & Millar (2005) with the addition of X-ray heating as described in Nomura et al. (2007). We model an axisymmetric Keplerian disk and two types of central stars are considered. The first is a typical T Tauri star with mass, M_* = 0.5 $M_\odot$, radius, R_*= 2.0 $R_\odot$, and effective temperature, T_*= 4000 K (Kenyon & Hartmann 1995). The second is a Herbig Ae star with mass, M_*= 2.5 $M_\odot$, radius, R_*= 2.0 $R_\odot$, and effective temperature, T_*= 10,000 K (e.g., Palla & Stahler 1993).

The gas density profiles are determined by assuming vertical hydrostatic equilibrium, the balance between gravity and the pressure gradient force. In order to obtain the gas surface density profiles, we adopt the viscous α-disk model (Shakura & Sunyaev 1973), with a viscous parameter, $\alpha = 10^{-2}$ and a mass accretion rate, $\dot{M}$ = 10^{-8} $M_\odot$ yr^{-1}. The temperature profile of the gas is calculated self-consistently with the gas density profiles by assuming local thermal balance between gas heating and cooling. The thermal processes of heating from X-ray ionization of hydrogen, grain photoelectric heating induced by far-ultraviolet photons and cooling via gas-grain collisions and line transitions are taken into account. The dust temperature profiles are obtained by assuming local radiative equilibrium between the blackbody emission of grains and the absorption of radiation from the central star as well as the surrounding dust grains.

Regarding dust, we assume that the dust and gas are well-coupled and that the dust-to-gas mass ratio is constant (0.01) throughout the disk. The dust size distribution model in Weingartner & Draine (2001), which reproduces the observational extinction curve of dense clouds, is adopted. The dust properties are important factors for both gas and dust temperatures. The adopted dust opacity is described in Appendix D of Nomura & Millar (2005).

For the UV radiation field two radiation sources are taken into account: radiation from the central star and the interstellar medium. In the case of the T Tauri star, we use a UV excess model that reproduces the observational data toward TW Hydrae. The components of the stellar UV radiation are blackbody emission, hydrogenic thermal Bremsstrahlung emission and Lyα line emission (see Appendix C of Nomura & Millar 2005 for details). For the Herbig Ae star, the UV excess contributes a significantly smaller fraction to the total UV luminosity compared with that from the stellar blackbody radiation (e.g., Dent et al. 2013). Therefore, we use only the blackbody emission of the central star as the source of UV radiation field for the Herbig Ae model. For the X-ray radiation, we adopt a TW-Hydrae-like spectrum with a total luminosity, $L_X \sim 10^{30}$ ergs^{-1}, for the T Tauri star (Preibisch et al. 2005). Due to the non-convective interiors of Herbig Ae stars, the typical X-ray luminosities are ≥ 10 times lower than those of T Tauri stars (Güdel & Nazé 2009). Therefore, we assume an X-ray spectrum with $L_X \sim 3 \times 10^{29}$ erg s^{-1} and $T_X \sim 1.0$ keV for the Herbig Ae star based on observations (e.g., Zinnecker & Preibisch 1994; Hamaguchi et al. 2005).

For full details on the generation of the physical models, see Nomura & Millar (2005) and Nomura et al. (2007). The total grid numbers are 8699 and 12116 for the disks around T Tauri and Herbig Ae stars, respectively, where 129 radial steps are taken logarithmically for the disk radius from 0.04 to 305 au. Figure 2.2 shows the physical structure of the disk around the T Tauri star and the Herbig Ae star (see also Walsh et al. 2015; Notsu et al. 2016, 2017). From top, the gas number density decreases as the function of height and the radius. The densest region reaches about 10^{15}cm^{-3} near the disk midplane, falling to 10^5cm^{-3} in the surface layer, showing the diversity of the environment in the PPDs. The gas and dust temperature decouple in the diffuse region due to inefficient collisions between the gas and dust grains. As the density increases toward the disk midplane, the gas and dust temperature become well coupled. The UV flux from the central star is much stronger in the case of Herbig Ae star (right-hand-side) than in the T-Tauri star (left-hand-side). However, both UV and X-ray photons are absorbed by dust and gas and do not penetrate to the midplane. Since the Herbig Ae star has a higher luminosity, its enhanced gas and

dust temperatures make line emission easier to detect than in the T Tauri case (see Section 2.3.3). Noted that different radial ranges are shown in Figure 2.2 for each type of disk.

2.2.2 Chemical Network

We use a chemical reaction network, containing both gas-phase reactions and gas-grain interactions to study the chemical evolution of the disks. In order to examine the effect of carbon grain destruction (Lee et al. 2010; Anderson et al. 2017), we focus on those small molecules that are not much affected by grain surface reactions and consider two initial values for the elemental abundance of carbon. Except the abundance of carbon, for both models without and with carbon grain destruction, we use the typical low-metal value often adopted to model the chemistry of dark clouds such as TMC-1 (Table 8 of Woodall et al. 2007; see also Table 2.1). In the model without carbon grain destruction, the elemental abundance of carbon in gas is the same as that in diffuse clouds, in which the gas-phase elemental abundance of carbon is lower than that of oxygen. For the model with carbon grain destruction, we consider an extreme case assuming that all the carbon in the grains is destroyed and released into the gas-phase, and set the abundance for ionized carbon to be the solar abundance of carbon, $C^+ = 2.95 \times 10^{-4}$ (e.g., Asplund et al. 2009; Draine 2011). In this case, the gas-phase elemental abundance of carbon is larger than that of oxygen. We note that the C/O ratio is larger than unity in the gas-phase in this extreme case, although the C/O ratio of the solar photosphere is around 0.5 (Allende Prieto et al., 2002). This is because a large fraction of available elemental oxygen is incorporated into silicate grains which are more difficult to destroy than carbon grains. According to Lee et al. (2010), if the grain size is small enough, carbon grains could be sputtered into the gas phase in the surface layer of the disks where the gas temperature is high. If turbulent mixing in the vertical direction of the disk is efficient enough, a significant amount of the small carbon grains could be sputtered inside a disk radius of around 10 au in the case of T Tauri disks. Therefore, in this paper we only consider chemistry in the very inner region and treat the T Tauri disk up to 10 au, and the Herbig Ae disk, which the UV irradiation is stronger, up to 50 au. We calculate the chemical evolution up to 10^6 years, which is the typical life time for protoplanetary disks and at which point the chemical structure has almost reached steady state in the disk. We note that for a more realistic model, the evolution of physical conditions, such as density, temperature, and radiation field, should be treated together with the time evolution of molecular abundances. This is beyond the scope of this work, and for

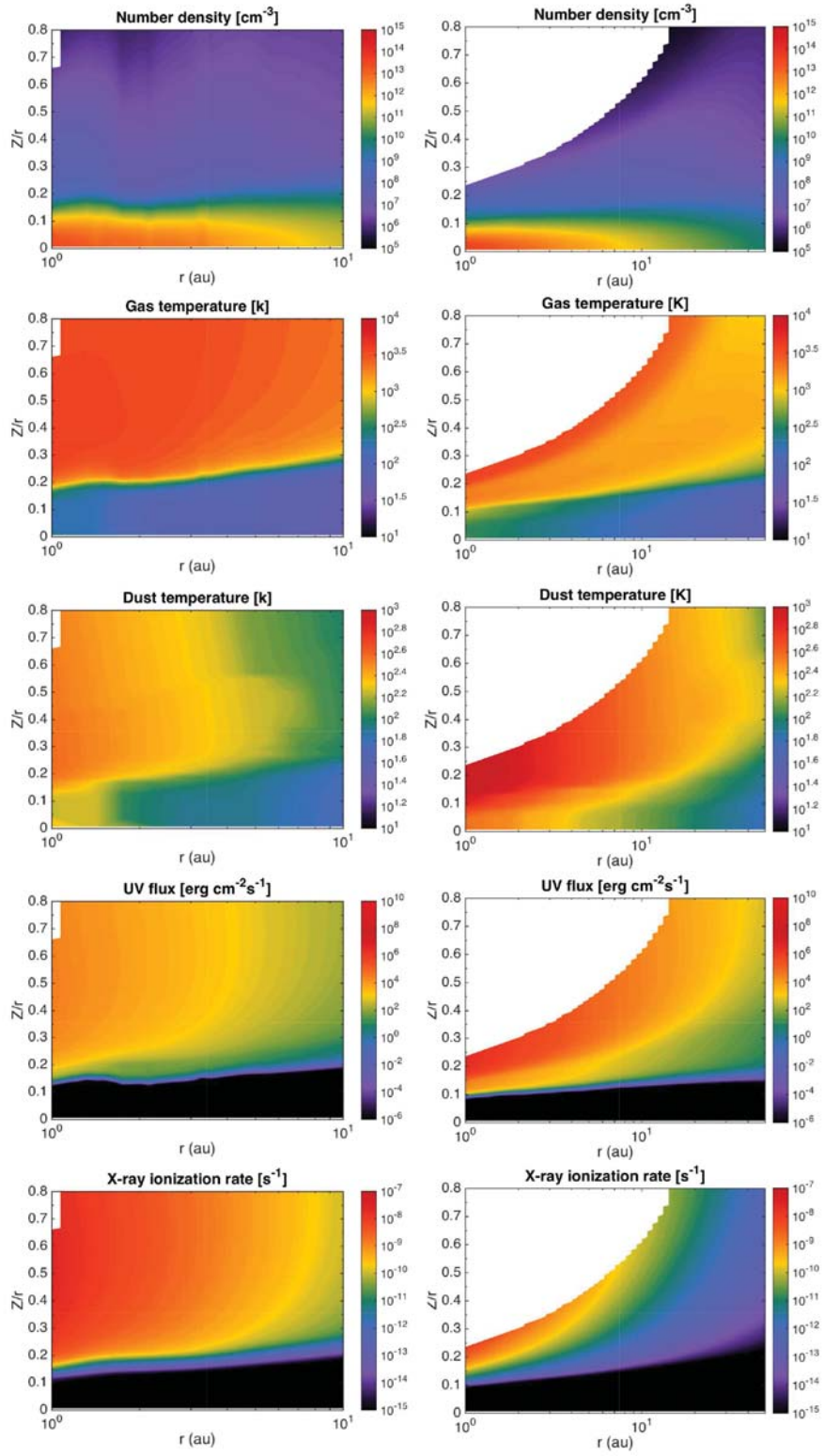

Figure 2.2: The gas number density, gas temperature, dust temperature, UV flux and X-ray ionization rate as a function of radius and height divided by the radius (Z/r) for the T Tauri disk (left-hand-side) and the Herbig Ae disk (right-hand-side). Noted that the radial ranges are different between the two disks.

simplicity, we use the chemical composition of diffuse clouds as an initial condition, and use the fixed physical conditions of each protoplanetary disk for the calculation of chemical reactions. Also, and again for simplicity, we ignore the change in the dust mass and surface area caused by the carbon grain destruction and the freeze-out of gas-phase molecules on grains during the calculation of chemical reactions.

Element	Abundance	
	Without C grain destruction	With C grain destruction
He	0.14	
C^+	7.30×10^{-5}	2.95×10^{-4}
N	2.14×10^{-5}	
O	1.76×10^{-4}	
Na^+	3.00×10^{-9}	
Mg^+	3.00×10^{-9}	
Si^+	3.00×10^{-9}	
S^+	2.00×10^{-8}	
Cl^+	3.00×10^{-9}	
Fe^+	3.00×10^{-9}	

Table 2.1: The initial gas-phase elemental abundances relative to total hydrogen nuclei in the model without carbon grain destruction. For the model with carbon grain destruction, we adopt a carbon abundance of $C^+=2.95 \times 10^{-4}$.

2.2.2.1 Gas-phase Reactions

We use the RATE06 release of the UMIST Database for Astrochemistry, for the gas-phase chemistry (Woodall et al. 2007). In this chemical network, there are 375 species and 4336 reactions, including 3957 two-body reactions, 214 photoreactions, 154 X-ray/cosmic-ray-induced photoreactions, and 11 reactions of direct X-ray/cosmic-ray ionization. Since the reactions including fluorine, F, and phosphorus, P, have a low impact on the chemistry (Walsh et al. 2010), we remove reactions containing these two elements to reduce the computation time. For the photoreactions, we calculate the UV radiation at each point in the disk as

$$G_{FUV}(r,z) = \int_{912\text{Å}(13.6eV)}^{2068\text{Å}(6eV)} G_{FUV}(\lambda,r,z)d\lambda. \quad (2.1)$$

The UV radiation is scaled by the interstellar UV flux, $G_0 = 2.67 \times 10^{-3}$ erg cm^{-2}s^{-1} (van Dishoeck et al. 2006), and photoreaction rates at each point in the disk can be approximated as

$$k^{ph}(r,z) = \frac{G_{FUV}(r,z)}{G_0} k_0 \quad s^{-1}, \tag{2.2}$$

where k_0 is the unshielded photoreaction rates due to the interstellar UV radiation field as compiled in RATE06 (see also Millar et al. 1997).

2.2.2.2 Gas-grain Interactions

The gas-grain interactions included are the adsorption (freeze-out) and desorption of molecules on and from dust grain surfaces, respectively. When the gas temperature is low enough, the adsorption rate becomes larger than the desorption rate, and therefore, molecules freeze onto dust grains. Otherwise, molecules sublimate from dust grains and into the gas-phase, so-called "thermal desorption". The rate of thermal desorption, and thus the temperature at which sublimation happens, will depend on the binding energy of each molecule to dust grains. The binding energies of several important molecules and adopted in their work are listed in Table 2.2. In addition to thermal desorption, we consider non-thermal desorption mechanisms: cosmic-ray-induced thermal desorption (Leger et al. 1985; Hasegawa & Herbst 1993) and UV photodesorption (Westley et al. 1995; Willacy & Langer 2000; Öberg et al. 2007). The details of reaction rates for these processes can be found in the Appendix 2.5.1 (see also Walsh et al. 2010; Notsu et al. 2016).

Considering the processes of freeze out, thermal desorption, cosmic-ray-induced desorption and photodesorption, the differential equation for the number density of species i on the dust grain is written as (e.g., Hasegawa et al. 1992)

$$\frac{dn_{i,ice}}{dt} = n_i k_i^a - n_{i,ice}^{desorb}(k_i^d + k_i^{crd} + k_i^{pd}), \tag{2.3}$$

where k_i^a is the adsorption rate, k_i^d is the thermal desorption rate, k_i^{crd} represents the cosmic-ray-induced thermal desorption rate, and k_i^{pd} denotes the photodesorption rate of species i. n_i is the gas phase number density of species i and $n_{i,ice}^{desorb}$ is the number density of species i located in uppermost active layers of the ice mantle. The value of $n_{i,ice}^{desorb}$ is given by (Aikawa et al., 1996) as

$$n_{i,ice}^{desorb} = \begin{cases} n_{i,ice} & (n_{ice} < n_{act}) \\ n_{act}\frac{n_{i,ice}}{n_{ice}} & (n_{ice} \geq n_{act}) \end{cases} \tag{2.4}$$

where n_{ice} is the total ice number density of all species (see also Walsh et al. 2014) and n_{act}=$4\pi r_d^2 n_d n_s N_{LAY}$ represents the number of active surface sites in the ice mantle per unit volume and N_{LAY} is the number of surface layers considered as active, assumed

to be two. r_d is the dust grain radius, n_s represents the surface density of sites and n_d is the number density of dust grains. For more detail, please refer to Appendix 2.5.1.

2.2.3 Radiative Transfer and the Line Emission

In order to predict observational signatures of carbon grain destruction in the inner region of protoplanetary disks, we perform ray-tracing calculations to estimate the intensity of molecular line emission and obtain intensity maps for both models with and without carbon grain destruction. The line data are taken from the Leiden Atomic and Molecular Database (LAMDA, Schöier et al. 2005), the Cologne Database for Molecular Spectroscopy (CDMS, Müller et al. 2005), or the Jet Propulsion Laboratory (JPL) molecular spectroscopic database (Pickett et al. 1998). We modify the original 1D code, RATRAN (Hogerheijde & van der Tak 2000) to calculate the ray-tracing using an axisymmetric 2D disk structure under the assumption of local thermodynamic equilibrium (LTE).

The intensity of the line profile at a frequency ν, $I_{ul}(\nu)$, is obtained by solving the radiative transfer equation along the line-of-sight s in the disk

$$\frac{dI_{ul}(\nu)}{ds} = -\chi_{ul}(\nu)(I_{ul}(\nu) - S_{ul}(\nu)) \tag{2.5}$$

where $\chi_{ul}(\nu)$ is the total extinction coefficient of dust grains and molecular lines and $S_{ul}(\nu)$ is the source function given by

$$\chi_{ul}(\nu) = \rho_d \kappa_{ul} + \frac{h\nu_{ul}}{4\pi}(n_l B_{lu} - n_u B_{ul})\Phi_{ul}(\nu) \tag{2.6}$$

and

$$S_{ul}(\nu) = \frac{1}{\chi_{ul}(\nu)} \frac{h\nu_{ul}}{4\pi} n_u A_{ul} \Phi_{ul}(\nu) \tag{2.7}$$

respectively, where A_{ul} and B_{ul} are the Einstein A and B coefficients for spontaneous and stimulated emission and B_{lu} is the Einstein B coefficient for absorption. n_u and n_l are the number densities of the molecules in the upper and lower levels, respectively. ρ_d is the mass density of dust grains where we simply apply the dust to gas mass ratio of $\rho_d/\rho_g = 1/100$. κ_{ul} is the dust absorption coefficient at a frequency ν_{ul} and h is Plank's constant.

Here $\Phi(\nu)$ is the line profile function which is affected by thermal broadening and Keplerian rotation in the disk. As a result, $\Phi(\nu)$, is given by

$$\Phi_{ul}(\nu) = \frac{1}{\Delta\nu_D \sqrt{\pi}} \exp\left[\frac{-(\nu + \nu_K - \nu_{ul})^2}{\Delta\nu_D^2}\right], \tag{2.8}$$

where $\Delta\nu_D = (\nu_{ul}/c)\sqrt{2k_BT_g/m_i}$ is the Doppler width, c is the speed of light, T_g represents the temperature of gas and m_i is the mass of the species, i. ν_K denotes the Doppler shift due to the projected Keplerian velocity along the line-of-sight and is given by

$$\nu_K = \frac{\nu_{ul}}{c}\sqrt{\frac{GM_*}{r}}\sin\phi\sin\theta, \tag{2.9}$$

where G is the gravitational constant, M_* is the mass of the central star, r is the distance of the line emitting region from the central star, ϕ is the azimuthal angle between the semimajor axis and the line linking the point in the disk along the line of sight and the center of the disk, and θ is the inclination angle of the disk.

In order to predict the observable flux density, we integrate Equation 2.5 along the line of sight s. The intensity at (x, y) in the projected plane is given by

$$I(x, y, \nu) = \int_{-s_\infty}^{s_\infty} j_{ul}(s, x, y, \nu)\exp(-\tau_{ul}(s, x, y, \nu))ds, \tag{2.10}$$

where j_{ul} is the emissivity at the position (s, x, y) and frequency ν, given by

$$j_{ul}(s, x, y, \nu) = n_u(s, x, y)A_{ul}\frac{h\nu_{ul}}{4\pi}\Phi_{ul}(s, x, y, \nu), \tag{2.11}$$

and $\tau_{ul}(s, x, y, \nu)$ is the optical depth from the line emitting point s to the disk surface s_∞ at the frequency ν, expressed by

$$\tau_{ul}(s, x, y, \nu) = \int_{s}^{s_\infty} \chi_{ul}(s', x, y, \nu)ds'. \tag{2.12}$$

The observable line flux integrated all over the disk is given by

$$F_{ul}(\nu) = \frac{1}{4\pi d^2}\iint I(x, y, \nu)dxdy, \tag{2.13}$$

where d is the distance between the observer and the target object.

2.3 Result and Discussion

2.3.1 Effect of carbon grain destruction on molecular abundance distribution

In this subsection, we show effect of carbon grain destruction on carbon-bearing species (HCN, CH_4, C_2H_2, carbon-chain and hydrocarbon molecules) and oxygen-bearing species (H_2O, OH, O_2 and CO_2), some of which have been detected in protoplanetary disks at infrared wavelengths (e.g., Carr et al. 2004; Lahuis et al. 2006; Carr & Najita 2008; Salyk et al. 2008; Pascucci et al. 2009; Gibb et al. 2007). Here we mainly focus on the T Tauri disk model as an analogue of our solar system.

First, in order to see how the physical properties affect the molecular abundance profiles, the top panels of Figure 2.3 show the number density of hydrogen nuclei, the gas temperature and dust temperature as a function of height divided by radius (Z/r) at a disk radius of 1 au (left), 3 au (middle) and 10 au (right). The bottom panels show similar plots for the UV flux, the X-ray ionization rate and the cosmic-ray ionization rate.

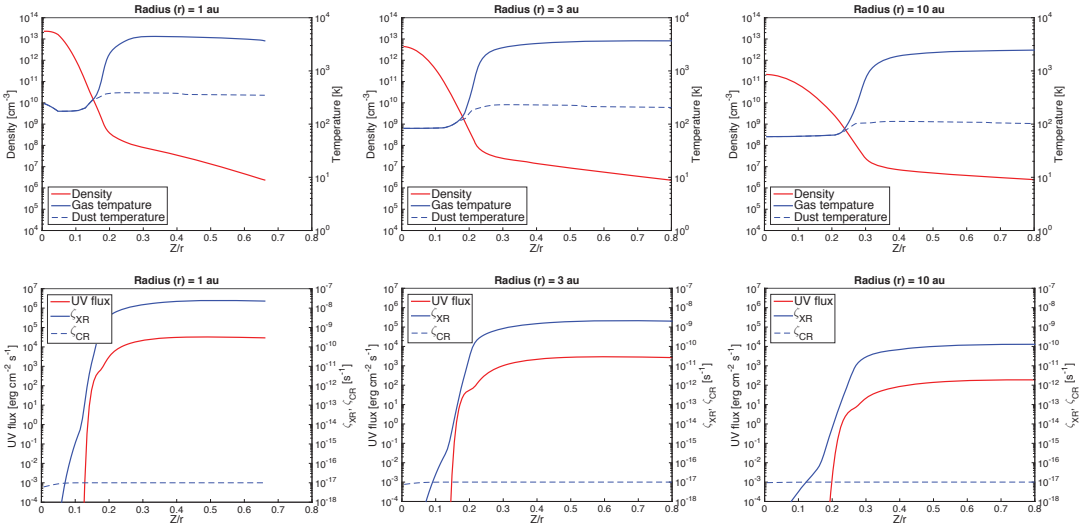

Figure 2.3: The top panels are number density of hydrogen nuclei (red line), the gas temperature (blue solid lines) and dust temperature (blue dashed lines) as a function of height divided by radius (Z/r) at a disk radius of 1 au (left), 3 au (middle) and 10 au (right). The bottom panels show the UV flux (red line), X-ray ionization rate (blue solid lines) and the cosmic-ray ionization rate (blue dashed lines) as a function of height divided by radius (Z/r) at a disk radius of 1 au (left), 3 au (middle) and 10 au (right) for a T Tauri disk.

Since gas-phase molecular abundances change dramatically across their snow-lines, we estimate the location of the snowlines of some molecules by equating the

adsorption rate (Equation 2.17) with the desorption rate (Equation 2.18). Because thermal desorption rate is related to the binding energy, Table 2.2 presents the location of the snowline of each species together with binding energies adopted in the model.

Molecule	Binding Energy (K)	Snowline in T-Tauri Disk (au)	Snowline in Herbig Ae Disk (au)
CO	855	>10	>50
CH_4	1080	>10	>50
C_2H_2	2400	9.33	>50
CO_2	2990	5.34	37.65
C_5	3220	2.66	32.75
C_6	3620	2.48	24.77
C_6H	3880	2.31	21.54
HCN	4170	2.31	18.74
C_7	4430	2.15	17.48
C_8	4830	2.01	14.18
H_2O	4820	2.01	14.18
HCOOH	5000	2.01	13.22
C_9	5640	1.75	10.00
C_{10}	6000	1.52	8.70

Table 2.2: The locations of the snowlines in T-Tauri and Herbig Ae disks determined by the temperature profiles given in Figure 2.2.

Figures 2.4, 2.6, 2.8 and 2.10 show molecular abundances relative to total hydrogen nuclei in both the gas-phase and ice mantle at 10^6 years as a function of (Z/r) at the disk radii of 10 au, 3 au and 1 au. The dashed and the solid lines represent the case without and with carbon grain destruction, respectively. Figures 2.5, 2.7, 2.9 and 2.11 display the 2-dimensional fractional abundances of gas-phase and ice mantle molecules as a function of radius and height, out to a maximum radius of 10 au since the destruction of carbon grains mainly occurs in the inner hot region only. In the latter set of figures, the left-hand-side plots represent the case without carbon grain destruction (C/O<1) and right-hand-side plots those with carbon grain destruction (C/O>1).

Since the abundance of gas-phase CO has a large effect on molecular abundances differences between the models with and without the carbon grain destruction, as is shown below, we present first the gas-phase and ice mantle abundances of CO (Figure 2.4). In the disk surface, CO gas is dissociated by the FUV photons so that oxygen and carbon are not locked in CO but are mostly in the form of atoms and ions since the synthesis of molecules is difficult due to the high flux of FUV photons. Figure

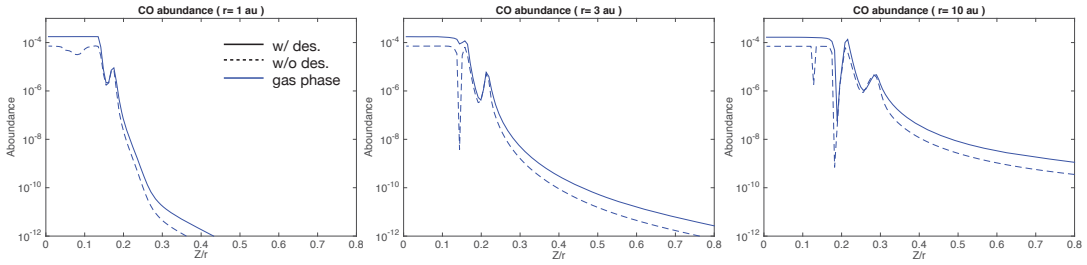

Figure 2.4: The fractional abundance of CO as a function of height divided by radius (Z/r) at a disk radius of 1 au (left), 3 au (middle) and 10 au (right). The blue lines show CO gas and light blue lines show CO in ice mantle for a T Tauri disk. Solid and dashed lines represent the model with and without carbon grain destruction, respectively.

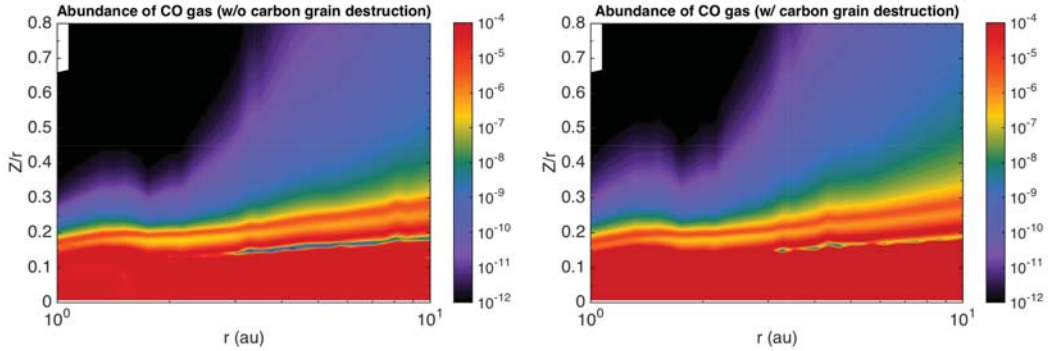

Figure 2.5: The 2-dimensional abundance distribution of gas-phase CO for the models without (left) and with (right) carbon grain destruction as a function of radius and height of the disk for a T Tauri disk. A detailed explanation of CO gas depletion layers can be found in Sec. 2.3.1.

2.5 shows the global CO abundance distribution, and CO is abundant (x(CO)=10^{-4}) throughout the whole region near the midplane, since it is easily desorbed inside 10 au due to its low binding energy. The abundance of CO increases slightly when carbon grains are destroyed, due to the additional elemental carbon now available in the gas phase.

The abundances of other molecules, however, are significantly affected by the gas-phase elemental C/O abundance ratio, especially in the region where CO gas is abundant. In general, carbon-bearing molecules are not expected to be very abundant in an oxygen-rich environment (C/O<1) since most of the carbon is incorporated into CO. However, in the carbon grain destruction regions, excess carbon exists (C/O>1) and carbon-bearing molecular abundances can increase dramatically. This type of chemistry is similar to that observed and successfully modeled around carbon-rich

AGB stars, such as IRC+10216 (e.g., Millar & Herbst 1994; Glassgold 1996).

Figure 2.6 shows 1D plots of the abundances of some carbon-bearing species (HCN, CH_4, C_2H_2 and c-C_3H_2). The left and right panels show the molecular abundances in gas and ice, respectively. Figure 2.7 shows the 2-D abundance distribution of the carbon-bearing species. The effects of carbon grain destruction, and the resulting chemistry, are different between the surface and the midplane. Near the midplane, carbon-bearing molecules can form efficiently via gas-phase reactions in the carbon-rich case. The most significant difference between two cases appears in HCN especially inside $\sim$ 2 au, near the HCN snowline. Due to its high binding energy (see Table 2.2), HCN can remain on dust grains beyond 2 au in the T Tauri disk. In the carbon-rich case, the peak gas-phase abundance of HCN is $\sim 10^{-5}$ near the midplane of the inner region. Near the midplane inside 2 au, the maximum differences between two cases can reach 8 orders of magnitude. In the oxygen-rich case, the peak abundance is $\sim 10^{-7}$ in the molecular layer. Therefore, HCN appears to be a good tracer of the effect of carbon grain destruction within its snowline, and we will focus on it in section 2.3.3. We note, however, that the abundance distribution of HCN could be affected by the initial abundance of species and the ingredients adopted in the chemical model (see e.g., Figure 14 of Walsh et al. 2015).

Similar behavior can be seen in CH_4 and C_2H_2, but the differences are less significant. The snowlines of CH_4 and C_2H_2 are located outside 10 au and around 9.3 au, respectively. The gas phase abundances of both molecules increase near the midplane inside the snowlines in the carbon-rich case. However, inside 2 au, most of the carbon is incorporated into HCN and long carbon-chain species in the gas-phase (see Figure 2.8 and Figure 2.9) and the abundances of CH_4 and C_2H_2 gas decrease here. We note that CH_4 is more abundant than HCN and carbon-chain molecules in the gas-phase near the midplane inside 2 au in the oxygen-rich case. In the oxygen-rich case CH_4 gas has its peak abundance ($\sim 10^{-7}$) in the molecular layer. In the case of c-C_3H_2, it shows a differences of about 7 orders of magnitude between two cases. Though it is less abundant than HCN, we treat c-C_3H_2 as a possible tracer in section 2.3.3 as well. We note that though the reaction network used here treats c-C_3H_2 and l-C_3H_2 separately, we should be cautious that there are some uncertainties since it is rarely possible to identify the specific isomeric products in a laboratory reaction and we need to rely on some calculations about energetics of the product and so on. Nevertheless, the model calculations show quite good agreement with observations of c- and l-C_3H_2 in IRC+10216 and TMC-1 (McElroy et al. 2013).

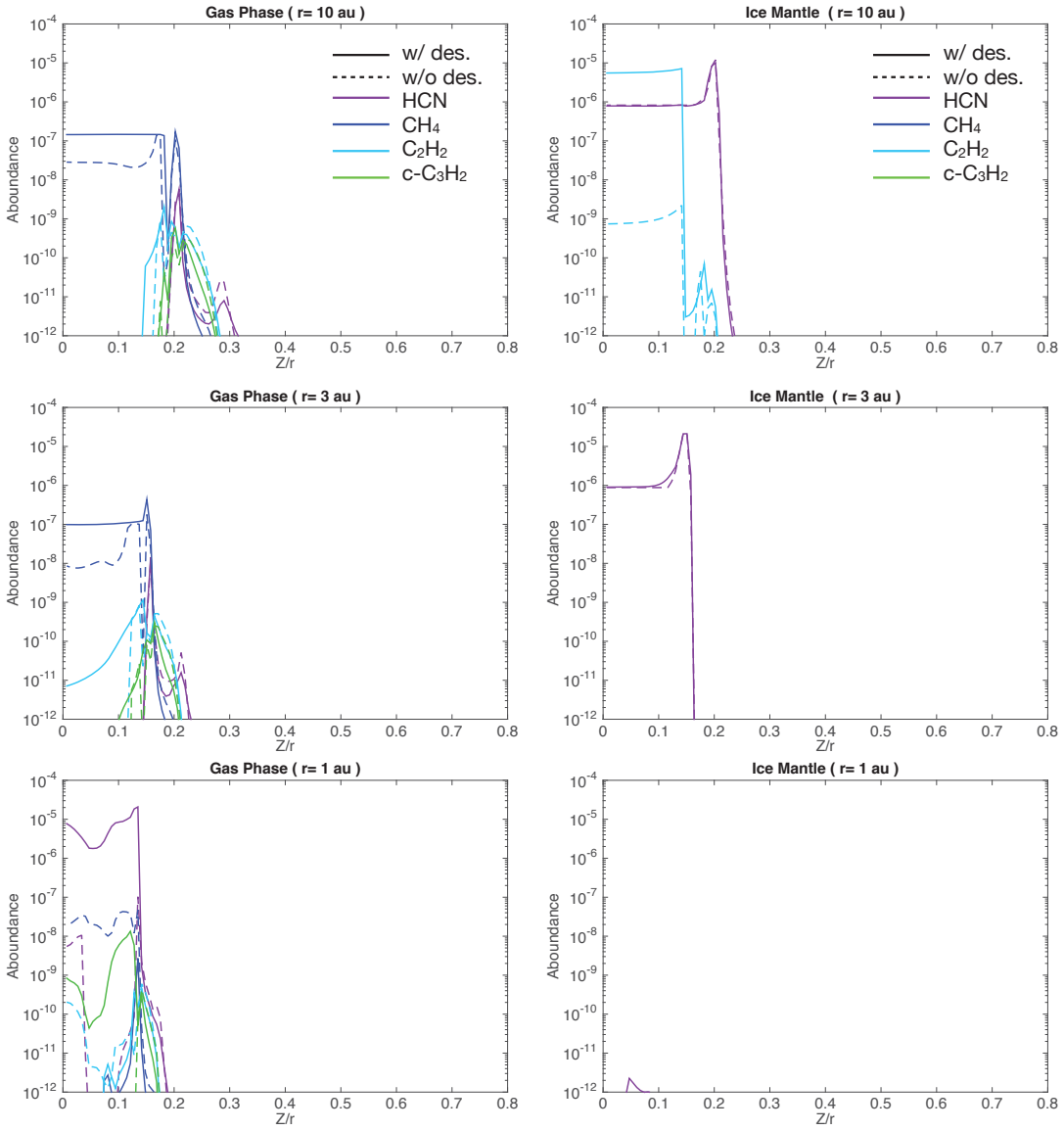

Figure 2.6: The abundances of carbon-bearing molecules as a function of height divided by radius (Z/r) at a disk radius of 10 au (top), 3 au (middle) and 1 au (bottom) for a T Tauri disk. The left and right panels show the molecular abundances in gas and ice, respectively. Solid and dashed lines represent the models with and without carbon grain destruction, respectively.

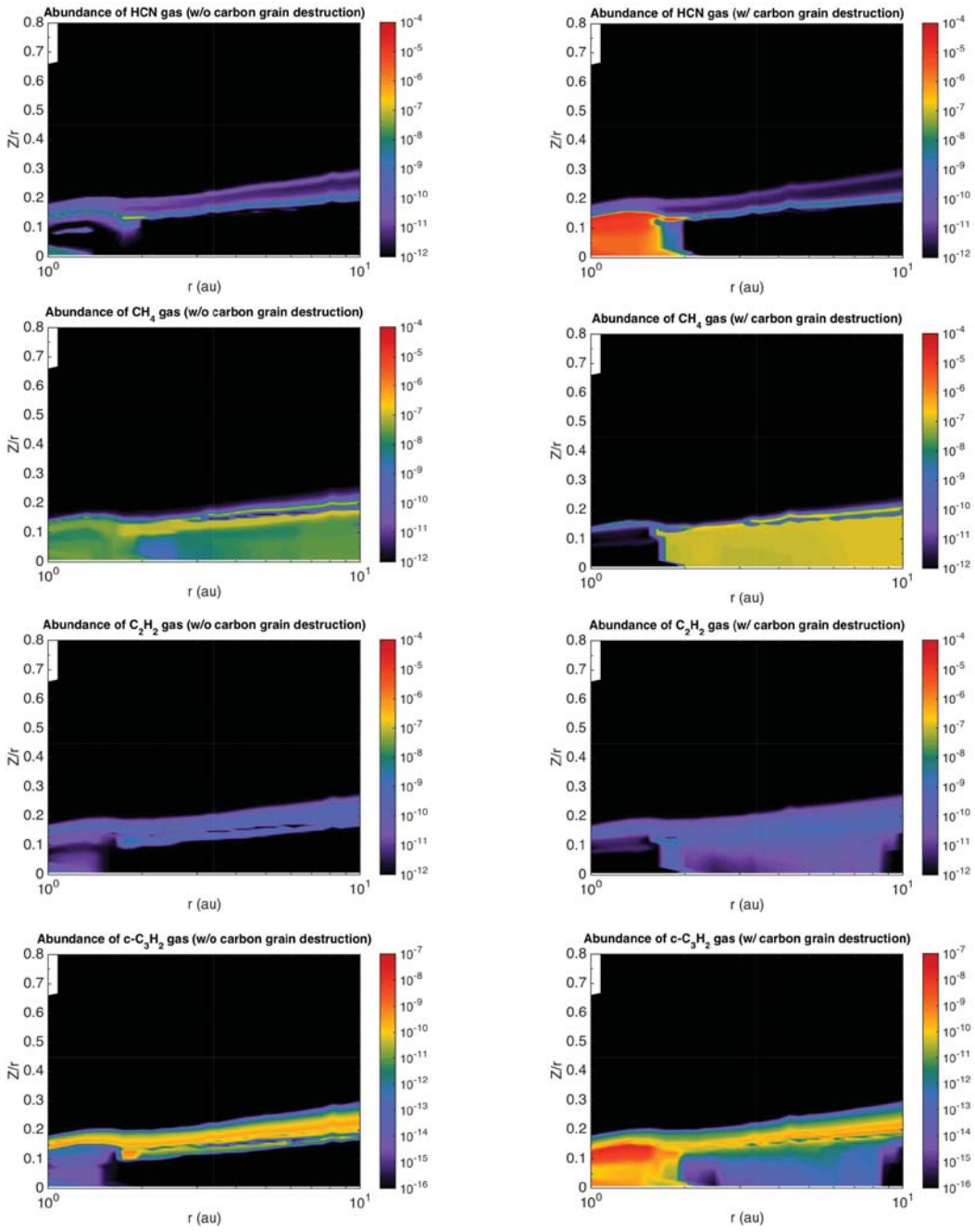

Figure 2.7: The 2-dimensional abundance distribution of gas-phase carbon-bearing molecules for the models without (left) and with (right) carbon grain destruction as a function of radius and height of the disk for a T Tauri disk. Noted that the colarbar range of c-C_3H_2 is different from the others (10^{-16} to 10^{-7}).

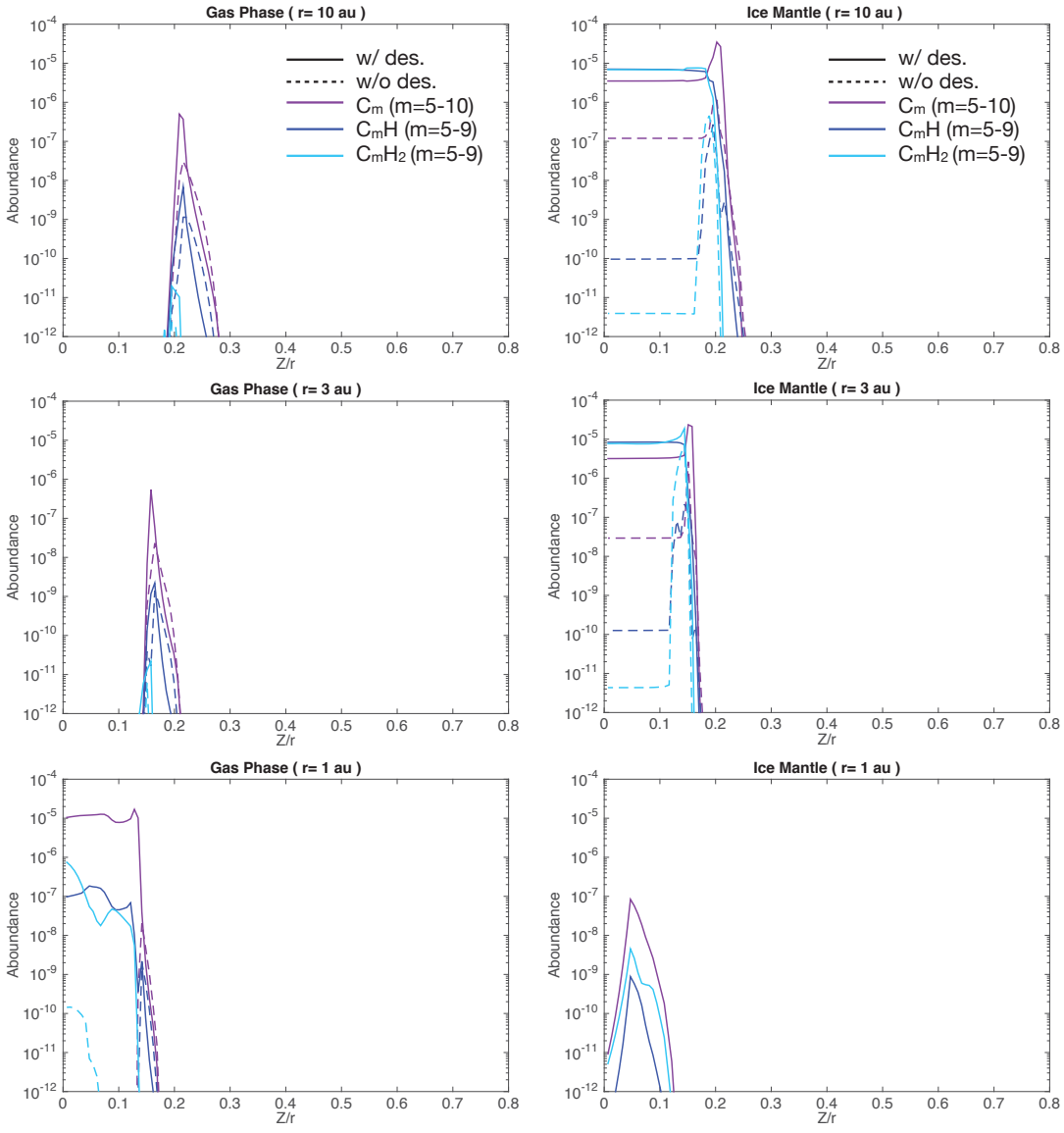

Figure 2.8: The same as Figure 2.6 but for the fractional abundance of C_m, C_mH and C_mH_2, summed over m as indicated in the figure.

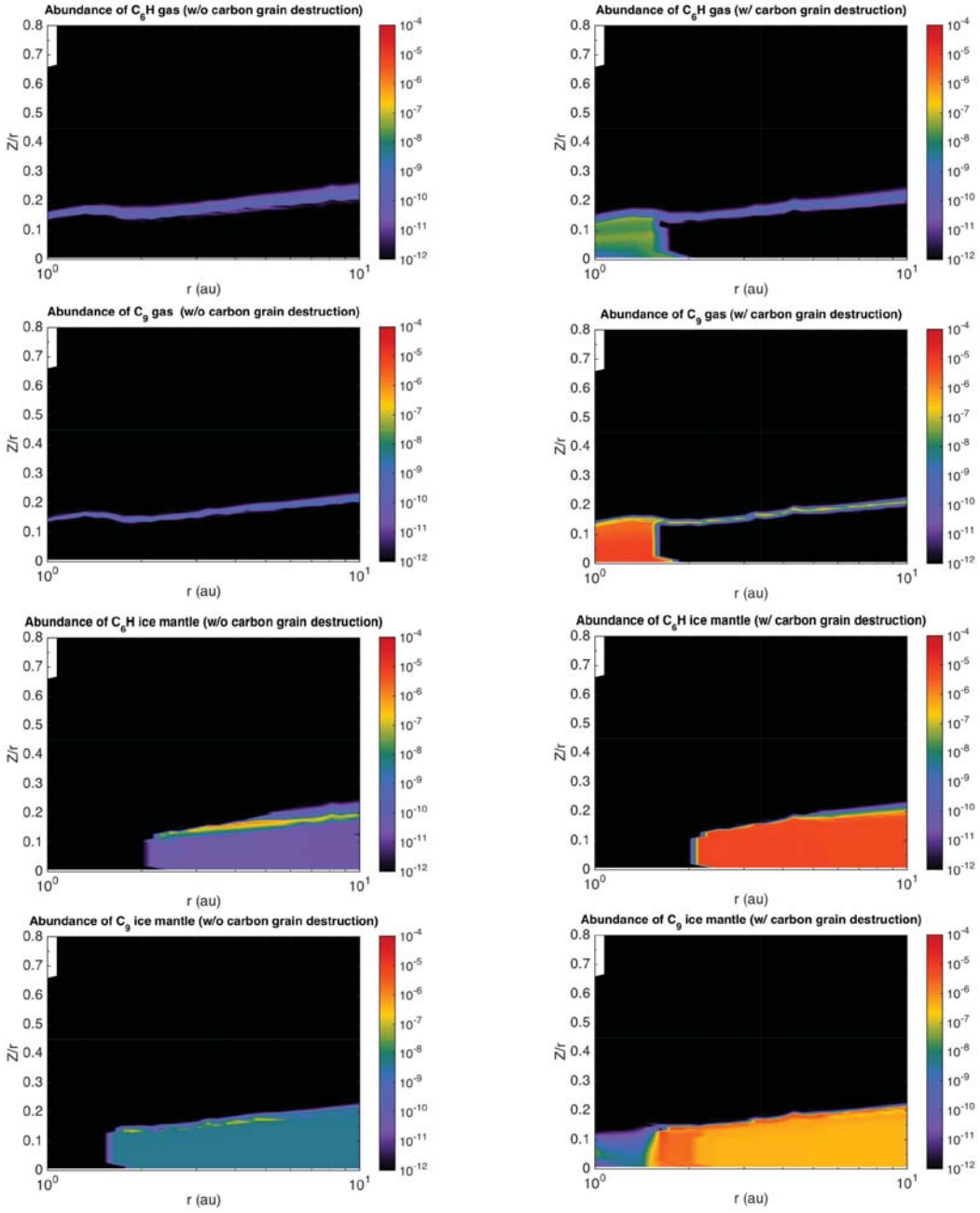

Figure 2.9: The 2-dimensional abundance distribution of C_6H and C_9 in the gas-phase and in the ice mantle for the models without (left) and with (right) carbon grain destruction as a function of radius and height of the disk for a T Tauri disk.

Figure 2.8 presents the 1-D plots of $C_m(m = 5 - 10)$, $C_mH(m = 5 - 9)$ and $C_mH_2(m = 5 - 9)$ molecules, where we sum up the abundances of the molecules for $m = 5 - 10$ or $m = 5 - 9$. Figure 2.9 shows 2-D gas and ice distributions of C_6H and C_9. We chose these two species as representative of carbon-chain molecules since they are abundant on grain surfaces (Table 2.4) and, indeed, most of the carbon-chain molecules have spatial distributions similar to these two species and to HCN. We note that we treat the carbon-chain molecules together since grain surface reactions, which may reduce the abundances of carbon-chain molecules, for example through hydrogenation, are not included here. From our calculations, we find that carbon-chain molecules with larger number of carbon atoms have larger abundances because the destruction of carbon-chain molecules by molecular ions is inefficient near the midplane of the disk where the density is high and the ionization degree is very low ($\sim 10^{-12}$). In the carbon-rich case, the gas-phase abundances increase inside the snowline near the midplane. Beyond the snowline, the ice-mantle abundances increase significantly. The binding energies of carbon chain molecules are relatively large and thus the molecules can remain on the dust grains until very close to the parent star ($\sim$ 1.5 - 3 au).

We note that the gaseous carbon-chain molecules are abundant in the molecular layers beyond their snowlines in both cases. This region corresponds to the CO gas depletion layer. Figure 2.4 and Figure 2.5 show CO gas is depleted at $Z/r \sim 0.15, r = 3 - 10$ au. Similar CO gas depletion can be seen in other disk chemical models (e.g., Walsh et al. 2010; Furuya & Aikawa 2014). Though the self and mutual shielding of CO photodissociation are not included in the model, the shielding factors are not so effective especially in the inner region of the disks (Walsh et al. 2012). In our model, the decrease is caused by photodissociation of CO due to FUV irradiation from the central star, and the subsequent formation and freeze-out of carbon-chain molecules onto grains. If the FUV field is strong enough, FUV photons dissociate CO into atomic species. Above the CO gas depletion area, the UV destruction is fast, and due to the low density, the adsorption rate on to grains is low. Therefore, any synthesized molecules are difficult to stick on the grains and will eventually convert to CO gas or, nearer the surface remain as atomic and ionized carbon. Moving deeper towards the disk midplane, where UV photons are extinguished by grains in the high density molecular layers, CO can remain in the gas-phase. A fraction of the carbon-chain molecules in ice mantle in the CO gas depleted layer is photodesorbed into gas, which produces the gaseous carbon-chain molecule rich layer seen in Figure 2.8 and Figure 2.9.

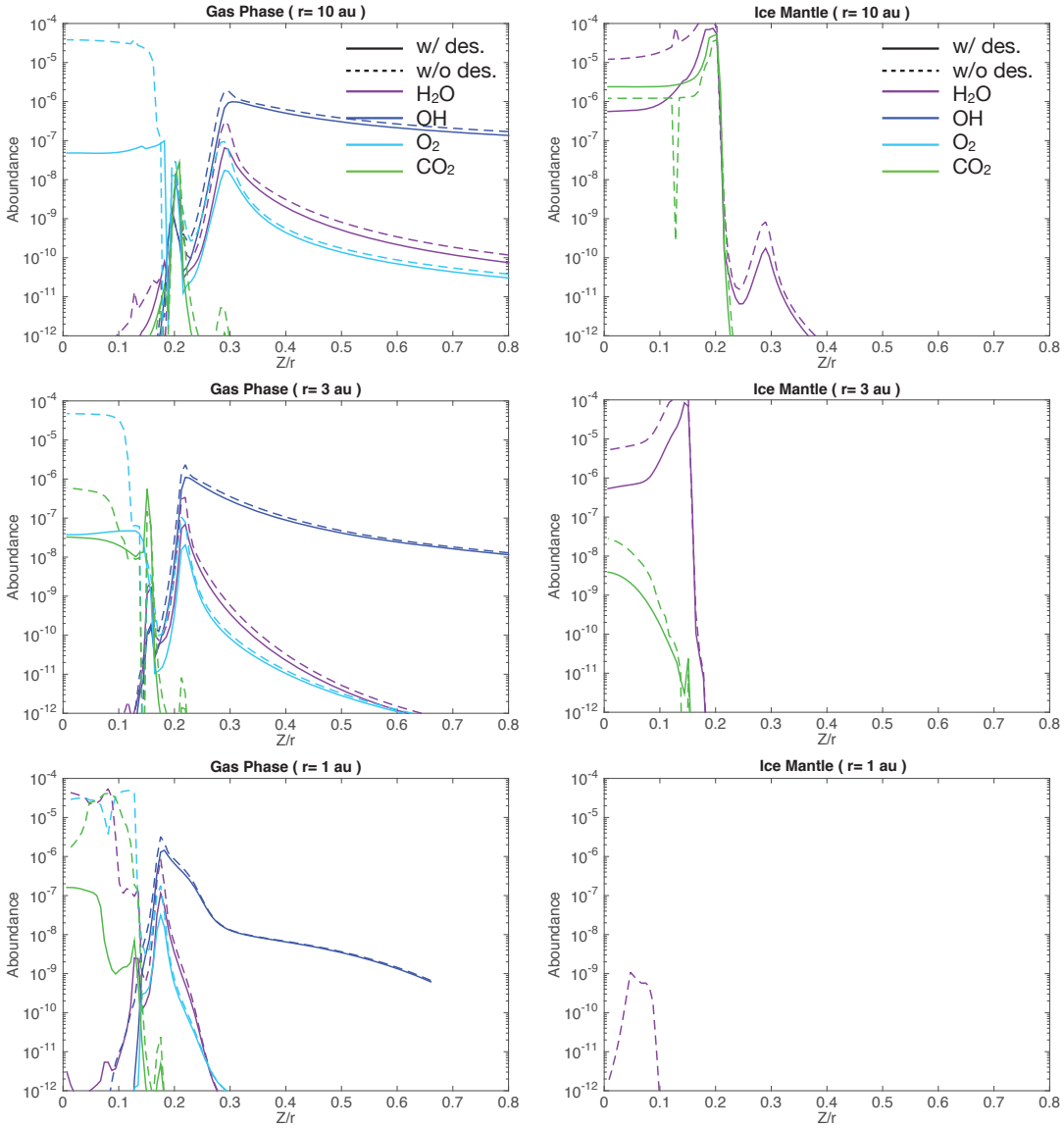

Figure 2.10: The same as Figure 2.6 but for the oxygen-bearing molecules.

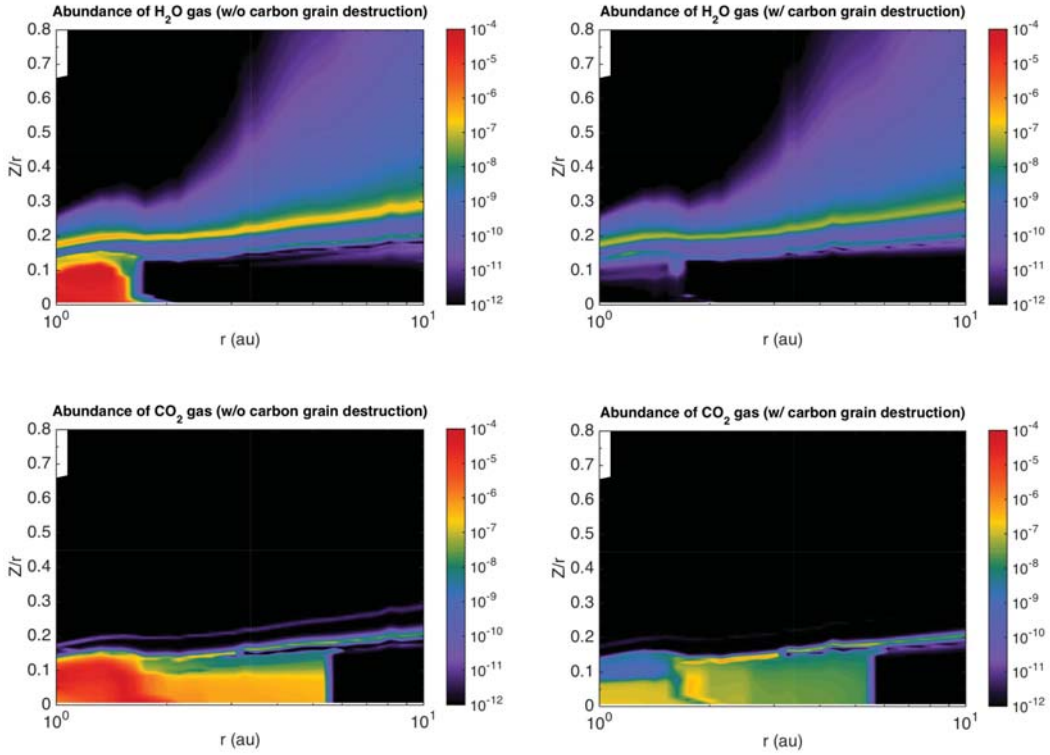

Figure 2.11: The 2-dimensional distribution of fractional abundances of oxygen-bearing molecules in the gas-phase for the models without (left) and with (right) carbon grain destruction as a function of radius and height of the disk for a T Tauri disk.

Figure 2.10 shows the 1-D plots of oxygen-bearing species (H_2O, OH, O_2 and CO_2) in the gas phase and ice mantle. Figure 2.11 shows the 2-dimensional distribution of gas-phase oxygen-bearing species, H_2O and CO_2. The results are opposite in behavior to those of carbon-bearing species. They are less abundant when carbon grains are destroyed. In Figure 2.11, in the oxygen-rich case, the volatile water abundance is enhanced inside its snowline around 2 au. In the carbon-rich case, the gas-phase water abundance is very low inside 10 au and there is no clear water ice snowline present. The distributions of CO_2 gas show clearly the snowline around 5 au in both cases. In the oxygen-rich case, the abundance peak of $\sim 10^{-4}$ appears near the midplane inside 2 au, whereas in the carbon-rich case, the peak value can only reach $\sim 10^{-6}$ close to the central star. We note that the abundance of O_2 gas can be affected by the initial abundance setting, atomic or molecular (Eistrup et al. 2016; Eistrup & Walsh 2019)

Finally, we briefly summarize in which molecules the carbon is mainly incorporated in both cases. Excluding CO gas, in the oxygen-rich case, carbon mainly resides in CO_2 gas inside the HCN snowline, and as CO_2 gas and HCN ice beyond the HCN snowline. Beyond the CO_2 snowline, carbon mainly resides in CO_2 and HCN ice. A fraction of carbon forms CH_4 gas throughout the inner disk. Meanwhile, in the carbon-rich case, carbon mainly forms HCN gas and long, gas-phase, carbon-chain molecules inside their snowlines. Beyond it, carbon mainly ends up in long, carbon-chain ice and gaseous CH_4, while inside the CO_2 snowline, some carbon is converted to gas-phase CO_2.

2.3.2 Radial distribution of solid carbon fraction

To compare the observed carbon depletion gradient in the inner solar system (Figure 2.1) with the modeled values, we calculate the carbon fraction in grains relative to the solar abundance of silicon as a function of the disk radius,

$$\text{Solid Carbon Relative to Solar Silicon} = \frac{\text{Refractory Carbon+Carbon in Ice Mantle}}{\text{Solar Abundance of Silicon}} \tag{2.14}$$

We assume that the solar abundance of silicon is 3.55×10^{-5} with respect to hydrogen nuclei (Asplund et al. 2009; Draine 2011). The value for the refractory carbon is assumed to be the difference between the solar abundance of carbon, 2.95×10^{-4} with respect to hydrogen nuclei (Draine 2011), and the gas-phase carbon abundance in the local diffuse ISM, 7.30×10^{-5} (Table 2.1). In the model with carbon grain

destruction, all the carbon has been released from the refractory material and thus there is no carbon left in this form. The released refractory carbon will be incorporated into species either in the gas-phase or in the ice mantle and the abundance of ice mantle carbon is obtained from our model calculation described in Section 2.3.1. We noted here again, the assumption of the carbon grain destruction is the extreme case that inside 10 au, all of the carbon were released out from the solid phase to the gaseous phase which is valid if we consider the grains are less than 0.1 μm or 1 μm (porous) with efficient vertical direction turbulent mixing (Lee et al. 2010; Anderson et al. 2017). One caveat here is that when considering both vertical and radial drift inside the disks, the radial transport will replenish the carbon from the outer disk and enlarge the solid carbon fraction. Thus other mechanisms to destroy solid carbon are needed to be studied. For example, flash heating events such as FU Ori outbursts to destroy the solid carbon along with the mechanisms to stop from the replenishment like the formation of giant planets (Klarmann et al. 2018). To simplify the situation, here we present the extreme cases only, which would be the minimum C/Si ratio. Here, table 2.3 shows the ratio of the carbon in the solid phase relative to the solar silicon at each disk radius.

	without destruction	with destruction	with des. and increase E_{bin} by 25%
10 au	6.25	3.62	3.69
5 au	6.25	3.39	3.60
4 au	6.28	3.39	3.57
3 au	6.28	3.38	3.56
2 au	6.25	3.31	3.38
1 au	6.25	4×10^{-6}	0.0015

Table 2.3: The ratio of the carbon in the solid phase relative to the solar silicon at different disk radius.

	without destruction	with destruction
10 au	CO_2 HCN C_5	C_6H C_6H_2 C_2H_2
5 au	HCN C_5 HCOOH	C_6H C_6H_2 C_5H
4 au	HCN HCOOH C_7	C_6H C_6H_2 C_6
3 au	HCN HCOOH CO_2	C_6H C_6H_2 C_6
2 au	HCOOH C_9 C_2S	C_9H C_9H_2 C_9
1 au	HCOOH C_9H_2 CO_2	C_9 C_9H_2 C_{10}

Table 2.4: The most abundant carbon-bearing species in the ice mantle in the midplane at different disk radii.

In the case without carbon grain destruction, the fraction does not change very

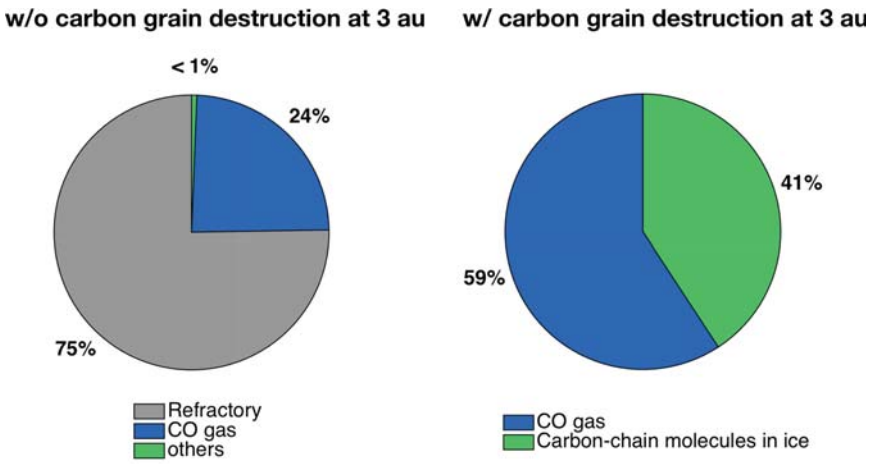

Figure 2.12: Pie chart showing the percentage of the form of carbon (gas and solid) for the models without (left) and with (right) carbon grain destruction at a disk radius of 3 au for a T Tauri disk.

much at different radii (Table 2.3), since it is imposed that the majority of the carbon is locked in refractory form. Figure 2.12 shows the percentages of the form of carbon for the models with and without carbon grain destruction at a disk radius of 3 au as an example. It shows that most of the carbon (∼75 %) is locked in refractory form in the case without carbon grain destruction. In this case the elemental abundance of oxygen is larger than that of carbon (C/O < 1) in the gas-phase, and thus most of the remaining carbon (∼24%) is stored in the form of CO gas with less than 1% in the form of larger organic species. Since the refractory carbon and CO gas do not change significantly in abundance over 1 au < r < 10 au in this model, there is almost no fractional variation in this case. On the other hand, in the case with carbon grain destruction, the fraction varies slightly at 2 au < r < 10 au and suddenly drops at r = 1 au. In this case, all the carbon in refractory form released to the gas phase reacts to form a range of species. Since the elemental abundance of carbon is larger than that of oxygen in gas-phase (C/O > 1), oxygen is mainly stored in CO in this case, capturing 1.76×10^{-4} (see Table 2.1), the corresponding amount of carbon, that is, $1.76 \times 10^{-4}/2.95 \times 10^{-4} \simeq 60$ % of the total carbon as CO gas (Figure 2.12). The remaining carbon is mainly in the form of carbon-chain molecules in the ice mantle at $r \geq 2$au, as is shown in Sect. 2.3.1 (see e.g., Figure 2.9 and Figure 2.10). Table 2.4 shows the most abundant carbon-bearing species in the ice mantle in the disk midplane at different radii. The carbon-bearing molecules in the ice mantle evaporate into the gas phase inside their snowlines and the locations of the snowlines depend on their binding energies (see Table 2.2). Therefore, the fraction of carbon in the solid-

phase changes across these snowlines of carbon-bearing species. Since the most abundant carbon-bearing molecules in the ice mantle are carbon-chain molecules (see Table 2.4) whose snowlines are located around the disk radii of $\sim$ 2 au (see Table 2.2), the solid carbon fraction does not decrease until r < 2 au. Noted here, as we mentioned before, there are some uncertainties in the abundances of carbon-chain molecules in the ice mantle because grain surface reactions are not included in our calculation. Once grain surface reactions are considered, hydrogenation reactions on the surface may lead to the formation of alkanes.

While the model results reproduce qualitatively the trend of carbon depletion observed in the solar system, the comparison between our result (Table 2.3) and the solar system data (Figure 2.1) shows some quantitative discrepancies. There is a relatively high carbon fraction in the asteroid belt (a few to an order of magnitude larger) and too much depletion at 1 au ($\sim$ three orders of magnitudes smaller) compared to the observation values. This is possibly caused by the omission of, for example, grain surface reactions and/or turbulent mixing, which we have not yet taken into account in our chemical model and will alter the chemical structure of the disk and the partitioning of carbon between solid and gaseous forms. With grain surface reactions, a higher carbon fraction in the ice mantle might be produced by large carbon-bearing molecules formed from species stuck on the grain surface that react with other species (e.g., Hasegawa et al. 1992; Hasegawa & Herbst 1993; Garrod & Herbst 2006; Garrod et al. 2008; Walsh et al. 2014; see Appendix 3.5.2 for the detail discussion of the grain surface reaction). On the other hand, turbulent mixing can bring the dust grains from the midplane up to the warm surface layer where the ice mantle can be photodissociated or thermally desorbed. This leads to a decrease in the solid carbon fraction, perhaps to a level consistent with that in the asteroid belt (e.g., Furuya et al. 2013; Furuya & Aikawa 2014; Semenov & Wiebe 2011). We note that the timescale of vertical mixing is $\tau_{mix} \sim 6 \times 10^4 (r/10AU)(\alpha/0.01)^{-1}$ yr, where α represents the parameter for vertical mixing, similar to the α parameter in the viscous disk (e.g., Furuya et al. 2013). Figure 2.13 show the abundance evolution of the icy species which are abundant or have much difference between two cases at midplane of 3 au in the case of with carbon grain destruction. We compare the timescale which chemical abundances become saturated with the turbulent mixing timescale. In the case of C_6H and C_6H_2 which are the abundant icy species at 3 au listed in Table 2.4, the abundances become saturated around 10^5 years and if the vertical mixing α is 0.01, the turbulent mixing timescale is around 2×10^4 years. Therefore, when α is 0.01, turbulent at vertical direction is possible to bring up the icy grains up to the surface

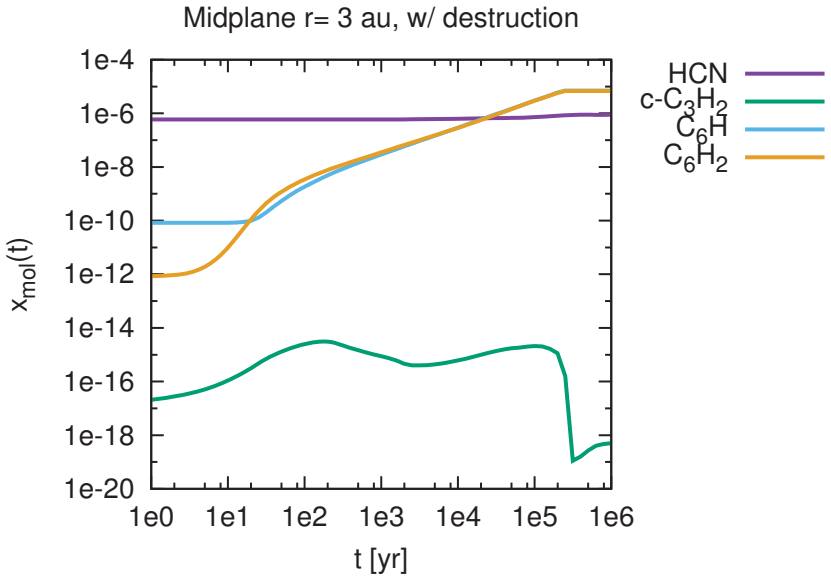

Figure 2.13: The abundance evolution of the icy species, HCN, c-C_3H_2, C_6H and C_6H_2, which have much difference between two cases or are abundant at midplane of 3 au in the case of with carbon grain destruction.

layer before they are saturated and destroy the icy component by the photochemistry which is with even shorter timescale than the turbulent mixing (see Figure 2 of Furuya et al. 2013). In addition, uncertainties in the binding energies of molecules on grains will affect the solid carbon fraction in grains. Desorption rates depend exponentially on binding energies (see Equation 2.18). However, due to the lack of appropriate data for many binding energies, the values are still very uncertain. We therefore enlarged the value of binding energies by 25% to investigate how the solid carbon fraction changes as binding energies change. We found that the value at 1 au becomes comparable with the observed value on the Earth when binding energies increase about 25% (see Table 2.3). We note that the increased binding energies of carbon-chain molecules are close to the data in complied for the UMIST Database for Astrochemistry [1] (McElroy et al. 2013). The other possibility to increase the carbon at 1 AU to the level we observed nowadays, is the supplement from the small bodies. The same issue had been discussed in Lee et al. (2010). They suggested that the supplement of carbon might come with the small bodies with the same amount of carbon in the carbonaceous chondrites. This might explain the origin of Earth's oceans as well, since the possession of water is difficult for the location of 1 AU.

[1] http://www.udfa.net/

2.3.3 Prediction for ALMA observations

Our results in Section 2.3.1 suggest that if carbon grains are destroyed in the inner region of protoplanetary disks, it will affect the molecular abundance profiles, a process which could be tested by observing the molecular line emission. In this subsection, we perform ray tracing calculations, using the molecular abundance profiles obtained from our model calculation and determine whether or not carbon grain destruction in the inner disk can be tested observationally.

While molecular lines have been observed towards protoplanetary disks at infrared and (sub)millimeter wavelengths, we choose lines which are observable with ALMA. Since, as we have seen in Section 2.3.1, significant differences in molecular abundances between the models with and without carbon grain destruction appear only near the disk midplane where CO is dominant and not photodissociated. Therefore, (sub)millimeter lines are more suitable to trace potential differences because infrared lines are optically thick and trace only the disk surface layer. In addition, ALMA enables us to spatially resolve the inner region of the disk, which allows us to see the difference between the models more clearly. Among the molecular lines observable at (sub)millimeter wavelengths, we choose the HCN lines because (1) the HCN abundance distribution is very much affected by the carbon grain destruction (see Section 2.3.1), and (2) they are known to be strong towards protoplanetary disks (e.g., Dutrey et al. 1997; Qi et al. 2008; Öberg et al. 2010; Öberg et al. 2011; Chapillon et al. 2012; Huang et al. 2017). Three HCN isotopologues, DCN, $H^{13}CN$ and $HC^{15}N$, have been detected towards protoplanetary disks (e.g., Qi et al. 2008; Huang et al. 2017; Guzmán et al. 2015; Guzmán et al. 2017). We concentrate here on $H^{13}CN$ because the DCN/HCN ratio is known to be sensitive to the temperature profile (e.g., Aikawa & Herbst 2001; Willacy 2007; Cleeves et al. 2016; Aikawa et al. 2018), while $H^{13}CN$ is less affected (e.g., Woods & Willacy 2009). Meanwhile, $H^{13}CN$ lines are stronger than $HC^{15}N$ lines (Guzmán et al. 2017) and it is easier to analyze its spatial distribution. The combination of HCN and its isotopologue lines is useful to test the carbon grain destruction model since HCN lines are optically thick and trace mostly surface layer of the disk where CO is photodissociated and the carbon grain destruction does not affect molecular abundances significantly. The HCN isotopologue lines are less optically thick and trace the lower layer of the disk where CO is not photodissociated and the effect of carbon grain destruction is significant.

Figure 2.14 displays the profiles of the HCN and $H^{13}CN$ J=4-3 lines at 354.5 and 345.3 GHz respectively, with the spectral resolution of 0.4 km/s^{-1}, for the T-Tauri disk, calculated by performing ray tracing calculations (see Section 2.3.2) using the

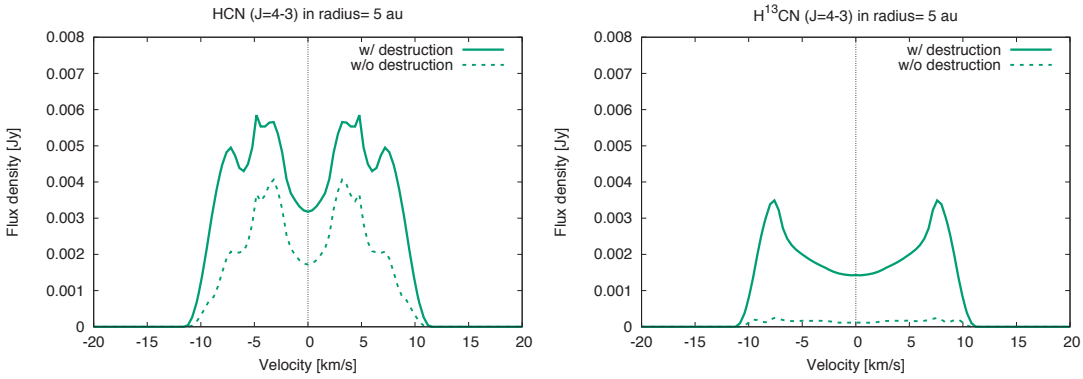

Figure 2.14: The line profiles of the HCN (left) and $H^{13}CN$ (right) J = 4 - 3 lines within r < 5 au of T-Tauri disk. Solid and dashed lines represent the models with and without carbon grain destruction, respectively.

obtained physical structure (Figure 2.2) and the HCN abundance profile (Figure 2.7). The HCN/$H^{13}CN$ abundance ratio is simply assumed to be the typical interstellar value of 70 (Qi et al. 2011). According to Woods & Willacy (2009), it could be larger by a factor of ≤ 2 in the disk surface where the effect of self-shielding is significant and different CO isotopologues are selectively photo-dissociated. But the assumption is reasonable in the region closer to the disk midplane. We assume the distance to the T-Tauri disk is 70 pc and its inclination angle is 30 degrees. The left- and right-hand sides of Figure 2.14 show the line profiles of HCN and $H^{13}CN$, respectively. The line profiles are calculated only inside a radius of 5 au since the significant differences between two models appears mainly inside 2 au (Figure 2.7). Solid and dashed lines represent models with and without grain destruction, respectively. Figure 2.14 indicates that the line emission of $H^{13}CN$ shows more obvious differences between the two cases. However, the peak flux density is less than 1 mJy for the $H^{13}CN$ line for the model without the carbon grain destruction, and it is too weak to use it for testing the carbon grain destruction model even with ALMA.

For this reason, we have also modeled a Herbig Ae disk since the radiation from the central source is stronger and the hot region is larger (Figure 2.2). Thus, the carbon grain destruction region spreads to larger radii and the observational test will be easier. Figure 2.15 shows the distribution of HCN in the Herbig Ae disk as a function of radius up to 50 au and the disk height divided by the radius (Z/r). Gas-phase reactions produce HCN efficiently only in the very hot region inside a disk radius of r $\leq$ 5 au for the model without carbon grain destruction, while gas-phase HCN can be very abundant in the whole region inside the HCN snowline at $\sim$ 20 au for the model with carbon grain destruction. Therefore, a dramatic change appears appears at radii

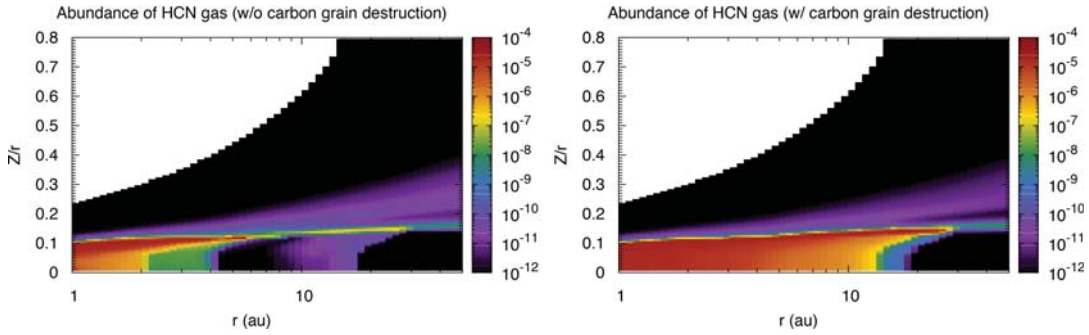

Figure 2.15: The abundance distributions of HCN in a protoplanetary disk around a Herbig Ae star for models without (left-hand-side) and with (right-hand-side) carbon grain destruction. A dramatic change appears around r ∼ 2-30 au between the models.

of 2 - 30 au between two models. In contrast, the significant differences in T-Tauri disk appear only very close to the central star (inside 2 au) and the flux density is too low to be observed.

Figure 2.16 is the zeroth moment map, that is, the integrated intensity map of the HCN and $H^{13}CN$ lines, calculated as

$$M_0(x, y) = \int I(x, y, v)dv \tag{2.15}$$

where $I(x, y, v)$ is the intensity as a function of position, (x, y), and velocity, v, given by Equation 2.10.

The physical structure (Figure 2.2) and the HCN abundance profile (Figure 2.15) of the Herbig Ae disk are used. We assume that the distance to the disk is 140 pc and its inclination angle is 30 degrees. The $H^{13}CN$ line intensity map shows the difference more clearly than the HCN line. This is because the $H^{13}CN$ line traces a relatively lower layer of the disk due to relatively lower optical depth than the HCN line. Figure 2.17 shows the optical depth of the HCN and $H^{13}CN$ lines along the vertical direction of the disk for the models without and with carbon grain destruction. The HCN line becomes optically thick up to a disk radius of ∼ 30 au even for the model without the carbon grain destruction, that is, the HCN line only traces the disk surface where the difference in the HCN abundance is not significant between the models (Section 2.3.1). On the other hand, the isotopologue $H^{13}CN$ line is optically less thick and can trace the HCN abundance difference near the midplane at a disk radii of r < 30 au. Therefore, the difference in the emitting regions of intensity map between the HCN and $H^{13}CN$ lines is a good tracer for testing the carbon grain destruction.

Even in those cases for which spatially resolved observations are difficult, the profiles of the HCN and $H^{13}CN$ lines can be a good tracer as well. Figure 2.18 shows the

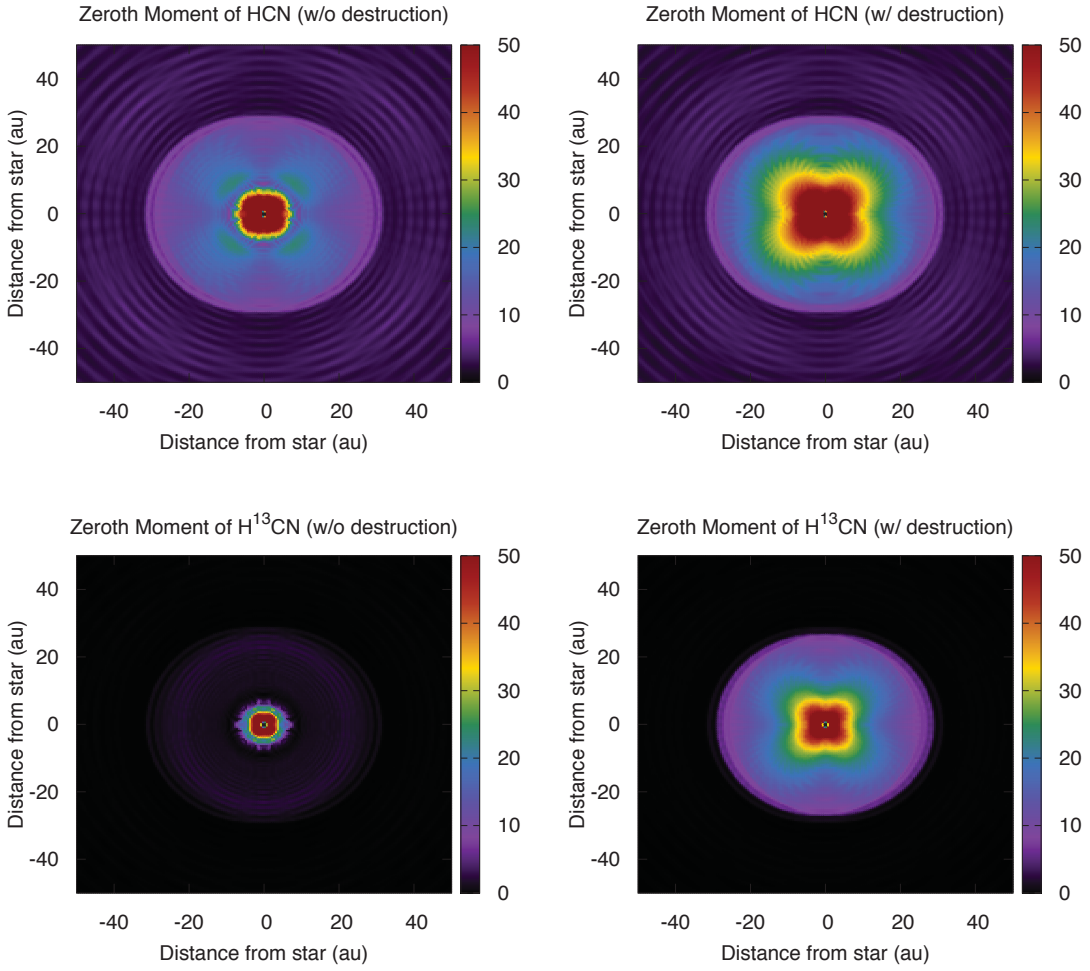

Figure 2.16: The zeroth moment maps of the HCN (top) and $H^{13}CN$ (bottom) J= 4 -3 lines for the models without (left-hand-side) and with (right-hand-side) the carbon grain destruction for the Herbig Ae disk. The unit of the color map is Jy arcsec^{-2}km s^{-1}.

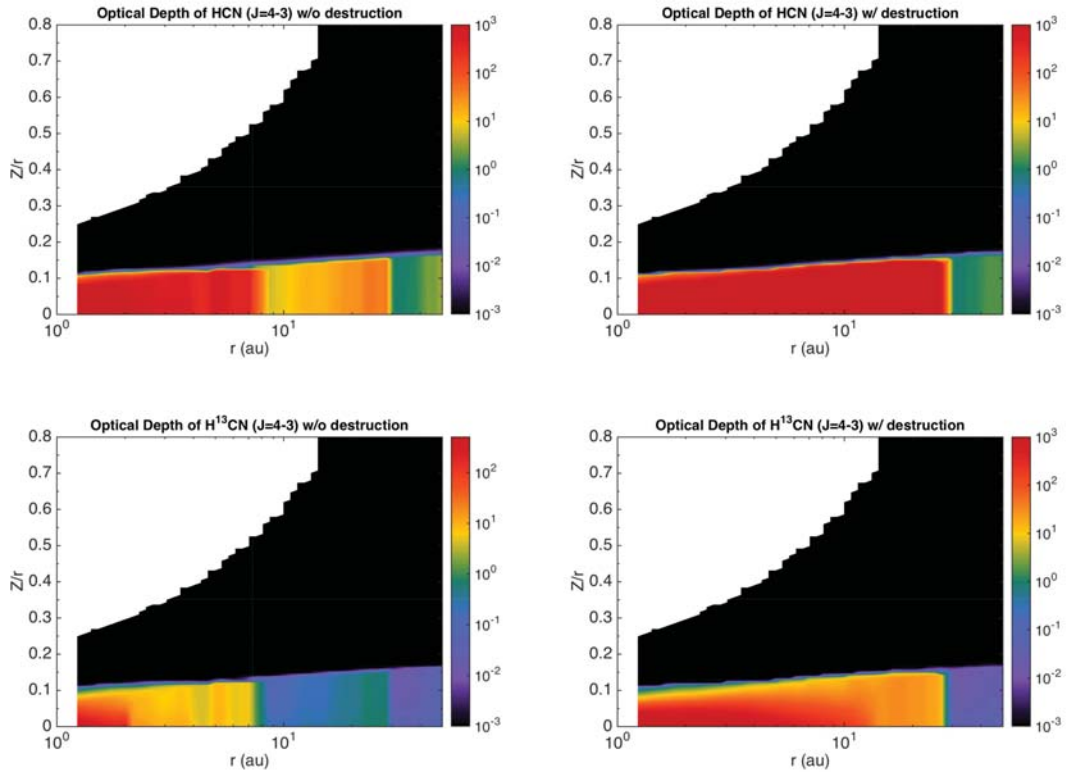

Figure 2.17: The optical depth of the HCN (top) and $H^{13}CN$ (bottom) lines for the models without (left-hand-side) and with (right-hand-side) the carbon grain destruction.

line profiles of the HCN line (left-hand-side) and the $H^{13}CN$ line (right-hand-side). In both profiles, the solid line represents the model with carbon grain destruction and the dotted line is the model without. Like the T-Tauri disk model (Figure 2.14), the line emission of $H^{13}CN$ shows more substantial differences between the two models. The differences in the $H^{13}CN$ line range from high velocity (~10 km/s, tracing the inner region) to low velocity (tracing the outer region). In contrast, the differences in HCN emission mainly exist at velocity of -5 to + 5 km/s.

Figure 2.19 is the normalized cumulative line flux as functions of disk radius (left-hand-side) and the velocity (right-hand-side). The former is calculated from the disk center to the disk radius of 25 au and the latter is calculated over the range $0 < v < 20$ km/s. Each cumulative flux is normalized using the following equations,

$$F_{cum}(r) = \frac{\int_0^r 2\pi r' dr' \int_{-a}^{+a} I(r', v) dv}{\int_0^b 2\pi r' dr' \int_{-a}^{+a} I(r', v) dv},$$
$$F_{cum}(v) = \frac{\int_0^v dv' \int_0^b I(r, v') 2\pi r dr}{\int_0^{+a} dv' \int_0^b I(r, v') 2\pi r dr}, \tag{2.16}$$

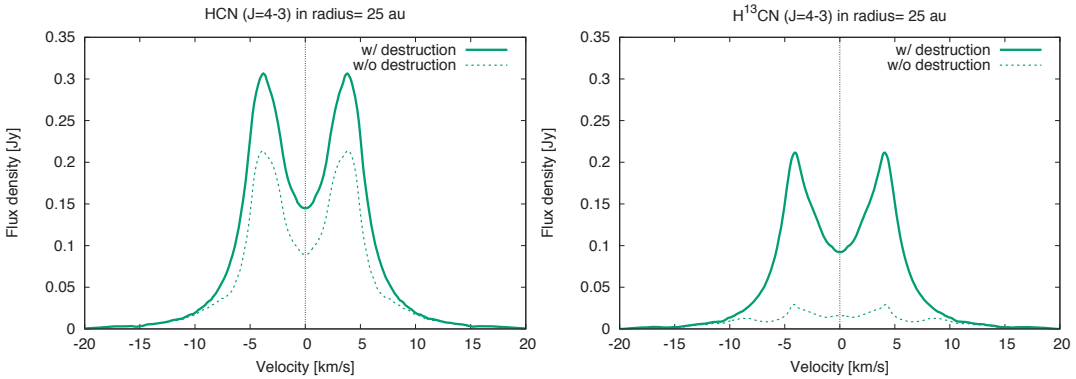

Figure 2.18: The line profiles of the HCN (left) and $H^{13}CN$ (right) J = 4 - 3 lines within r < 25 au of Herbig Ae disk. Solid and dashed lines represent the models with and without carbon grain destruction, respectively.

where a is defined as 20 km s^{-1} and b as 25 au. The blue and green lines are models with and without carbon grain destruction, respectively, with HCN represented by the solid lines and $H^{13}CN$ the dashed lines. Comparing the results in the same color, the differences between two models can be easily distinguished by the ratio of HCN and $H^{13}CN$. In left-hand-side figure, the green dashed line reaches $\sim$ 60 % of the cumulative flux inside 5 au and the green solid line reaches the same level inside $\sim$ 15 au. This can be explained from the intensity map. For the model without carbon grain destruction, the intensity of the $H^{13}CN$ line is strong only in very compact region ($r < 5$ au) as shown in Figure 2.16. Meanwhile, the HCN line is strong out to $r \sim 30$ au and thus the normalized cumulative flux increases smoothly with radius. On the other hand, for the model with carbon grain destruction, both HCN and $H^{13}CN$ lines are strong out to $r \sim 30$ au and the cumulative fluxes increase smoothly, with no significant difference between them, so that differences between the two models can be tested by the cumulative flux as a function of radius if it can be spatially resolved. Even in the case for which the emission is not spatially resolved, we can see these differences in the line profiles, that is, cumulative flux as a function of velocity (e.g., Zhang et al. 2017). The green lines in Figure 2.19 (right-hand-side) show the differences between two models clearly. Comparing the normalized cumulative flux with the line profiles (Figure 2.18), the shape and the distribution of the model without carbon grain destruction are very different from HCN and $H^{13}CN$. However, the line shape and the distribution in the model with carbon grain destruction are very similar for both HCN and $H^{13}CN$. Both figures show significant differences between the HCN and $H^{13}CN$ lines for the model without the carbon grain destruction, while the difference is not large for the model with carbon grain destruction. Therefore, the

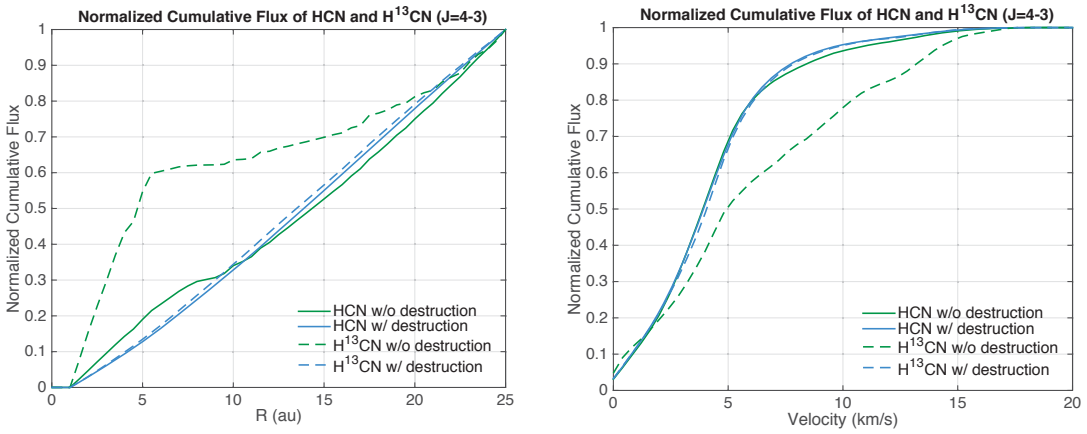

Figure 2.19: The normalized cumulative line flux of the HCN (solid lines) and $H^{13}CN$ (dashed lines) J = 4 - 3 lines as a function of the disk radius (left-hand-side) and the velocity (right-hand-side) for the models without (green lines) and with (blue lines) carbon grain destruction. Under the assumption of a disk in Keplerian rotation, the velocity profiles reflect the line emitting regions.

differences between two models can be easily distinguished by the ratio of the HCN and $H^{13}CN$ line.

HCN and $H^{13}CN$ lines have been detected toward some Herbig Ae stars by ALMA (e.g., Guzmán et al. 2015, Huang et al. 2017). Guzmán et al. (2015) have reported the observations of the HCN J = 4 - 3 and $H^{13}CN$ J = 3 - 2 lines with relatively low spatial resolution of > 0.7 ″. Mapping the inner region of the disk (around the disk radius of 10 - 20 au), taking advantage of ALMA's high spatial resolution and high sensitivity, would be useful to diagnose carbon grain destruction in the inner disk.

Because the abundance distribution of molecules has some uncertainty depending on the chemical model, here we suggest c-C_3H_2 $6_{1,6}$-$5_{0,5}$ (217.882 GHz) as the other target line. This line has been detected in a Herbig Ae disk (Qi et al. 2013). The line is blended with the c-C_3H_2 $6_{0,6}$-$5_{1,5}$ line, but we treat only the C_3H_2 $6_{1,6}$-$5_{0,5}$ since it is slightly stronger. We note that other transition lines of c-C_3H_2 have been detected toward T Tauri disks (Bergin et al. 2016). Figure 2.20 shows that the distribution of c-C_3H_2 in the Herbig Ae disk as a function of radius up to 50 au and the disk height divided by the radius (Z/r), which indicates the significant difference appears at r < 30 au between the models, similar to the case of HCN. The difference in the abundance distribution results in the clear differences in both the intensity map (Figure 2.21) and the line profile (Figure 2.22). To sum up briefly, we suggest HCN, $H^{13}CN$ and c-C_3H_2 as possible tracers of testing the carbon grain destruction effect in protoplanetary disks.

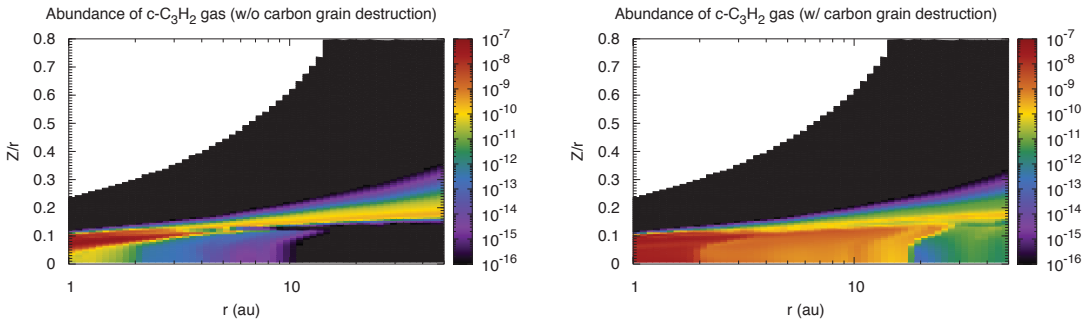

Figure 2.20: The abundance distributions of c-C_3H_2 in a protoplanetary disk around a Herbig Ae star for models without (left-hand-side) and with (right-hand-side) carbon grain destruction.

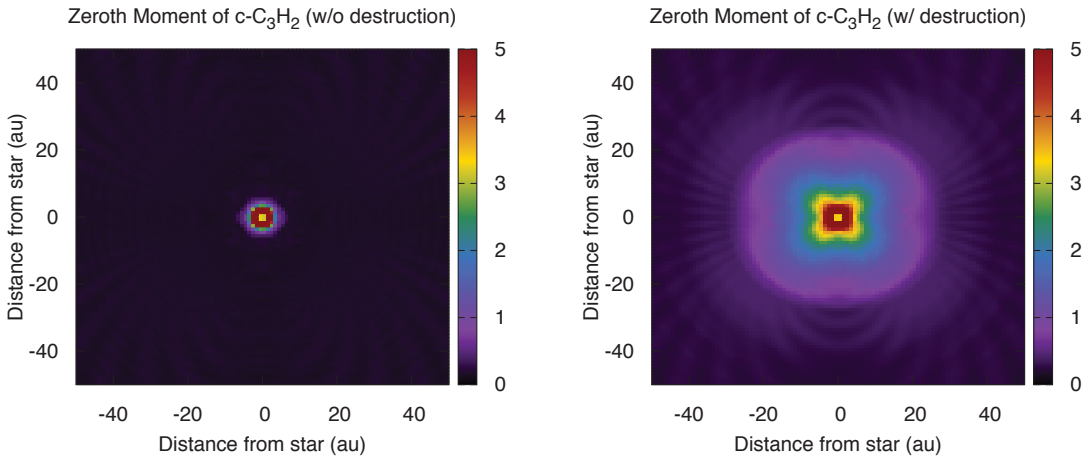

Figure 2.21: The same as Figure 2.15 but for the c-C_3H_2 $6_{1,6}$-$5_{0,5}$ line for the Herbig Ae disk.

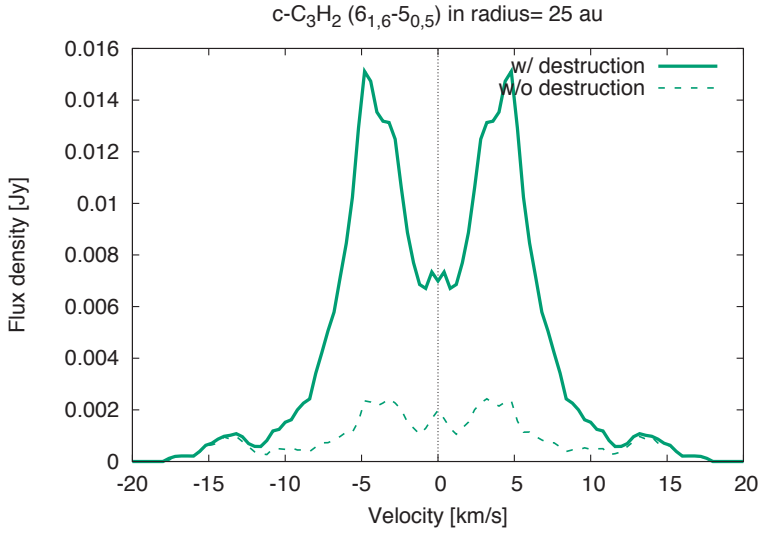

Figure 2.22: The same as Figure 2.17 but for the c-C_3H_2 $6_{1,6}$-$5_{0,5}$ line within r < 25 au.

2.4 Summary

In this work, we focus on two issues: (1) The carbon depletion gradient in the inner solar system, and (2) searching for observational evidence of carbon grain destruction in the disks of T-Tauri and Herbig Ae stars. We conclude that the carbon grain destruction affects the abundances and distribution of various molecules in the protoplanetary disk, showing significant differences especially near the midplane in the inner region of the disk, where CO gas is abundant and is not photodissociated. For example, the gas-phase HCN abundance shows 8 orders of magnitudes difference near the midplane inside the radius of 2 au in the T-Tauri disk.

The distribution of molecules is determined by their volatility such that volatile species can evaporate into gas even in the outer region of the disk. Those molecules which remain in ice mantles can influence the composition of subsequently forming planets. Therefore, we present the location of the snowlines and calculate the solid carbon fraction relative to the solar abundance of carbon as a function of the radius in the inner region of a protoplanetary disk. Although the carbon depletion gradient is reproduced in the model with carbon grain destruction, the resulting solid carbon fractions show a quantitative discrepancy from those in the solar system. The solid carbon fractions in the asteroid belt are about an order of magnitude larger than the measured value of the meteorites. Meanwhile, the value at 1 au is 3 orders of magnitude smaller than the measured value. Including grain surface reactions in the model may help to better reproduce the carbon depletion gradients. For example, grain surface reactions are expected to make more complex, less volatile, organic molecules in the disk and could further enlarge the solid carbon fraction at 1 au. We also examined the effect of carbon grain destruction on predictions for ALMA observations. We find that lines in T Tauri are too weak to probe carbon grain destruction but that ALMA can probe this effect through the line ratio of HCN/H^{13}CN as well as c-C_3H_2 in Herbig Ae disks.

2.5 Appendix

2.5.1 The calculation of adsorption and desorption rates

The adsorption(freeze-out) rate of species i onto grain surface, k_i^a [s^{-1}], is written as (Hasegawa et al. 1992)

$$k_i^a = \alpha \sigma_d < v_i^{th} > n_d, \tag{2.17}$$

where α is the sticking coefficient and we set it as 0.4 for all species (Veeraghattam et al. 2014), $\sigma_d = \pi r_d^2$ is the geometrical cross section of a dust grain, r_d is the dust grain radius and n_d is the number density of dust grains. We fix the number density ratio of dust grains to hydrogen nuclei ($d_g = n_d/n_H$) times the geometrical cross section of grain (σ_d), as $\pi < d_g r_d^2 >= 6.9 \times 10^{-22}$ cm^2, according to Rawlings et al. (1992), which is consistent with a gas-to-dust mass ratio of 100. $< v_i^{th} >= (k_B T_g/m_i)^{1/2}$ represents the thermal velocity of species i, where k_B is the Boltzmann's constant, T_g is the temperature of gas and m_i is the mass of species i.

The thermal desorption rate, k_i^d [s^{-1}], with which species i evaporate from the dust grain surface, is represented as (Hasegawa et al. 1992)

$$k_i^d = \nu_0(i) \exp(\frac{-E_d(i)}{T_d}), \tag{2.18}$$

where $E_d(i)$ is the binding energy of species i to the dust grain surface in units of Kelvin, T_d is the dust temperature and ν_0 is the vibrational frequency of each adsorbed species in its potential well (Hasegawa et al. 1992).

$$\nu_0(i) = \sqrt{\frac{2 n_s k_B E_d(i)}{\pi^2 m_i}}, \tag{2.19}$$

where n_s represents the surface density of sites, $n_s = 1.5 \times 10^{15}$ cm^{-2}, and m_i is the mass of the adsorbed species i.

For cosmic-ray induced thermal desorption, we assume that dust grains with a radius of 0.1 μm are heated by the impact of relativistic Fe nuclei with energy from 20 to 70 MeV $nucleon^{-1}$ and deposit an energy of 0.4 MeV on average into each dust grain (Leger et al. 1985; Hasegawa & Herbst 1993). Assuming that the majority of molecules will desorb around 70 K, the cosmic ray induced thermal desorption rate, k_i^{crd}, is expressed as

$$k_i^{crd} \approx f(70K) k_i^d(70K) \frac{\zeta_{CR}}{1.36 \times 10^{-17} s^{-1}}, \tag{2.20}$$

where ζ_{CR} is the cosmic ray ionization rate of H_2 scaled by the interstellar value used in the UMIST database, 1.36×10^{-17} s^{-1}. k_i^d(70 K) is the thermal desorption rate of species i at dust temperature of 70 K. $f(70K)$ is the fraction of time that dust grain spends above 70 K and it is roughly calculated by the ratio of the desorption cooling time ($\sim 10^{-5}$ s) to the total interval time for the temperature of dust grain to become 70 K (3.16×10^{13} s, Leger et al. 1985). Therefore, f(70 K) $\approx 3.16 \times 10^{-19}$. Although X-rays can penetrate the disk and induce desorption as well, we do not include it in this chemical network because of the remaining uncertainty in the desorption rate.

Photodesorption is independent of the surface binding energy. The photodesorption rate adopted is based on the experiments of Westley et al. (1995) and Öberg et al. (2007). Their results show that each photon absorbed by a dust grain will release a particular number of molecules into the gas phase and it is related to the fractional abundance on the dust grain surface. The photodesorption rate, k_i^{ph}, is expressed by the following equation (Willacy & Langer 2000; Willacy 2007)

$$k_i^{ph} = F_{UV} Y_{UV}^i \sigma_d \frac{n_d}{n_{act}}, \tag{2.21}$$

where F_{UV} represents the UV radiative field at each position in the disk in units of photon $cm^{-2}s^{-1}$. Y_{UV}^i is the photodesorption yield determined from the experiments in the unit of molecules $photon^{-1}$, and we adopt the value of 3.0×10^{-3}, which is determined by experiments of pure water ice (Westley et al. 1995) and pure CO ice (Öberg et al. 2007). n_{act}=$4\pi r_d^2 n_d n_s N_{LAY}$ represents the number of active surface sites in the ice mantle per unit volume and N_{LAY} is the number of surface layers considered as active, assumed to be two.

Chapter 3

The Effect of Mantle Reactions on Formation of Complex Organic Molecules

3.1 Introduction

Comets are thought to be the objects preserving the pristine materials from the proto-Solar nebula. They can be the link to understand the environment and the processes during the formation of the Solar system. The observation towards comet by Rosetta mission gives us many first-time discoveries (Bieler et al. 2015; Goesmann et al. 2015; Capaccioni et al. 2015), opening the new pages of cometary science. Rosetta is an ESA mission, launched in 2004 and has it first rendezvous with comet 67P/C-G on August 4^{th} 2014. From that on, Rosetta starts a series of in situ measurements towards the comet until the end of September 2016.

Previous information of cometary nucleus is mainly derived by composition in the cometary coma. However, retrieving the compositions in the coma to the compositions in the nucleus itself is actually challenging (Le Roy et al. 2015). Thanks to the Rosetta mission, we obtained the surface information of comet 67P/C-G in situ and even directly by the lander, Philae. Several complex organic molecules (COMs) have been detected on the surface of the comet 67P/C-G by COSAC (Cometary Sampling and Composition) which is on broad Philae, and four out of sixteen are detected for the first time (Goesmann et al. 2015). On the other hand, the instrument aboard Rosetta, VIRTIS (Visible Infrared Thermal Imaging Spectrometer) measured a broad absorption band feature in the 2.9 μm to 3.6 μm centered at 3.2 μm over 3 different regions (e.g., head, neck, and body) on the surface of comet for the first time (Capaccioni et al. 2015; Figure. 3.1). The measurement is obtained from August to September 2014 with heliocentric distance from 3.6 to 3.3 au. The comparison between different regions indicated that there is less effect from the solar wind radiation on 3.2 μm. By comparing the observed spectra with the experiments in the laboratory, it is suggested that Carboxylic acids group (R-COOH) along with NH_4^+ are the highly plausible candidates to account for the broad absorption features (Quirico et al. 2016).

Meanwhile, comparisons between the protoplanetary disk models coupling with chemical network and comet 67P/C-G had been done (Walsh 2015; Drozdovskaya et al. 2016). The results in Walsh (2015) show the consistency of some COMs (e.g., CH_3CN, NH_2CHO, $HOCH_2CHO$, CH_3COCH_3) but not for the relatively large COMs observed by Rosetta (e.g., $HOCH_2CH_2COH$, C_2H_5CHO, $C_2H_5NH_2$). It might be due to the lack of the chemical network of grain-surface reactions or indicate that there are other possible pathways, e.g., mantle reactions, which allows the reactions occur inside the ice mantle.

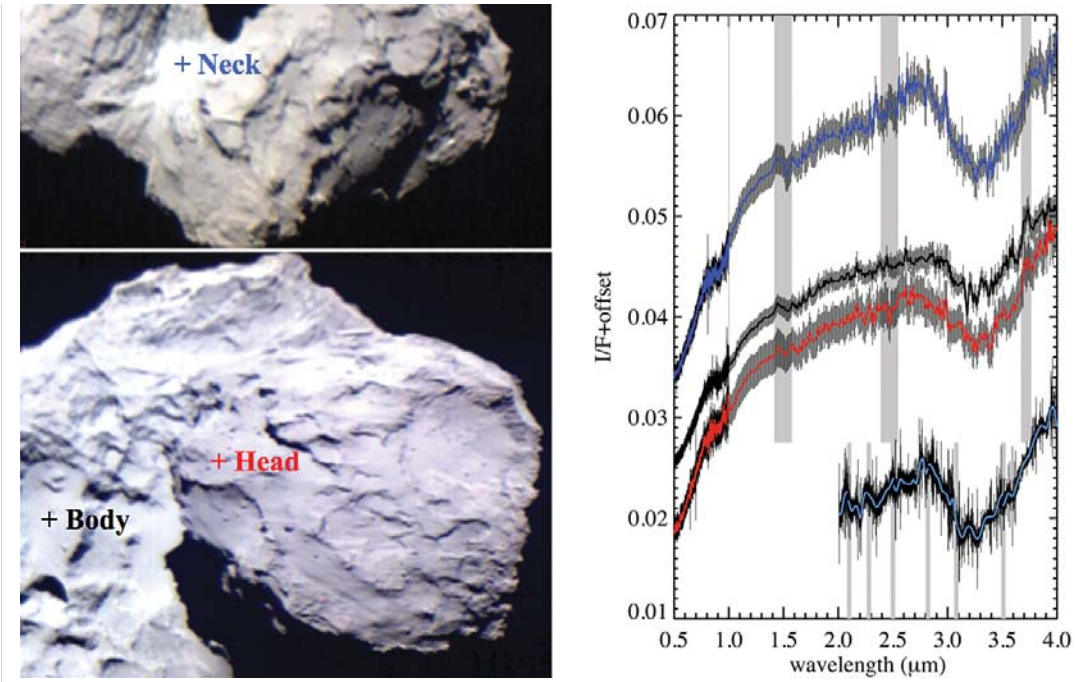

Figure 3.1: Left panels show regions corresponding to the reflectance spectra on the right hand side with the same color. All regions show the clear absorption in 2.9μm to 3.6 μm (Figure is taken from Capaccioni et al. 2015).

At low-temperature the formation COMs by ice chemistry is poorly known. The bulk ice diffusion are thought to be inefficient, and thus in astrochemical model, COMs are thought to be mainly formed on the surface of the ice mantle through the grain-surface chemistry. However, recent laboratory experiments show that COMs not only form on the grain surface but can be formed inside ice mantles via some pure thermal reactions. Experiments show these pure thermal reactions can occur inside the ice bulk without diffusion since they are abundant enough (e.g., H_2O, CO_2, NH_3 and H_2CO) and statistically, pairs of reactants reside in neighboring sites (Theulé et al. 2013). Besides, the other experiment demonstrates a strong correlation between the reaction kinetics in bulk ices and their structural evolution such as pore collapse and crystallization which breaks the conventional picture of reactants diffusing in the bulk ice. They deposit a gas mixture of NH_3, CO_2 and H_2O on a substrate covered with pure ice water layer to ensure the consumption of reactants was solely due to the reaction: CO_2+NH_3 $\rightarrow$ $NH_4{}^+NH_2COO^-$ (see left panel of Figure 3.2). Also, this reaction is with a lower activation barrier comparing to the bulk diffusion barriers. While increasing the temperature to a certain values, the substrate is monitored by the spectrometer. The evolution of reactants and products abundances can be deduced

from their IR absorption bands. The experiment results show the correlation between the evolution of reactants, products and the structural changing of the amorphous ices, indicting that the reactions are driven by the structural changing. The diffusion of reactants inside the ice bulk are likely occurs along the cracks generated by the structural changing and thus mantle reactions are thought to occur along the cracks as well. The right panels of Figure 3.2 show the schematic view of cracks forming inside the ice during the crystallization of amorphous ice, where the reactions are thought to occur. Therefore, the reaction occurring inside the ice mantle are expected to increase the complexity and the production rate of interstellar COMs (Ghesquière et al. 2018).

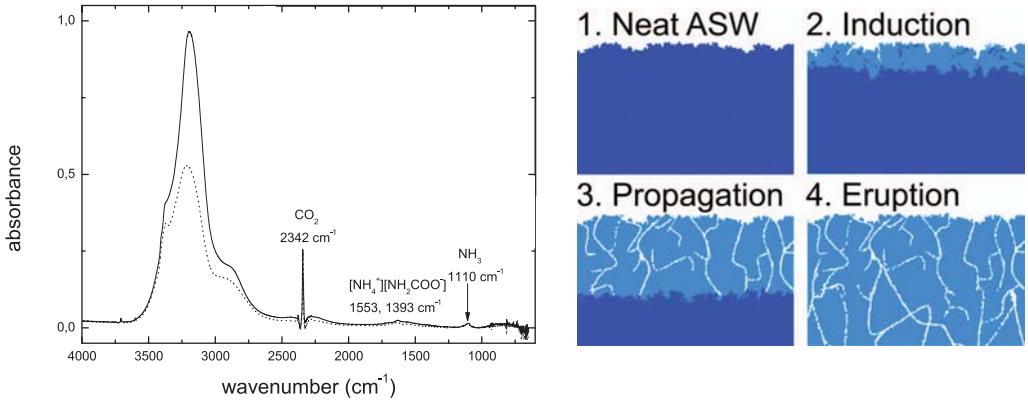

Figure 3.2: Left panel is the FTIR spectrum showing the initial state of an experiment, NH_3:CO_2:H_2O ice mixture at 80 K (dotted line) and after the water ice cover on the ice mixture on top of it (solid line) (Modified from Ghesquière et al. 2018). The right hand side panels show the schematic view of cracks forming inside the ice during the crystallization of amorphous ice (Taken from (May et al. 2013) .

According to the experiments, it suggests that mantle reactions become efficient when the temperature is high enough to crystallized the amorphous ice (Ghesquière et al. 2018). Therefore, we consider the FU Ori type outbursts which occur repeatedly during Class I and Class II stages (observational paper). The sudden increment of mass accretion rate raises the temperature inside the disk and further enhances the efficiency of mantle reactions. Besides, considering the FU Ori outburst expands the possible region where comets form if assuming comets were formed in-situ, because most of the COMs are thought to be formed by grain surface reactions, which occur efficiently in the warm environment around 20-50K (depending on the binding energy of each molecules as well). By considering mantle reactions into the chemical network, we open an additional pathway to synthesize COMs even under high temperature environment and increase the complexity of the molecules in the ice mantle.

In this study, we aim to investigate the effect of the mantle reactions and compare it with the observation from Rosetta mission, especially focus on chemical compounds which make the broad absorption features centered at 3.2 μm. We present the physical setting and the chemical model in the Section 3.2 and the results and discussion in Section 3.3. Finally, we summarize the study in the Section 3.4.

3.2 Methodology

3.2.1 Physical Model

We consider a single-point model with three different H_2 density which are 10^5, 10^6 and 10^7 cm^{-3} as our physical setting. In this study we aim to investigate how temperature variation affects the efficiency of the mantle reactions. The increment of temperature is driven by the FU Ori type outburst. During the outburst, the brightness of FU Ori objects increases $\sim$ 4 orders of magnitude or more. The increment of brightness is due to the sudden raise of the mass accretion rate to the central protostar. We set up three sets of temperature variation, which are 10k-30K, 80-100K and 80-120K, assuming every outburst lasts for 100 years and remains in the quiescent state for 10^3 and 10^4 years for 5 cycles based on the observation (Hartmann & Kenyon 1996). For the low temperature variation setting we follow the same condition as Visser & Bergin (2012) to confirm the consistency with the other chemical model at low temperature. For the other two temperature settings, 80K represents the temperature with slow processing mantle reactions. 100K and 120K are set in order to understand the efficiency of mantle reactions under different temperature.

3.2.2 Chemical Reaction Network

In this chemical model, we consider three different phases including gas, surface, and mantle phase (Hasegawa & Herbst 1993) instead of gas and ice in Chapter 2. Besides, we not only consider the gas-phase reactions and gas-grain interactions, but include the grain surface reactions and mantle reactions with an escaping mechanism which allows the mantle phase release to the gas phase. The details of the interaction between each phase will be introduced in the Section 3.2.2.4.

The initial abundance setting is the result based on the elemental abundance ($He:C^+:N:O:Na^+:Mg^+:Si^+:S^+:Cl^+:Fe^+$ are 0.14:7.3(-5):2.14(-5):1.76(-4):3.00(-9):3.00(-9):3.00(-9):2.00(-8):3.00(-9):3.00(-9) (see Table 2.1 in Section 2.2)) at T = 10K lasting for 10^5 years with three different H_2 density as mentioned above (Table 3.1).

Briefly mentioned here that as the density increases, the adsorption rate which is proportional to hydrogen density, increases simultaneously (see Equation 2.17). Therefore, the gas-phase abundance decreases and mantle-phase abundance increases since gaseous molecules freeze on the dust grain easier. However, for some of the molecules, such as NH_3, H_2CO, and CH_3OH, the mantle-phase abundance decreases as the density increases. In the case of NH_3, it is affected by N_2. If the freeze-out timescale of N_2 is shorter than the timescale of forming NH_3 by grain surface reactions, N_2 will be accumulated on grains while NH_3 can not be formed efficiently. In the case of H_2CO and CH_3OH, it could be related with the formation rates of CH_4 and CO_2 verse those of H_2CO and CH_3OH. At high density, it seems that CH_4 and CO_2 are preferably formed.

Species	Gas			Mantle			E_d (K)
H_2 dens.	10(5)	10(6)	10(7)	10(5)	10(6)	10(7)	
N_2	1.51(-06)	1.76(-08)	1.35(-09)	7.96(-07)	2.47(-06)	3.58(-06)	790
CH_4	2.88(-07)	6.46(-10)	1.00(-12)	9.52(-06)	1.23(-05)	1.33(-05)	1090
CO	3.42(-05)	6.94(-08)	2.16(-11)	1.90(-05)	5.14(-05)	5.10(-05)	1150
OH	8.88(-09)	1.67(-08)	1.00(-14)	1.17(-14)	1.60(-14)	3.57(-14)	2850
H_2CO	5.84(-09)	9.06(-11)	1.53(-18)	5.72(-06)	4.55(-06)	3.28(-06)	2050
NH_3	4.38(-09)	2.91(-09)	1.02(-11)	1.98(-05)	1.59(-05)	1.33(-05)	2790
CO_2	2.03(-07)	1.08(-10)	6.33(-24)	1.96(-07)	8.00(-07)	9.86(-07)	2990
HCN	1.27(-09)	6.85(-11)	2.05(-16)	2.35(-08)	1.98(-07)	5.59(-07)	4170
H_2O	5.72(-08)	9.22(-10)	6.09(-16)	7.06(-05)	1.16(-04)	1.17(-04)	4820
CH_3OH	1.06(-12)	4.36(-16)	2.56(-27)	1.33(-06)	7.33(-07)	5.89(-07)	4930

Table 3.1: The initial abundances of both gas- and mantel-phase relative to total hydrogen nuclei under three different densities of molecular hydrogen. It is ordered by the value of binding energy and $a(b)$ represents $a \times 10^b$.

3.2.2.1 Gas-Phase Reactions

We adopted the latest version of the UMIST Database for Atrochemistry, Rate12 into our chemical model (McElroy et al. 2013) instead of using Rate06 used in the previous Chapter, since the updated Rate12 network includes more comprehensive reaction sets relating to COMs. Furthermore, as mentioned in McElroy et al. (2013), the major differences compared to Rate06 (Woodall et al. 2007) is the inclusion of anions reactions which enhanced the carbon-chain molecules (Walsh et al. 2009). In this network, there are 506 gas-phase species and 6900 gas-phase reactions, including two-body reactions, photoreactions, X-ray/cosmic-ray-induced photoreactions,

and reactions of direct X-ray/cosmic-ray ionization. The formula for the gas-phase reaction rates are the same as we present in Section 2.2.2.1 and Appendix 2.5.1 in the previous chapter.

3.2.2.2 Grain Surface Reactions

The grain surface reaction occurs on the top most layer of the ice mantle. In our chemical model, it is corresponding to the species in the surface phase. Our grain surface reaction network is taken from Garrod et al. (2008). The calculation method of the reaction rate can be found in Tielens & Allamandola (1986) and Hasegawa et al. (1992). The rate coefficient of grain surface reaction between species i and j can be defined as

$$k_{i,j} = \kappa_{i,j}(R_{diff}(i) + R_{diff}(j))(1/n_d) \tag{3.1}$$

where $\kappa_{i,j}$ is the probability for the reaction to happen on an encounter, R_{diff} is the diffusion rate of the species and n_d is the dust number density. If the reaction is exothermic, the probability is unity. For reactions with an activation barrier, E_a, and at least one light reactant (i.e., H or H_2), the probability can be approximated as the exponential term of the quantum mechanical probability for tunneling the barrier with thickness of b.

$$k_{i,j} = \exp(\frac{-2b}{\hbar}\sqrt{2\mu E_a}), \tag{3.2}$$

where b is the barrier thickness assumed to be 1 Å, and μ is the reduced mass of species i and j, μ=m_i m_j/(m_i+m_j). For R_{diff}, it is the inverse of the diffusion time, t_{diff}=N_{site} t_{hop}, where N_{site} is the number of sites adopted for adsorption on an average grain, assumed to be 1×10^6. The time scale for t_{hop} for a species migrating from a site (potential well) to an adjacent site by thermal hopping can be written as

$$t_{hop}(i) = \nu_0(i)^{-1}\exp(E_b(i)/kT_d), \tag{3.3}$$

where ν_0 is the vibrational frequency of each adsorbed species in its potential well (see equation 2.19). The barrier between each surface sites, E_b is assumed to be $0.3E_d$, here E_d is the binding (desorption) energy and T_d is the dust temperature. However, for the light species H and H_2, the surface migration through quantum tunneling is much more rapid than the thermal hopping. Therefore, the time scale of light species tunneling through the barrier to the adjacent site can be represented as

$$t_q(i) = \nu_0(i)^{-1}exp(\frac{2b}{\hbar}\sqrt{2m_iE_b(i)}). \tag{3.4}$$

3.2.2.3 Mantle Reactions

The mantle reactions in our network are based on the laboratory experiments adopting from Theulé et al. (2013). Referring to Ghesquière et al. (2018), the mantle reaction can be driven by the structure changing of the ice mantle and the structure changing is due to the transformation of amorphous ice to crystallized ice T ≥ 120 K). Therefore, we constructed a formula for the reaction rates of mantle reactions. In order to make sure the correlation between the crystallization rate and the mantle reaction rates, we adopt the rate coefficient of water crystallization to the mantle reactions by considering the following reactions to reproduce the data shown by the experiments.

$$H_2O_{amorphous} \rightarrow H_2O_{crystallized} \tag{3.5}$$

$$NH_3 + CO_2 \rightarrow NH_3COO \tag{3.6}$$

$$NH_3 + NH_3COO \rightarrow NH_4{}^+NH_2COO^- \tag{3.7}$$

For the mantle reaction rates, we adopt rate coefficient of water crystallization times the minimum number density of the reactants (Equation 3.8), which is reasonable since the reactions are determined mainly by the abundance of the minimum reactants.

$$\frac{dn_m(k)}{dt} = k_{cry}\min[n_m(i), n_m(j)], \tag{3.8}$$

which represents the reaction, $i_{mantle} + j_{mantle} \rightarrow k_{mantle}$, the water crystallization rate, k_{cry}=1.2 × 10^{21} exp(-E_a/8.3/T_d) s^{-1} and E_a is assumed to be 65.7 KJ/mol based on the experiment (Smith et al. 2011). Figure 3.3 shows the experiment results and our model results with corresponding temperature. The vertical axis represents the abundance of each molecules normalized to the maximum of itself. The reaction rate in the model shows a good agreement with the experiment.

3.2.2.4 Interaction between Different Phases

In the three phase model, species are separated in to gas, surface, and mantle phase. The interaction of each phase can be transformed by different pathway. In the case of gas-phase and surface phase, the interaction is determined by the adsorption, thermal, and non-thermal desorption. The details of the reaction rates can be found in Appendix2.5.1.

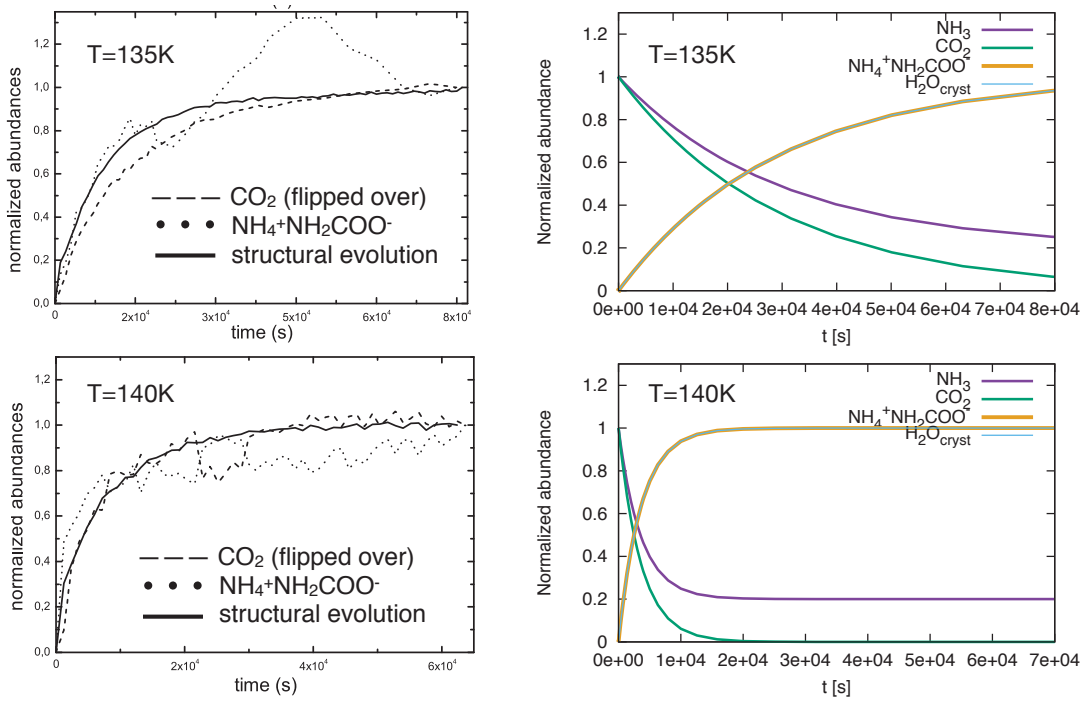

Figure 3.3: Left panels show the experiment results from Ghesquière et al. (2018). Right panels show the results based on our model under corresponding temperature.

Once the species are adsorbed on the grain surface and start to pile up, we distinguish the surface and mantle phase following Hasegawa & Herbst (1993). We define the core coverage factor α ($0 \leq \alpha \leq 1$) as the following equation

$$\alpha = n_s / N_{site} n_d, \tag{3.9}$$

where n_s represents the total number density of the surface phase (n_s=Σ_i $n_s(i)$), N_{site} is the number of sites adopted for adsorption on an average grain and n_d is the number density of dust. We consider two conditions. First, the net accretion from gas to surface is positive ($[dn_s(i)/\mathrm{dt}]_0 > 0$) , then

$$\frac{dn_s(i)}{dt} = [\frac{dn_s(i)}{dt}]_0 - \alpha[\frac{dn_s}{dt}]_0 \frac{n_s(i)}{n_s}, \tag{3.10}$$

where the first term on the right-hand side is the net accretion of species i from gas to surface and the second term represents the conversion of specie i from surface to mantle depending on the the core coverage factor α. The rate of species i in the mantle phase is given by

$$\frac{dn_m(i)}{dt} = [\frac{dn_m(i)}{dt}]_0 + \alpha[\frac{dn_s}{dt}]_0 \frac{n_s(i)}{n_s}. \tag{3.11}$$

For the second condition, the net accretion from gas to surface is negative ($[dn_s(i)/\mathrm{dt}]_0 < 0$), then

$$\frac{dn_s(i)}{dt} = [\frac{dn_s(i)}{dt}]_0 - \alpha[\frac{dn_m}{dt}]_0 \frac{n_m(i)}{n_m}. \tag{3.12}$$

In this case, species i on the surface will desorb into gas phase and at the same time, species i inside the ice mantle will transform into surface layer to replace the lost sites on the grain surface. The rate of species i in the mantle is

$$\frac{dn_m(i)}{dt} = [\frac{dn_m(i)}{dt}]_0 + \alpha[\frac{dn_s}{dt}]_0 \frac{n_m(i)}{n_m}. \tag{3.13}$$

On the other hand, we add a pathway letting the molecules inside the mantle ice escape to the gas phase. From the experiment results, we noticed that gas can be transported through the pores inside the porous amorphous ice even if they were deposited beneath the water ice (Ayotte et al. 2001). The desorption of the gas is detected even at low temperature. Molecules show continuous desorption during the intermediate temperature and it might be due to the connection between different pores to the surface. As the temperature goes higher, water ice starts to crystallize ($\approx \geq$ 120K). The crystallization will induce the cracks formed and propagates top-down inside ice bulk. If the crack inside the ice connected to the surface, it can open a pathway letting the gas trapped inside the ice release out or the ice along the crack can desorb into the gas phase (Ayotte et al. 2001; Burke & Brown 2010; May et al. 2013). However, the effect of releasing molecules from the ice mantle largely depends on the ice structure (porosity) and the heating rate which in terms relates to the thermal history during the formation (Ayotte et al. 2001; Bossa et al. 2012).

In this study we simply assumed only the species with binding energy less than or equal to the binding energy of CO can escape with the escaping rate (k_{escape}), which is assumed to be the same as the thermal desorption rate (Equation 2.18). We will discuss this setting in the Section 3.3. The fraction of how much of the mantle ice can escape is defined as follows,

$$n_m^{escape}(i) = \begin{cases} n_{m(i)} & (n_{ice} < n_{act}) \\ n_{act}\frac{n_m(i)}{n_{ice}} & (n_{ice} \geq n_{act}) \end{cases} \tag{3.14}$$

where $n_m(i)$ is species i in the mantle phase, n_{act}=$4\pi r_d^2 n_d n_{site} N_{LAY}$ represents the number of active surface sites in the ice mantle per unit volume, where N_{LAY} is the number of surface layers considered as active, here we assumed it as two, r_d is the dust grain radius, n_{site} is the surface density of sites, $n_{site} = 1.5\times10^{15}$ cm^{-2}, and n_d is the number density of dust grains (see Section 2.2.2.2 and Appendix 2.5.1 for the details). n_{ice}

is the combination of all the species in the surface and mantle phase. Therefore, the modified gas-phase and mantle-phase rate can be represented as

$$\frac{dn_m(i)}{dt} = [\frac{dn_m(i)}{dt}]_0 - n_m(i)n_m^{escape}(i)k_{escape} \tag{3.15}$$

$$\frac{dn_g(i)}{dt} = [\frac{dn_g(i)}{dt}]_0 + n_m(i)n_m^{escape}(i)k_{escape}, \tag{3.16}$$

where $n_g(i)$ is the number density of gas species i.

3.3 Results and Discussion

3.3.1 The Effect of FU Ori Outburst

In this subsection, we address the effect of the timescale of outburst cycle towards the behavior of molecular abundance. First, we examine it under low temperature condition in which mantle reaction hardly occurs. The temperature changes from 10K during quiescent time to 30K during the outburst. Since the temperature is across the desorption temperature of both CO and N_2, which is $\approx$ 20K, we expect to see the abundance variation due to the adsorption and desorption. Figure 3.4 shows the molecular abundance variation in gas phase. On the left-hand side and right-hand side columns present the quiescent duration of 10^3 and 10^4 years, respectively, and from top to bottom, results of different cases of H_2 density are shown.

During each quiescent time, temperature is low enough to make CO and N_2 adsorb on the grain surface, and thus the molecular abundances decrease. When outburst occurs, the temperature increases. The molecules frozen on the dust grain convert back to the gas-phase by thermal desorption. Therefore, the outburst events can be regarded as a cycle of adsorption and desorption. However, as the figure shows, CO and N_2 do not decrease under all the physical conditions. The critical factor is the timescale. The behavior is strongly controlled by the quiescent timescale and the adsorption timescale. The adsorption timescale can be approximated as

$$\tau_{ads,i} = 2.1 \times 10^4 yr \frac{10^6 cm^{-3}}{n(\mathrm{H})} \sqrt{\frac{10\mathrm{K}}{T_{gas}}} \sqrt{\frac{m_i}{28}} \tag{3.17}$$

where m_i is the molecular weight of species. From Equation 3.17, the adsorption timescale is inverse proportional to the H_2 density. In the case of CO, the adsorption timescales approximate to 10^5, 10^4 and 10^3 years with respect to the H_2 density=10^5,

10^6 and 10^7 cm^{-3}. As a result, panel (f) shows the most significant abundance variation since the timescale of adsorption is 10 times less than the timescale of quiescent state and in panel (a), (b) and (d), they are opposite. Therefore, it is difficult to see the changing of the molecular abundances. Panel (c) and (d) are the cases in between which have the equivalent timescale.

For ion molecules, HCO^+, $H_3{}^+$ and N_2H^+, they are closely related to CO and N_2. The destruction pathways of $H_3{}^+$ are through the collision between both CO and N_2 and it can produce HCO^+ and N_2H^+. Also the main destruction pathway of HCO^+ is the electron recombination, producing CO and H_2. For N_2H^+, it is produced by the proton transfer between CO and produce HCO^+ and N_2. In panel (f), during the quiescent time, $H_3{}^+$ increases because CO and N_2 become depleted. In the case of HCO^+, the production rate is proportional to the abundances of CO and $H_3{}^+$. As CO decreases and $H_3{}^+$ becomes saturated, the production rate becomes less efficient and thus the abundance decreases. In the case of $NH_2{}^+$, it is balanced by the formation through N_2 and the destruction by CO. During the cold phase, the deletion of CO slows down the destruction rate and it is less than the production rate. Meanwhile, since the production rate of it is proportional to the abundances of N_2 and $H_3{}^+$, as N_2 becomes saturated, N_2H^+ maintains at the same level as well.

From these results, we understand the relation between the behavior of molecular abundance based on the physical timescale of outburst and the chemical timescale and it shows a good agreement with Visser & Bergin (2012).

3.3.2 Temperature Dependency of Mantle Reactions

Besides the effect of outburst timescale, we examine the mantle reaction efficiency and estimate the reaction timescale by the rate coefficient of water crystallization under different temperature, 80K, 100K and 120K. The initial setting is extracted from the results under 15K for 10^6 years to build up the ice mantle since at low temperature molecules can adsorb on the grain surface and form various molecules such as CH_4, NH_3 and H_2O by grain-surface rations. After that, we raise up the temperature to accelerate the crystallization of water, inducing the mantle reaction simultaneously. Figure 3.5 shows the abundances of various species in mantle phase as a function of time with corresponding reaction timescale on it. As the figure shows, the molecular production is relatively small at 80K and increases as the temperature increases. It is because at low temperature water is hardly crystallized and thus mantle reactions hardly occur. The timescale of 80K is 10^{14} years, which is even longer than the history of the universe. In the 100K case, the timescale is 10^5 years. On the

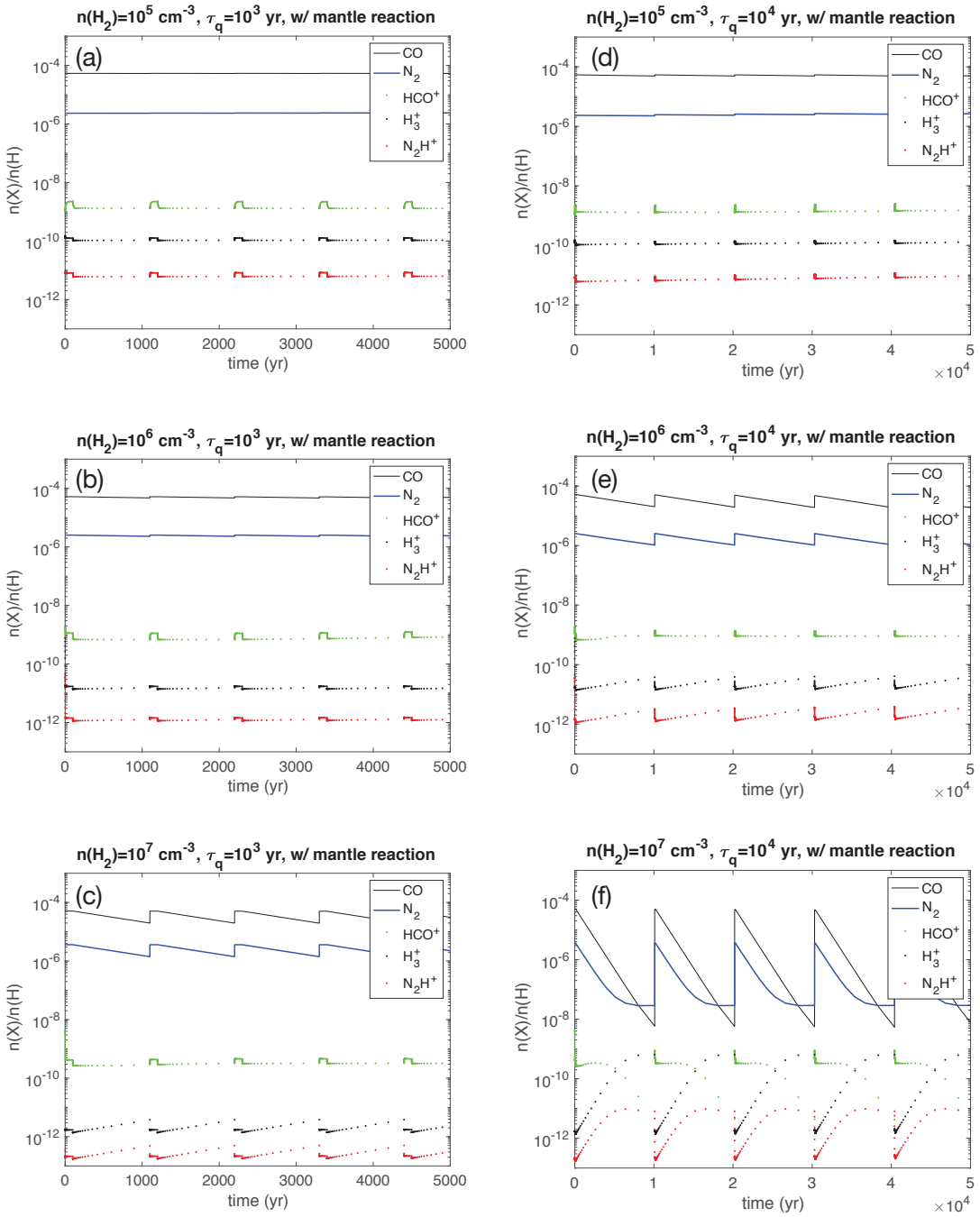

Figure 3.4: The evolution of gas-phase molecular abundance in the 10K-30k outburst model with quiescent time equals to 10^3 years (panel a-c) and 10^4 years (panel d-f) relative to different H_2 density.

other hand, when temperature reaches 120K, according to the reaction timescale, molecular abundances reach the peak when time is $\approx$ 1.5 years, and some of them become saturated after that since no destruction pathway is present in the network. Meanwhile, some of them continue to be used to the other reactions.

Furthermore, we combined the effect of outburst and present the molecular abundance variation in mantle phase in Figure 3.6. We especially focus on the reaction written in Equation 3.6 and Equation 3.7, which are the reactions to form Ammonium carbamate, the candidate accounts for the broad absorption centered at 3.2 μm showing in the cometary spectra (Figure 3.1). Solid and dotted line are the reactants, NH_3 and CO_2, respectively. Green line is the intermediate, which is produced by NH_3 and CO_2 and it will further react with NH_3 to form Ammonium carbamate, expressed by the red line. At 10-30K temperature cycle, crystallization hardly occurs and thus Ammonium carbamate is almost zero in this case. In 80-100K case, the production of Ammonium carbamate increases as the outburst repeats, since the timescale of the mantle reaction at 100K is about 10^5 years. Hence, before it reaches the maximum, the abundance will keep increasing as long as there are no destruction pathways and the reactants are sufficient. In the case of 80-120K, the timescale of 120K is 1.5 years which is shorter than the outburst timescale and consequently, the production of Ammonium carbamate reaches its peak during the first outburst and keeps the same value afterward.

3.3.3 The Molecules Affected by Mantle Reactions

Based on the results of previous subsections, since the mantle reaction becomes efficient when temperature is higher than 120K, we examine how mantle reactions affect the production of molecules especially in the mantle phase under 80-120K temperature cycle. First we present the production of Ammonium carbamate, $NH_4{}^+NH_2COO^-$ (Figure 3.7). It clearly shows that once we turn off the mantle reactions, Ammonium carbamate can not be produced, since in the network the only way to produce it is through the mantle reactions. Also, as we showed in Figure 3.6, the abundances of Ammonium carbamate reaches the peak in the first outburst in all the cases and the abundances are $\sim 10^{-7}$ to 10^{-6} relative to H density. Furthermore, as H_2 density increases, the more CO_2 can be incorporated inside the ice mantle due to higher adsorption rate (see Tabletab:3.1). As a result, with larger amount of reactants, more Ammonium carbamate can be produced. However, the amount of the production is constrained by the reactants with smaller number density (see Equation 3.8). In all the cases of H_2 density, the production of Ammonium carbamate already reach its

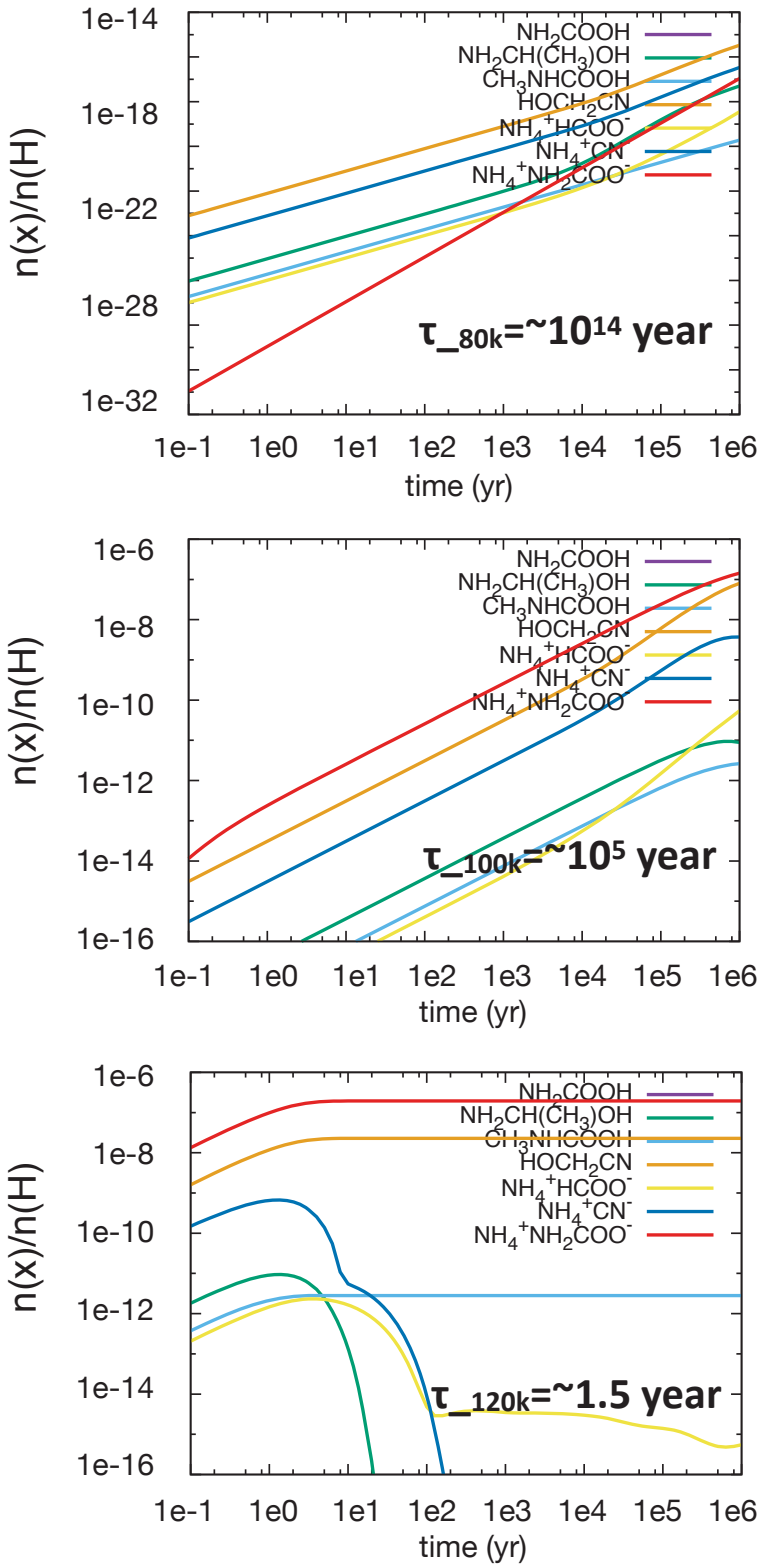

Figure 3.5: Abundance variation under three different temperature, from top to bottom is 80K, 100K, 120K with corresponding reaction timescale based on the rate coefficient of water crystallization.

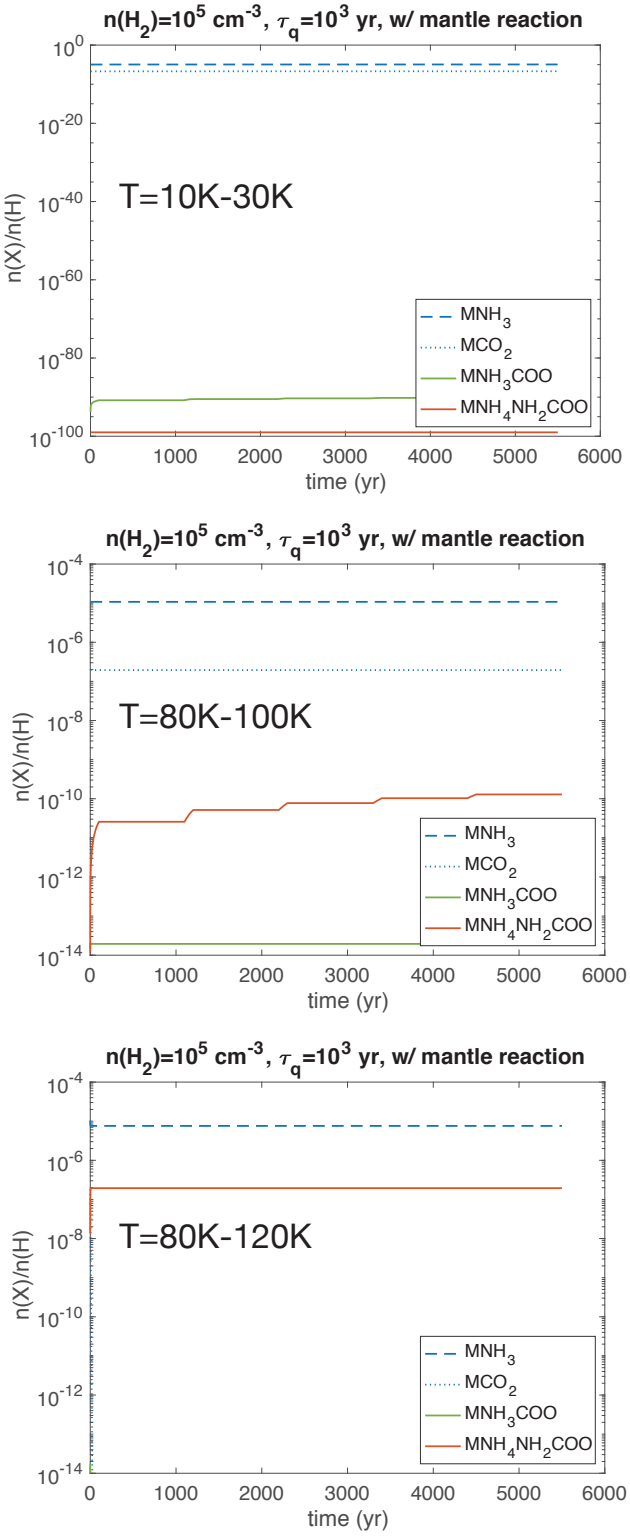

Figure 3.6: Abundance variation under different temperature variation, from top to bottom is 10-30K, 80-100K, 100-120K.

maximum since it is almost the same as the abundance of CO_2. Therefore, even if we raise up the temperature, the results would not change much until CO_2 and NH_3 start to desorb into gas phase.

Besides the Ammonium carbamate, we target the reactions with abundant reactants (e.g., $H_2CO + H_2O \rightarrow HOCH_2OH$, $H_2CO + NH_3 \rightarrow NH_2CH_2OH$) in the mantle phase (Figure 3.8). The production of them are similar to Ammonium carbamate which are $\sim 10^{-7}$to 10^{-6} in abundance. Moreover, both $HOCH_2OH$ and NH_2CH_2OH would further react with H_2CO and HCOOH to form refractory species by condensation reaction, which is the reaction that can combine two molecules into a larger molecule with loss of a small molecule (Theulé et al. 2013). Although we do not include condensation reactions in our chemical network, the formation of $HOCH_2OH$ and NH_2CH_2OH could lead to refractory species which are thought to be a part of the organic residue found in meteorites and comets (Theulé et al. 2013).

In the case of relatively small molecules, e.g., H_2CO and HCOOH, CH_3OH, we present the molecular abundance in three phases (Figure 3.9), where solid line is gas-phase, dashed line is grain surface phase and dotted line is mantle phase. First if we compare them in both gas-phase and grain surface phase, there is almost no difference between w/ and w/o mantle reactions and the variation between each outburst cycle is dominated by the adsorption and desorption mechanisms. As a result, the behavior of gas-phase and grain surface phase is opposite. When temperature is high, the species on the grain surface goes to gas-phase and when it turns back to the cold state, species in the gas phase freeze back to the grain surface. In the contrary, in the case of mantle phase, H_2CO depleted ~ 10 orders of magnitude since it is used to make the other molecules, such as $HOCH_2OH$ and NH_2CH_2OH which we mentioned before. HCOOH also decreases about an order of magnitude and for CH_3OH, it remains the same since no mantle reactions related to it included in our network. However, one thing should be kept in mind is that the mantle reaction sets are not completed yet and also the reactive part might just be a portion of the mantle instead of the total mantle.

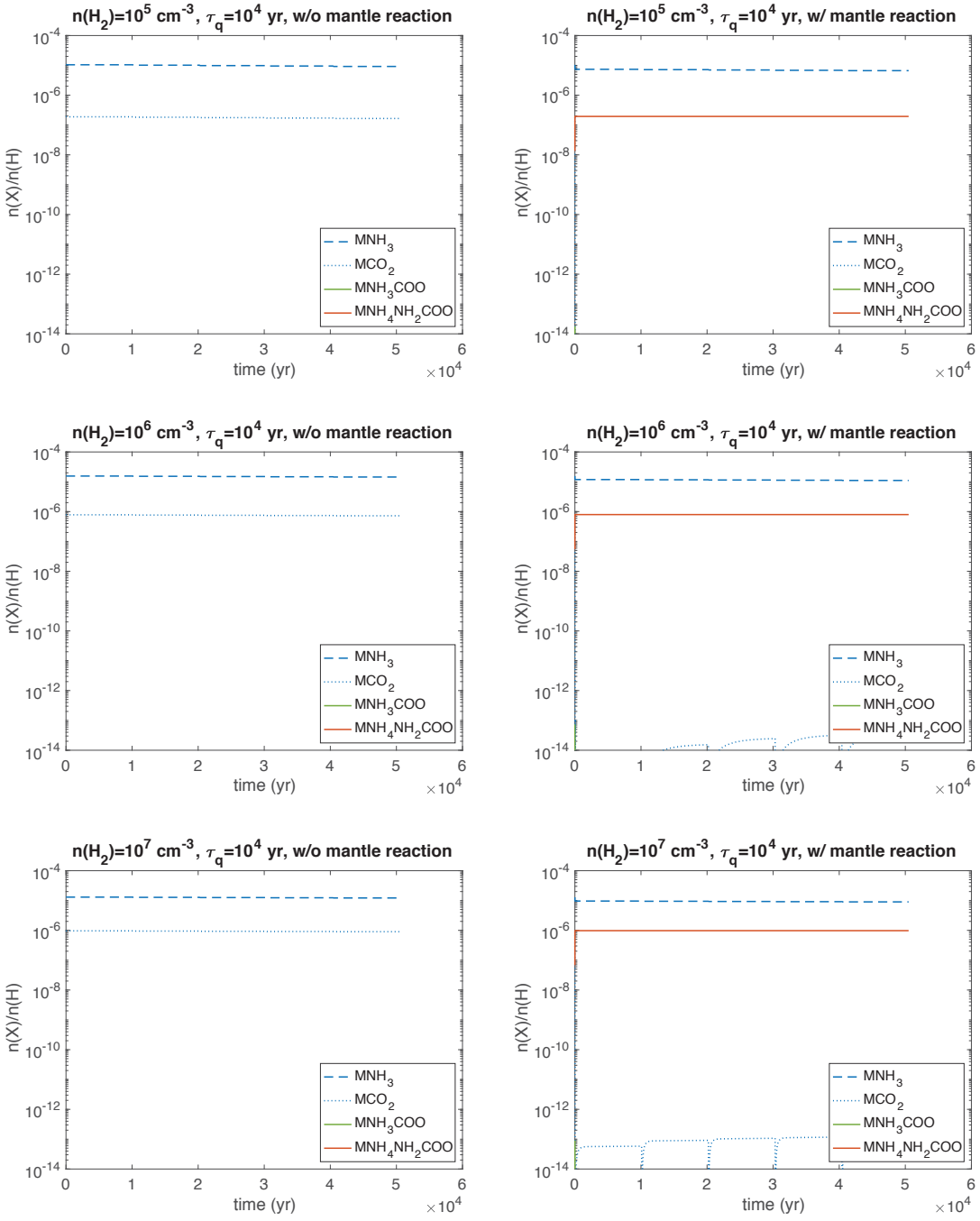

Figure 3.7: The mantle-phase molecular abundance as a function of time in the 80K-120k outburst model with quiescent time of 10^4 years relative to different H_2 density. The left-hand side columns are the results without mantle reactions and right-hand side columns are results with mantle reactions.

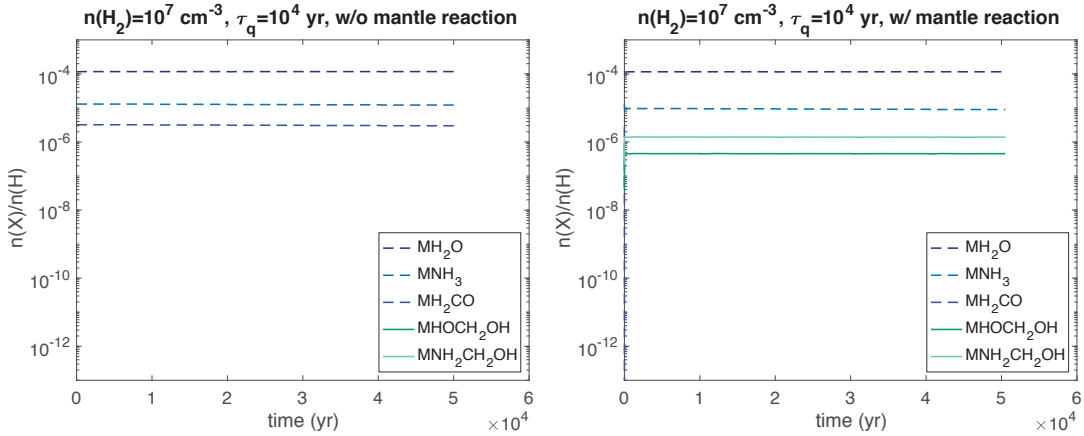

Figure 3.8: Same as Figure 3.7, but only for the condition of H_2 density=10^7 cm^{-3}. Dash line represents the reactants and solid line is the product.

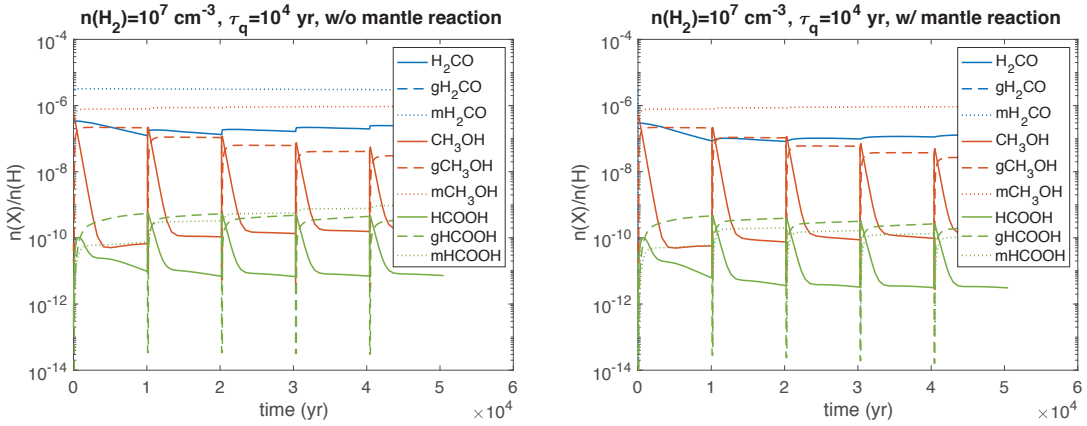

Figure 3.9: Same as Figure 3.8, but solid line represents gas-phase, dashed line is grain surface phase and dotted line is mantle phase.

3.3.4 Discussion on the Thermal History of the Comet 67P/C-G

We plot the midplane temperature as a function of disk radius in Figure 3.10. Based on the midplane temperature we obtained by the physical model in Section 2.2.1 with mass accretion rate, $\dot{M}$=10^{-8} M$_\odot$yr^{-1}, we simply assumed $T \propto \dot{M}^{1/4}$ by considering T=$T_{accretion}$+$T_{irradiation}$, in which

$$T^4_{accretion} = \frac{3GM_\star\dot{M}}{8\pi\sigma r^3}(1 - \sqrt{\frac{R_\star}{r}}), \tag{3.18}$$

where G is the gravitational constant, $M_\star$ is the mass of central star, σ is the Stefan Boltzmann constant, r is the disk radius and $R_\star$ is the radius of central star. As mass accretion rate increases, we consider the accretion luminosity instead of the

luminosity directly from the central star as follows

$$T^4_{irradiation} = \frac{GM_\star \dot{M}}{R_\star} \frac{1}{4\pi r^2 \sigma}. \tag{3.19}$$

As shown in equation 3.18 and 3.19, both $T_{accretion}$ and $T_{irradiation}$ are proportional to $\dot{M}^{1/4}$. Therefore, we assumed midplane temperature is T($\dot{M}$)=($\dot{M}$/10^{-8} $M_\odot yr^{-1}$)$^{1/4}$ T($\dot{M}$=10^{-8} $M_\odot yr^{-1}$) and varied the mass accretion rate from 10^{-7} to 10^{-4} $M_\odot yr^{-1}$ (Hartmann & Kenyon 1996). In figure 3.10, two vertical dashed lines denote the region of Kuiper belt, which is within 30 - 50 au, since Comet 67P/C-G is a Jupiter-family comets. 120K solid horizontal line represents the temperature over which mantle reactions occur efficiently. Meanwhile, the surface temperatures of Comet 67P/C-G with heliocentric distance of 3.6 to 3.3 au during daytime is in the range of 180-230K (Capaccioni et al. 2015) and it is also suggested that the component which is likely a major carrier of the 3.2 μm band is not volatilized at 220K (Quirico et al. 2016). As a result, we set 220K as the upper limit of the temperature. As shown in Figure 3.10, when the mass accretion rate reaches over 10^{-5} $M_\odot yr^{-1}$, FU Ori outburst can be the possible mechanism to transform water from amorphous ice to crystalline ice, and further drive the mantle reaction to produce the possible carrier, Ammonium carbamate in the ice bulk, during the early stage of the Solar system formation. Nevertheless, it is under the assumption that comets were formed already in the early stage to prevent from being drifted inward to the central star, it can be supported by for instance, the formation of planetesimals by porous icy grains outside of snowline neglecting the collisional fragmentation (Okuzumi et al. 2012). It is suggested that these fluffy icy aggregates can grow up efficiently within 10^5 years by direct collisional growth of submicron-size icy particles if fragmentation is insignificant. The other possibility to prevent from being drifting inward before dust growth is the streaming instability, which generates the clumps and further triggers the formation of planetisimals (Youdin & Goodman 2005; Johansen & Youdin 2007).

Though the ice structure of comet 67P/C-G is still under debate, based on the observed outgassing it is suggested that 67Ps nucleus contains crystalline ice and clathrates, and other ices (Luspay-Kuti et al. 2016). In this case mantle reactions driven by the water crystallization is still the possible mechanism to form Ammonium carbamate. However, we could not exclude the possibility that the components which contribute to the 3.2 μm band can be made during Comet 67P/C-G approaches the sun. In addition to FU Ori type outburst and the formation during comet approaching the Sun, the other possible heating mechanisms are, for example, the mantle reactions can produce Ammonium carbamate in the inner region of the disks, where the

temperature is within 120K to 140K. 140K is limited due to the timescale of water desorption based on the experiment (Ghesquière et al. 2018). After the production, Ammonium carbamate can be transport to the outer region of the disks and this can be supported by the discovery of crystalline silicate in the comets (Hanner 1999; Brownlee et al. 2006). The formation of crystalline silicate requires high temperature (≥ 800 K) and is examined by Bockelée-Morvan et al. (2002). They conclude that if dusts are well coupled with gas, turbulent diffusion will be efficient enough to transport the crystalline silicate outward to the comet-forming region within 10^4 years and well reproduced the observed value of crystalline silicate in the comet Hale-Bopp. However, with consideration of grain growth, the degree of radial transportation might be attenuated (Hughes & Armitage 2010). Furthermore, the transient heating due to shocks can be the possible mechanism as long as the shocks can maintain for hours to days within 120K to 140K. But whether the amount of Ammonium Carbamate being produced by shock heating can be detected by Rosetta still need to be aware.

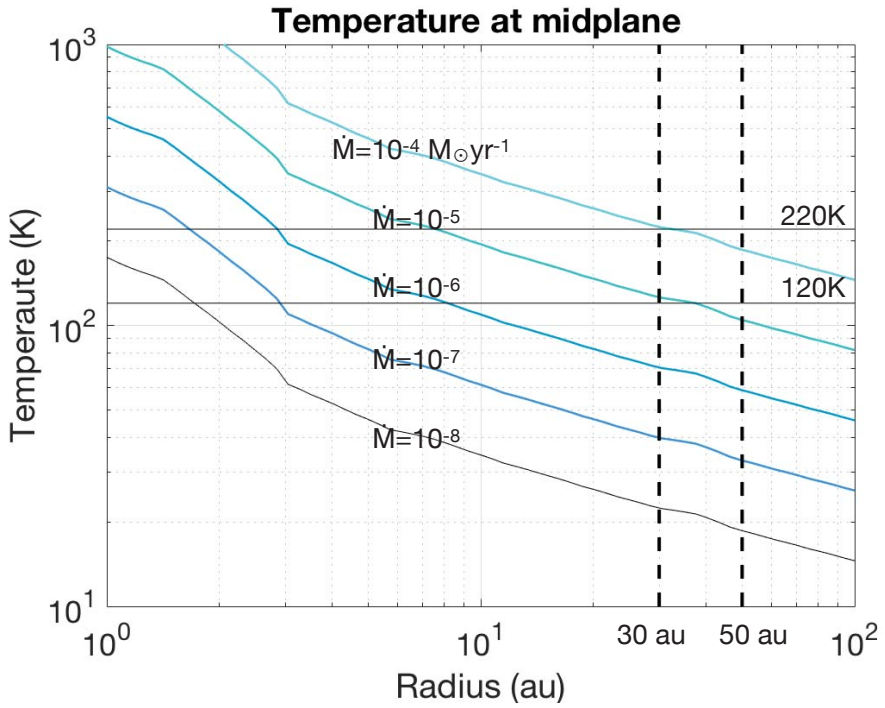

Figure 3.10: The midplane temperature as a function of distance from the central proto-star with various mass accretion rates. The temperature is based on the results of $\dot{M}$=10^{-8} M$_\odot$yr^{-1} and simply assume $T \propto \dot{M}^{1/4}$.

In addition, as mentioned in Section 3.2.2.4, we only consider the species with binding energy lower than or equal to CO can escape from the ice mantle for simplify. We set CO as the criteria to avoid trapping too much CO inside the ice mantle and thus

CO in gas phase becomes depleted even when the temperature is higher than 20K, which is not consistent with observation towards the disks (Miotello et al. 2017). Here we also examine the cases assuming all the species can escape from the ice mantle but we reduce the n_m^{escape} by multiplying Equation 3.14 with a parameter, α. We list the abundances of Ammonium carbamate in mantle phase at 120K and CO in gas phase at 30K in the case of H_2 density = 10^7 cm^{-3} in Table 3.2. The parameter is constrained by the gaseous CO abundance which is within an order of magnitude comparing to the total abundance of CO in mantle phase, which is 5.1 × 10^{-5} in this case. When α is 10^{-3}, all CO in mantle converts to the gas-phase, but at the same time, the production of Ammonium carbamate decreases about 6 orders of magnitude compared to the case only partial species (E_d(i) ≤ E_d(CO)) can escape (Figure 3.7). For the case that gaseous CO is an order of magnitude less than CO in the mantle, which α = 10^{-5}, Ammonium carbamate is ∼ 4 orders of magnitude less than the the case only partial of species can escape. In other words, the production of mantle species by mantle reaction strongly depends on how much the ice can trap the reactants inside the ice bulk, namely, the thermal history of comet 67P/C-G.

α	$NH_4^+NH_2COO^-$ at 120K	CO at 30K
10^{-5}	6.36(-10)	1.43(-06)
10^{-4}	6.36(-11)	1.43(-05)
5×10^{-3}	3.17(-11)	2.54(-05)
10^{-3}	6.36(-12)	5.01(-05)

Table 3.2: The abundance of Ammonium carbamate in mantle phase at 120k and CO in gas phase at 30K with H_2 =10^7 cm^{-3} under different α value. α value defines the fraction of how much mantle can escape to gas phase.

3.4 Summary

In this study, we construct a formula to apply the mantle reactions driven by the water crystallization based on the experiment results to the chemical model. We examined different setting of temperature and H_2 number density and conclude that the time evolution of molecular abundances changes strongly depends on the timescales of the chemistry and the temperature variation caused by FU Ori type outbursts. With the examination, we found out when temperature is higher than 120K, the molecular production due to mantle reactions can reach its maximum within one FU Ori outburst (the duration of outburst is assumed to be 100 years) and thus make large difference between the results without considering mantle reactions.

Extending the application to the recent discovery of broad absorption features in the IR spectra of Comet 67P/C-G detected by VIRTIS/Rosetta (Capaccioni et al. 2015), we confirmed that FU Ori type outburst is possible to raise the temperature to 120K even in the outer disk where Jupiter-family comets are thought to be formed if mass accretion rate is larger than $10^{-5}M_{\odot}yr^{-1}$. This is within the reasonable range of the mass accretion rate during the outburst time of the FU Ori, since the maximum of mass accretion rate during outburst time are thought to be $10^{-4}M_{\odot}yr^{-1}$ (Hartmann & Kenyon 1996). Therefore, as the temperature increases over 120K, water can be crystallized and further drive the mantle reactions occur inside the ice bulk efficiently. The consideration of mantle reactions in the chemical network can not only reproduce the possible carrier, Ammonium carbamate, which can explain the absorption features of the Comet 67P/CI-G, but also increase the molecular complexity in the ice (see Appendix 3.5.1).

Though we could not exclude the possibilities that Ammonium carbamate can be made during Comet 67P/C-G approach the sun or being made in the inner region of the disks and than being transported to the outer region, or being made by the transient heating processes like shocks, the mantle reactions still play an important role to enhance the molecular complexity when temperature is high enough. However, the amount of products is still depends on how much ice can trap the reactants inside the ice bulk and whether the timescale of mantle reactions can be comparable with or even less than other physical timescles.

3.5 Appendix

3.5.1 The Effect of Carbon Grain Destruction on COMs

In the appendix, we extended the effect of carbon grain destruction on COMs to this single-point model with a chemical network containing grain-surface and mantle reactions. First we set the H_2 density = 10^7 cm^{-3} and let the ice mantle grow in the cold phase (10K) for 10^5 years. After the cold phase, we increase the temperature to 120K at which mantle reactions can take place for 100 years.

We discussed the results into three elemental reservoirs (N, O, and C). First is the N element. We found that in both with and without carbon grain destruction case, N_2 gas is the dominant N-bearing species. But the second carrier is different from two cases, in the without carbon grain destruction case (O>C), NH_3 in icy form is the dominated one, while it is NH_2CH_2OH in the icy form in the with carbon grain destruction case (C>O). The difference is determined by the following mantle reaction, NH_3+H_2CO→NH_2CH_2OH and also the mantle reaction rate which depends on the smaller-number-density reactants (see equation 3.8). In the oxygen-rich case, the density of H_2CO is smaller than NH_3, so H_2CO determines the reaction and thus almost all H_2CO was used to produce the products, while the only portion of NH_3 was used for this reaction. On the other hand, in the carbon-rich case, it is preferable to form H_2CO and consequently, the number density of NH_3 is less than H_2CO. As a result, almost all NH_3 was used to produce NH_2CH_2OH and taking the second place of N-bearing species in the carbon-rich case. Moving to the O element. In both cases, CO gas is the most abundant species. The second-place oxygen-bearing species is H_2O in icy form and the icy carbon-bearing species which contain O as well in the without and with carbon grain destruction cases, respectively.

Finally, in the case of the elemental C reservoir, we checked the dominant species in the cold phase (10K) and outburst phase (120K) separately to see the effect from gas-phase/grain-surface reactions and mantle reactions. In the cold phase, the top three abundant carbon-bearing species are the same. They are the icy form of CO, CH_4, and H_2CO, but as mentioned above, the abundance of H_2CO is about an order of magnitude higher in the carbon-rich case comparing to the oxygen-rich case. In addition, in the carbon-rich case, excluding the top three abundant species, carbon-chain molecules such as C_2H_6 is about 4 orders of magnitude larger than the oxygen-rich case. Now we raise the temperature to 120K, in both with and without carbon grain destruction cases, CO gas and CH_4 formed in the cold phase evaporate into gas phase and the rest of 15% and 50% of carbon in the oxygen-rich and carbon-rich

environment, respectively, are mostly stored in the icy form. In table 3.3, we list the most abundant carbon-bearing species in the ice mantle. In the oxygen-rich case, excluding CH_3OH, the rest of them were made by the mantle reactions. On the other hand, in the carbon-rich case, excluding H_2OCH_2OH, others were made when they were in the cold phase and all of them are the hydrocarbon species. Combing the results together, since element carbon is more abundant in the carbon-rich case, in both cases, carbon is preferable to be used to produce the simple molecules such as CO, CH_4, H_2CO in the cold phase. In the oxygen-rich cases, after producing these three species, only 15% of carbon can be incorporated into other carbon-bearing species and as temperature increased, the rest of carbon was transformed into more complex form by mantle reactions. On the other hand, in the carbon-rich case, during the cold phase, 50% of carbon were incorporated into the other carbon-bearing species including carbon-chain molecules. Carbon-chain molecules that would not be altered by mantle reactions would stay in the ice. Meanwhile, mantle reactions produced the other COMs inside the ice, increasing the complexity of molecules in the ice.

w/o destruction	NH_2CH_2OH, $HOCH_2OH$, NH_4NH_2COOH, CH_3OH, $HOCH_2CN$
w/ destruction	C_2H_6, $HOCH_2OH$, CH_2CCH_2, CH_3CCH, C_2H_2

Table 3.3: The most abundant carbon-bearing species in the ice mantle at 120K.

Based on the results, we concluded it from 2 points. First, if we compared the dominant icy composition in table 3.3 with table 2.4 in Chapter 2, we could see how grain-surface reactions and mantle reactions increase the complexity of molecules in the icy form. But they are still consistent with each other that in the carbon-rich environment, carbon-chain molecules are favored to be produced. Second, if we compared the results in this chapter between w/o and w/ carbon grain destruction because ice build up in the low temperature, we found that grain-surface determined the ice composition first, once carbon stored into longer carbon-chain which have higher binding energy, these carbon-chain molecules can be stored in the ice form even if temperature is high. Thus with carbon grain destruction, more carbon can stay in the solid phase and vary the solid carbon to silicon ratio. Also, in the carbon-rich case, the abundance of COMs are larger than the oxygen-rich case, such as long carbon-chain species can reach $\approx$ 5 orders of magnitude differences between two cases. For others, such as CH_3OCH_3 and HCOOH, they were also enhanced by the carbon grain destruction $\approx$ 2 orders of magnitude.

3.5.2 The Effect of Grain Surface Reaction on Radial Distribution of Solid Carbon Fraction

In addition to the effect of carbon grain destruction on the formation of COMs based on the single-point model, we present the results of the radial distribution of solid carbon fraction in the midplane of disk model with extra consideration of grain surface reaction comparing to Chapter 2. The following table shows the ratio of the carbon in the solid phase relative to the solar silicon at each disk radius both for the results without and with the grain surface reactions. The results of without grain surface reactions are the same as table 2.3 presenting in Chapter 2 and we list the observed C/Si here as well (Bergin et al. 2015). As mentioned previously (Section 2.3.2), the results do increase the solid carbon to silicon ratio via grain surface reactions but the effect is only a few percent. For example, at 10 au without carbon grain destruction, it increases about 4 % when considering grain surface reactions and in the with carbon grain destruction case, it increases about 3%when considering grain surface reactions. It actually enhances the discrepancies in the asteroid belt. The C/Si ratio are the minimum values since we considered the extreme case that all the carbon were released out from the solid to the gaseous phase and thus the other mechanisms to decrease the C/Si ratio in the region of asteroid belt are needed.

	w/o grain surface		w/ grain surface			observed
	w/o des.	w/ des.	w/o des.	w/ des.		
10 au	6.25	3.62	6.51	3.74	Comet Halley	5.7
5 au	6.25	3.39	6.31	3.54	CI	0.71
4 au	6.28	3.39	6.29	3.49	CM	0.4
3 au	6.28	3.38	6.31	3.49	CV	0.08
2 au	6.25	3.31	6.26	3.30	CO	0.07
1 au	6.25	4×10^{-6}	6.25		Earth (BES)	0.001

Table 3.4: The ratio of the carbon in the solid phase relative to the solar silicon at different disk radius. The observed value refers from Bergin et al. (2015)

Besides, we list table 3.5 the same as table 2.4 in Chapter 2, the most abundant carbon-bearing species in the ice mantle in the midplane at different disk radii. Comparing both tables, we notice that first, when considering the grain surface reactions, long carbon chains (composed by atomic carbon only) hardly be the most abundant species anymore, since the hydrogenation is efficient enough to make them into hydrocarbon species such as C_6H_2 and C_9H_2 and even the CH_2CHCCH. Second, the complexity increases if we consider the grain surface reaction into the chemical

network from the view of species composed by CNO elements, for instance, the production of CH_3CN. On the other hand, they are consistent with each other that when carbon grain destruction had happened, the production of long carbon chains (hydrocarbon) are preferred. On the contrary, the oxygen-bearing carbon species would carry much of carbon in the case of without carbon grain destruction.

	without destruction	with destruction
10 au	C_3O CO_2 HCN	C_6H_2 C_4H_2 C_7H_2
5 au	HCN CO_2 CH_3CN	C_6H_2 C_7H_2 CH_2CHCCH
4 au	HCN CO_2 CH_3CN	C_6H_2 C_7H_2 C_5H_2
3 au	HCN CO_2 CH_3CN	C_6H_2 C_7H_2 C_5H_2
2 au	HCOOH HC_7N HC_9N	C_9H_2 C_8H_2 C_7H_2
1 au	C_9H_2 C_9 CH_3C_7N	

Table 3.5: The most abundant carbon-bearing species in the ice mantle in the midplane at different disk radii.

Chapter 4

Summary and Future Prospects

In the first part of the thesis, we focus on the carbon deficit problem in the inner Solar system. The Earth is dramatically carbon poor comparing to the interstellar medium and the proto-sun and gradually extends to the asteroid belt, showing the correlation between carbon to silicon ratios of inner solar system objects with heliocentric distance. It is suggested that the destruction of carbon grains has occurred before planet formation. To interpret the carbon deficit problem, we focus on two issues: (1) The carbon depletion gradient in the inner solar system. (2) Test the carbon grain destruction observationally. We perform model calculation using chemical reaction network under the physical conditions of typical protoplanetary disks and we examined the effect of carbon grain destruction by considering two extreme cases that is either all carbon in carbonaceous grains is returned to the gas or remains locked in grains. The gas phase elemental abundance ratio is C/O > 1 in the former case, while C/O < 1 is found in the latter case. For the chemical model we applied the 2-phase model considering gas-phase reactions and gas-grain interaction. We considered a T-tauri disks for the first issue and the results showed the carbon depletion gradient in the inner region of the disk if we assumed the carbon grain destruction happened in the disk but with some quantitative discrepancy. On the other hand, if there were no carbon grain destruction inside the disk, most of the carbon would keep staying in the refectory form and thus almost no carbon to silicon gradient presents in our results. The dominant factor is whether the gaseous elemental abundance of carbon is larger than oxygen or not. In the with carbon grain destruction case, $\approx$ 60 % of carbon is stored in the CO gaseous form and the amount of it is constrained by O abundance since elemental abundance of C is larger than O. In contrast, since 75 % of carbon remains in the refractory form, only $\approx$ 24 % of carbon is in the CO gaseous form. Besides, in the carbon grain destruction case, the abundance of carbon-bearing species, such as HCN and carbon-chain molecules increased significantly near the midplane, while

oxygen-bearing species are depleted. Within which, HCN shows about 8 orders of magnitude differences between with and without case. In addition, we examine if it is possible to diagnose the carbon grain destruction in protoplanetary disks by ALMA observations, based on the model calculations of molecular line emission, such as HCN lines, from the disks. Since the snowline of HCN in the T-Tauri disk is in the inner region of the disk (≈2 au), it is difficult to detect the HCN line emitted inside the snowline where the difference in the HCN abundance is large between the cases with and without carbon grain destruction. Therefore, in order to examine the effect of carbon grain destruction by observation, we consider a Herbig Ae star which has stronger radiation and thus pushes the snowline of HCN to ≈ 20 au, making it possible to be observed by ALMA. Based on our model results, we proposed that by line ratio of HCN/$H^{13}CN$ and c-C_3H_2 can be the good tracers for probing the effect of carbon grain destruction in the Herbig Ae disks.

Moving towards the outer region of the solar system, we studied the effect of mantle reactions on the formation of COMs especially focusing on reproducing the materials detected on comet 67P/C-G by Rosetta mission. In this study, we applied the 3 phase model, considering not only gas-phase reactions and gas-grain interactions but also grain-surface reactions which are thought to be an important pathway to produce COMs on the grain surface and mantle reactions occurring inside the ice mantle into our network. In the case of mantle reactions, there are a few chemical models taking them into account by assuming the same reactions rate with grain surface reactions caused by swapping such as Garrod (2013). However, some recent laboratory experiments indicate ice chemistry proceeding through the thermal process of the water crystallization inside the ice bulk, providing us the opportunity to modify the reaction rate of mantle reactions. It is also found that mantle reactions enhance the complexity of molecules and are the possible pathway to produce the candidate compounds, Ammonium carbamate, accounting for the broad absorption features in the reflected spectra of comet 67P/C-G (Quirico et al. 2016; Ghesquière et al. 2018). As a result, we constructed a formula reproducing the experiment results of mantle reactions and concluded that the mantle reactions can occur very efficiently if temperature > 120K. We further examined the effect of mantle reaction by assuming the FU Ori type outbursts occur in the disks. Though we do not know whether all systems experienced FU Ori type outbursts or not, by now FU Ori type outbursts have been observed in many targets. If the Solar system also experienced outbursts in the early stage of the evolution, once the mass accretion rate reaches over 10^{-5} $M_\odot yr^{-1}$, Ammonium carbamate can be produced ≈ 10^{-6} relative to the total number

of atomic Hydrogen. Besides, not only Ammonium carbamate but other molecules such as H_2CO, $HOCH_2OH$, and NH_2CH_2OH are affected a lot. For both $HOCH_2OH$ and NH_2CH_2OH, they might lead to refractory species that are thought to be part of the organic residue found in meteorites and comets (Theulé et al. 2013). Therefore, we address the importance of mantle reactions when the temperature is $\geq$ 120K under some assumptions with efficient mantle reactions. However, the effect of mantle reactions is still constrained by how much the reactants can be trapped inside ice bulk. In other words, it depends on the structure of ices, namely the thermal history of small bodies. Besides, we tested the effect of carbon grain destruction on the formation of COMs. The results are consistent with what we did by the 2-phase chemical model, but the molecules present in the more complex forms due to the grain-surface/mantle reactions. In the carbon-rich environment, carbon chain such as C_2H_6 and CH_3CCH enhanced around 2-4 orders of magnitude, while oxgen-bearing species are depleted. For the other COMs such as CH_3OCH_3 and HCOOH, they enhanced by the effect of carbon grain destruction as well with the differences within 2 orders of magnitude.

Finally, as we mentioned in Chapter 2, the quantitative discrepancy of carbon to silicon ratio showing in the inner region of the disk might due to the lack of grain-surface/mantle reactions which transform the molecules into complex forms and stored the carbon in the ice and further decrease the carbon to silicon ratio at 1 au where the Earth located at. Thus we will examine the effect of carbon grain destruction by our 3 phase model including grain-surface and mantle reactions as our future work. On the other hand, as we know so far there is no model able to follow the chemical composition during the complete cycle of the evolution from diffuse cloud to protoplanetary disks and further into planets or small objects. We could only finding the clues within stages to stages trying to put the pieces together to understand the whole picture of chemical evolution. The upcoming James Webb Space Telescope (JWST) covers the wavelengths of the ice feature observations at NIR and MIR, it will be able to observe ices frozen on grains in the dark cloud or ices in comets. Though it is hard to observe the ice features in protoplaneaty disks, some icy components had been detected towards edge-on disks using AKARI (Aikawa et al. 2012), as well as the face-on disks by observing the ice absorption in the spectra of scattered light and multi-wavelength imaging using Subaru Telescope (Honda et al. 2009), and thus same method might be able to be used by JWST. Together with ALMA observation and the sample return of the Hayabusa 2 mission, the observation from cloud to protoplanetary disks and small bodies in the solar system will be helpful for us

to collect the missing pieces during the evolution by comparing it with the model simulations.

Bibliography

Aikawa, Y., Furuya, K., Hincelin, U., & Herbst, E. 2018, ApJ, 855, 119

Aikawa, Y., & Herbst, E. 2001, A&A, 371, 1107

Aikawa, Y., Miyama, S. M., Nakano, T., & Umebayashi, T. 1996, ApJ, 467, 684

Aikawa, Y., Kamuro, D., Sakon, I., et al. 2012, A&A, 538, A57

Allègre, C., Manhès, G., & Lewin, É. 2001, E&PSL, 185, 49

Allende Prieto, C., Lambert, D. L., & Asplund, M. 2002, ApJ, 573, L137

Altwegg, K., Balsiger, H., Bar-Nun, A., et al. 2016, SciA, 2, e1600285

Anderson, D. E., Bergin, E. A., Blake, G. A., et al. 2017, ApJ, 845, 13

Andre, P., & Montmerle, T. 1994, ApJ, 420, 837

Andre, P., Ward-Thompson, D., & Barsony, M. 1993, ApJ, 406, 122

Armitage, P. J. 2010, Astrophysics of planet formation (Cambridge University Press)

Asplund, M., Grevesse, N., Sauval, A. J., & Scott, P. 2009, ARA&A, 47, 481

Audard, M., Abrahám, P., Dunham, M. M., et al. 2014, Protostars and Planets VI, 387

Ayotte, P., Smith, R. S., Stevenson, K. P., et al. 2001, J. Geophys. Res., 106, 33387

Bardyn, A., Baklouti, D., Cottin, H., et al. 2017, MNRAS, 469, S712

Bergin, E. A., Aikawa, Y., Blake, G. A., & van Dishoeck, E. F. 2007, 2007prpl conf, 751

Bergin, E. A., Blake, G. A., Ciesla, F., Hirschmann, M. M., & Li, J. 2015, PNAS, 112, 8965

Bergin, E. A., Du, F., Cleeves, L. I., et al. 2016, ApJ, 831, 101

Bergner, J. B., Guzmán, V. G., Öberg, K. I., Loomis, R. A., & Pegues, J. 2018, ApJ, 857, 69

Bieler, A., Altwegg, K., Balsiger, H., et al. 2015, Nature, 526, 678

Bockelée-Morvan, D., Gautier, D., Hersant, F., Huré, J. M., & Robert, F. 2002, A&A, 384, 1107

Bossa, J. B., Isokoski, K., de Valois, M. S., & Linnartz, H. 2012, A&A, 545, A82

Brownlee, D., Tsou, P., Aléon, J., et al. 2006, Science, 314, 1711

Burke, D. J., & Brown, W. A. 2010, Physical Chemistry Chemical Physics (Incorporating Faraday Transactions), 12, 5947

Capaccioni, F. a., Coradini, A., Filacchione, G., et al. 2015, Science, 347, aaa0628

Carr, J. S., & Najita, J. R. 2008, Sci, 319, 1504

Carr, J. S., Tokunaga, A. T., & Najita, J. 2004, ApJ, 603, 213

Chapillon, E., Guilloteau, S., Dutrey, A., Piétu, V., & Guélin, M. 2012, A&A, 537, A60

Churyumov, K., & Gerasimenko, S. 1972, in IAUS, Vol. 45, Cambridge University Press, 27–34

Cieza, L. A., Casassus, S., Tobin, J., et al. 2016, Nature, 535, 258

Cleeves, L. I., Bergin, E. A., O'D. Alexander, C. M., et al. 2016, ApJ, 819, 13

Dent, W. R. F., Thi, W. F., Kamp, I., et al. 2013, PASP, 125, 477

Draine, B. T. 2003, ARA&A, 41, 241

Draine, B. T. 2011, Physics of the interstellar and intergalactic medium (Princeton University Press)

Drozdovskaya, M. N., Walsh, C., van Dishoeck, E. F., et al. 2016, MNRAS, 462, 977

Dulieu, F., Minissale, M., & Bockelée-Morvan, D. 2017, A&A, 597, A56

Dutrey, A., Guilloteau, S., & Guelin, M. 1997, A&A, 317, L55

Dutrey, A., Semenov, D., Chapillon, E., et al. 2014, 2014prpl conf, 317

Eistrup, C., & Walsh, C. 2019, A&A, 621, A75

Eistrup, C., Walsh, C., & van Dishoeck, E. F. 2016, A&A, 595, A83

Elsila, J. E., Glavin, D. P., & Dworkin, J. P. 2009, M&PS, 44, 1323

Favre, C., Fedele, D., Semenov, D., et al. 2018, ApJ, 862, L2

Fayolle, E. C., Öberg, K. I., Cuppen, H. M., Visser, R., & Linnartz, H. 2011, A&A, 529, A74

Finocchi, F., Gail, H.-P., & Duschl, W. J. 1997, A&A, 325, 1264

Fornasier, S., Hoang, V. H., Hasselmann, P. H., et al. 2019, A&A, 630, A7

Furuya, K., & Aikawa, Y. 2014, ApJ, 790, 97

Furuya, K., Aikawa, Y., Nomura, H., Hersant, F., & Wakelam, V. 2013, ApJ, 779, 11

Gail, H.-P. 2001, A&A, 378, 192

—. 2002, A&A, 390, 253

Garrod, R. T. 2013, ApJ, 765, 60

Garrod, R. T., & Herbst, E. 2006, A&A, 457, 927

Garrod, R. T., Widicus Weaver, S. L., & Herbst, E. 2008, ApJ, 682, 283

Geiss, J. 1987, A&A, 187, 859

Ghesquière, P., Ivlev, A., Noble, J., & Theulé, P. 2018, A&A, 614, A107

Ghesquière, P., Mineva, T., Talbi, D., et al. 2015, PCCP, 17, 11455

Gibb, E. L., Van Brunt, K. A., Brittain, S. D., & Rettig, T. W. 2007, ApJ, 660, 1572

Glassgold, A. E. 1996, ARA&A, 34, 241

Goesmann, F., Rosenbauer, H., Bredehöft, J. H., et al. 2015, Science, 349, aab0689

Groussin, O., Sierks, H., Barbieri, C., et al. 2015, A&A, 583, A36

Güdel, M., & Nazé, Y. 2009, A&A Rv, 17, 309

Guzmán, V. V., Öberg, K. I., Huang, J., Loomis, R., & Qi, C. 2017, ApJ, 836, 30

Guzmán, V. V., Öberg, K. I., Loomis, R., & Qi, C. 2015, ApJ, 814, 53

Hamaguchi, K., Yamauchi, S., & Koyama, K. 2005, ApJ, 618, 360

Hanner, M. S. 1999, SSRv, 90, 99

Hartmann, L. 2008, The disks of pre-main-sequence stars, 2nd edn., Cambridge Astrophysics (Cambridge University Press)

Hartmann, L., & Kenyon, S. J. 1985, ApJ, 299, 462

—. 1996, ARA&A, 34, 207

Hasegawa, T. I., & Herbst, E. 1993, MNRAS, 263, 589

Hasegawa, T. I., Herbst, E., & Leung, C. M. 1992, ApJS, 82, 167

Henning, T., & Semenov, D. 2013, ChRv, 113, 9016

Herbig, G. H. 1966, Vistas in Astronomy, 8, 109

—. 1977, ApJ, 217, 693

Herbst, E., & van Dishoeck, E. F. 2009, ARA&A, 47, 427

Hogerheijde, M. R., & van der Tak, F. F. S. 2000, A&A, 362, 697

Honda, M., Inoue, A. K., Fukagawa, M., et al. 2009, ApJL, 690, L110

Horn, A., Møllendal, H., Sekiguchi, O., et al. 2004, ApJ, 611, 605

Huang, J., Öberg, K. I., Qi, C., et al. 2017, ApJ, 835, 231

Hughes, A. L. H., & Armitage, P. J. 2010, ApJ, 719, 1633

Jessberger, E. K., Christoforidis, A., & Kissel, J. 1988, Nature, 332, 691

Johansen, A., & Youdin, A. 2007, ApJ, 662, 627

Jura, M. 2006, ApJ, 653, 613

Jura, M., Xu, S., Klein, B., Koester, D., & Zuckerman, B. 2012, ApJ, 750, 69

Kenyon, S. J., & Hartmann, L. 1995, ApJS, 101, 117

Kenyon, S. J., Hartmann, L. W., Strom, K. M., & Strom, S. E. 1990, AJ, 99, 869

Klarmann, L., Ormel, C. W., & Dominik, C. 2018, A&A, 618, L1

Krolikowska, M. 2003, Acta Astronomica, 53, 195

Lada, C. J. 1987, in IAU Symposium, Vol. 115, Star Forming Regions, ed. M. Peimbert & J. Jugaku, 1

Lahuis, F., van Dishoeck, E. F., Boogert, A. C. A., et al. 2006, ApJ, 636, L145

Le Roy, L., Altwegg, K., Balsiger, H., et al. 2015, A&A, 583, A1

Lee, J.-E., Bergin, E. A., & Nomura, H. 2010, ApJ, 710, L21

Lee, J.-E., Lee, S., Baek, G., et al. 2019, NatAs, 3, 314

Leger, A., Jura, M., & Omont, A. 1985, A&A, 144, 147

Lodders, K. 2010, ASSP, 16, 379

Loomis, R. A., Cleeves, L. I., Öberg, K. I., et al. 2018, ApJ, 859, 131

Luspay-Kuti, A., Mousis, O., Hässig, M., et al. 2016, SciA, 2, e1501781

May, R. A., Smith, R. S., & Kay, B. D. 2013, JChPh, 138, 104501

McElroy, D., Walsh, C., Markwick, A. J., et al. 2013, A&A, 550, A36

Millar, T. J., Farquhar, P. R. A., & Willacy, K. 1997, A&AS, 121, 139

Millar, T. J., & Herbst, E. 1994, A&A, 288, 561

Miotello, A., van Dishoeck, E. F., Williams, J. P., et al. 2017, A&A, 599, A113

Mispelaer, F., Theulé, P., Aouididi, H., et al. 2013, A&A, 555, A13

Molyarova, T., Akimkin, V., Semenov, D., et al. 2018, ApJ, 866, 46

Mousis, O., Ronnet, T., Brugger, B., et al. 2016, ApJL, 823, L41

Müller, H. S., Schlöder, F., Stutzki, J., & Winnewisser, G. 2005, JMoSt, 742, 215

Mumma, M. J., & Charnley, S. B. 2011, ARA&A, 49, 471

Nomura, H., Aikawa, Y., Tsujimoto, M., Nakagawa, Y., & Millar, T. J. 2007, ApJ, 661, 334

Nomura, H., & Millar, T. J. 2005, A&A, 438, 923

Notsu, S., Nomura, H., Ishimoto, D., et al. 2016, ApJ, 827, 113

—. 2017, ApJ, 836, 118

Öberg, K. I., Fuchs, G. W., Awad, Z., et al. 2007, ApJ, 662, L23

Öberg, K. I., Guzmán, V. V., Furuya, K., et al. 2015, Natur, 520, 198

Öberg, K. I., Qi, C., Fogel, J. K. J., et al. 2010, ApJ, 720, 480

—. 2011, ApJ, 734, 98

Okuzumi, S., Tanaka, H., Kobayashi, H., & Wada, K. 2012, ApJ, 752, 106

Palla, F., & Stahler, S. W. 1993, ApJ, 418, 414

Pascucci, I., Apai, D., Luhman, K., et al. 2009, ApJ, 696, 143

Pickett, H., POYNTER, R., COHEN, E., et al. 1998, JQSRT, 60, 883

Pontoppidan, K. M., Salyk, C., Bergin, E. A., et al. 2014, 2014prpl conf, 363

Pontoppidan, K. M., Salyk, C., Blake, G. A., et al. 2010, ApJ, 720, 887

Preibisch, T., Kim, Y.-C., Favata, F., et al. 2005, ApJS, 160, 401

Qi, C., D'Alessio, P., Öberg, K. I., et al. 2011, ApJ, 740, 84

Qi, C., Öberg, K. I., Wilner, D. J., & Rosenfeld, K. A. 2013, ApJ, 765, L14

Qi, C., Wilner, D. J., Aikawa, Y., Blake, G. A., & Hogerheijde, M. R. 2008, ApJ, 681, 1396

Quanz, S. P., Henning, T., Bouwman, J., et al. 2007, ApJ, 668, 359

Quirico, E., Moroz, L., Schmitt, B., et al. 2016, Icarus, 272, 32

Rawlings, J. M. C., Hartquist, T. W., Menten, K. M., & Williams, D. A. 1992, MNRAS, 255, 471

Rubin, M., Altwegg, K., Balsiger, H., et al. 2019, MNRAS, 489, 594

Salyk, C., Pontoppidan, K. M., Blake, G. A., et al. 2008, ChRv, 676, L49

Savage, B. D., & Sembach, K. R. 1996, ARA&A, 34, 279

Schöier, F. L., van der Tak, F. F. S., van Dishoeck, E. F., & Black, J. H. 2005, A&A, 432, 369

Scholz, A., Geers, V., Clark, P., Jayawardhana, R., & Muzic, K. 2013, ApJ, 775, 138

Semenov, D., & Wiebe, D. 2011, ApJS, 196, 25

Shakura, N. I., & Sunyaev, R. A. 1973, A&A, 24, 337

Siebenmorgen, R., & Krügel, E. 2010, A&A, 511, A6

Smith, R. S., Matthiesen, J., Knox, J., & Kay, B. D. 2011, J. Phys. Chem. A, 115, 5908, pMID: 21218834

Taquet, V., Ceccarelli, C., & Kahane, C. 2012, A&A, 538, A42

Taquet, V., Furuya, K., Walsh, C., & van Dishoeck, E. F. 2016, MNRAS, 462, S99

Theulé, P., Duvernay, F., Danger, G., et al. 2013, AdSpR, 52, 1567

Thi, W.-F., van Zadelhoff, G.-J., & van Dishoeck, E. F. 2004, A&A, 425, 955

Tielens, A. G. G. M., & Allamandola, L. J. 1986, Composition, structure, and chemistry of interstellar dust., Tech. rep.

van Dishoeck, E. F., Jonkheid, B., & van Hemert, M. C. 2006, FaDi, 133, 231

van Dishoeck, E. F., Thi, W.-F., & van Zadelhoff, G.-J. 2003, A&A, 400, L1

Veeraghattam, V. K., Manrodt, K., Lewis, S. P., & Stancil, P. C. 2014, ApJ, 790, 4

Visser, R., & Bergin, E. A. 2012, ApJ, 754, L18

Visser, R., Bergin, E. A., & Jørgensen, J. K. 2015, A&A, 577, A102

Wakelam, V., Cuppen, H. M., & Herbst, E. 2013, arXiv e-prints, arXiv:1309.7792

Walsh, C. 2015, EAS, 75, 315

Walsh, C., Harada, N., Herbst, E., & Millar, T. J. 2009, ApJ, 700, 752

Walsh, C., Millar, T. J., & Nomura, H. 2010, ApJ, 722, 1607

Walsh, C., Millar, T. J., Nomura, H., et al. 2014, A&A, 563, A33

Walsh, C., Nomura, H., Millar, T. J., & Aikawa, Y. 2012, ApJ, 747, 114

Walsh, C., Nomura, H., & van Dishoeck, E. 2015, A&A, 582, A88

Walsh, C., Loomis, R. A., Öberg, K. I., et al. 2016, ApJ, 823, L10

Wei, C.-E., Nomura, H., Lee, J.-E., et al. 2019, ApJ, 870, 129

Weingartner, J. C., & Draine, B. T. 2001, ApJ, 548, 296

Westley, M. S., Baragiola, R. A., Johnson, R. E., & Baratta, G. A. 1995, P&SS, 43, 1311

Willacy, K. 2007, ApJ, 660, 441

Willacy, K., & Langer, W. D. 2000, ApJ, 544, 903

Wilson, D. J., Gänsicke, B. T., Farihi, J., & Koester, D. 2016, MNRAS, 459, 3282

Woodall, J., Agúndez, M., Markwick-Kemper, A. J., & Millar, T. J. 2007, A&A, 466, 1197

Woods, P. M., & Willacy, K. 2009, ApJ, 693, 1360

Yamamoto, S. 2017, Introduction to Astrochemistry: Chemical Evolution from Interstellar Clouds to Star and Planet Formation (Springer)

Youdin, A. N., & Goodman, J. 2005, ApJ, 620, 459

Zhang, K., Bergin, E. A., Blake, G. A., Cleeves, L. I., & Schwarz, K. R. 2017, NatAs, 1, 0130

Zinnecker, H., & Preibisch, T. 1994, A&A, 292, 152